Nanoscale

REVIEW

View Article Online
View Journal | View Issue

Cite this: *Nanoscale*, 2026, **18**, 8953

Catalytic applications of carbon nanotubes in energy and environmental remediation: multifunctional roles and design strategy

Samson A. Adeoye and Placidus B. Amama *

Received 17th December 2025,
Accepted 4th March 2026

DOI: 10.1039/d5nr05306d

rsc.li/nanoscale

Carbon nanotubes (CNTs) have emerged as highly multifunctional nanomaterials capable of addressing pressing challenges in energy conversion and environmental remediation. Their catalytic role has evolved from passive conductive supports to active, tunable catalytic platforms enabled by good control over nanotube structure, defect chemistry, and electronic properties. Across energy and environmental applications, catalytic performance is governed by unified nanoscale principles, including electronic structure modulation through heteroatom doping, nano-confinement-induced stabilization of active species, and strong interfacial interactions that facilitate efficient charge transfer and dynamic redox processes. Recent advances have demonstrated that CNTs are efficient and durable electrocatalysts and thermally stable supports for hydrocarbon reforming, in which confinement suppresses carbon accumulation. In environmental remediation, CNTs serve as efficient electron acceptors in hybrid photocatalysts, thereby suppressing electron–hole recombination and promoting the degradation of persistent pollutants and inactivation of pathogens. This review critically examines the advances in CNT-based catalysts and the emerging catalytic role of CNTs in these applications. It clarifies the structure–property–function relationships that define CNT catalytic behavior and identifies key challenges and future directions necessary to translate CNT-based catalysts into sustainable energy and environmental remediation technologies.

1. Introduction

The rapidly evolving fields of energy and environmental sustainability are being transformed by innovations in materials science, with carbon nanotubes (CNTs) emerging as a promising class of nanomaterials.[1] This is due to their superior mechanical, electrical, thermal, and optical properties, as well as their high aspect ratio and sp^2 carbon bonding, which have enabled various catalytic applications.[1–4] Our search of the Web of Science database reveals a growing interest in the application of CNTs for tackling energy and environmental issues. Since 1991, the number of published articles on the use of CNT-based hybrid nanomaterials has steadily increased (Fig. 1). This upward trend demonstrates that the scientific community is aware of the potential revolutionary impact of CNTs.

CNTs are widely utilized as supports and active components in catalytic processes, such as in electrocatalysis, Fischer–Tropsch synthesis (FTS), reforming of hydrocarbons, and photocatalysis. Their hollow structure provides a confined space for encapsulating or hosting functional species, enabling the synthesis of high-performance supported catalysts.[5] CNTs provide unique benefits, including high mechanical strength, thermal and chemical stability, low hydrophobicity, and mesoporosity, which facilitate superior mass transport and highly dispersed active sites.[6–8] The catalytic role of CNTs has evolved from passive conductive supports to active, tunable catalytic platforms enabled by good control over nanotube structure, defect chemistry, and electronic properties. In electrocatalysis, applications of CNTs have expanded beyond their traditional role as conductive supports. They function as robust scaffolds, effectively preventing the aggregation of active catalytic materials and facilitating the uniform dispersion of catalysts, including single-atom catalysts (SACs). In addition to favorable metal–support interactions, controlling the inherent structural defects of CNTs enhances catalytic activity and selectivity. The unique role of CNTs in electrocatalysis is attributed to the complex synergistic effects involving defects, heteroatom doping, metal–CNT electronic interactions, and confinement that lead to high efficiency. Furthermore, CNTs serve as nanostructured support materials in thermocatalysis, such as Fischer–Tropsch synthesis (FTS) and reforming of hydrocarbons.[9,10] Their unique properties and confinement effects boost catalytic activity and stability. This is especially evident in dry reforming of methane (DRM), where CNTs help reduce carbon deposition and affect the electronic properties of encapsulated metal nanoparticles.[9,11] This leads to higher

Tim Taylor Department of Chemical Engineering, Kansas State University, Manhattan, KS 66506, USA. E-mail: pamama@ksu.edu

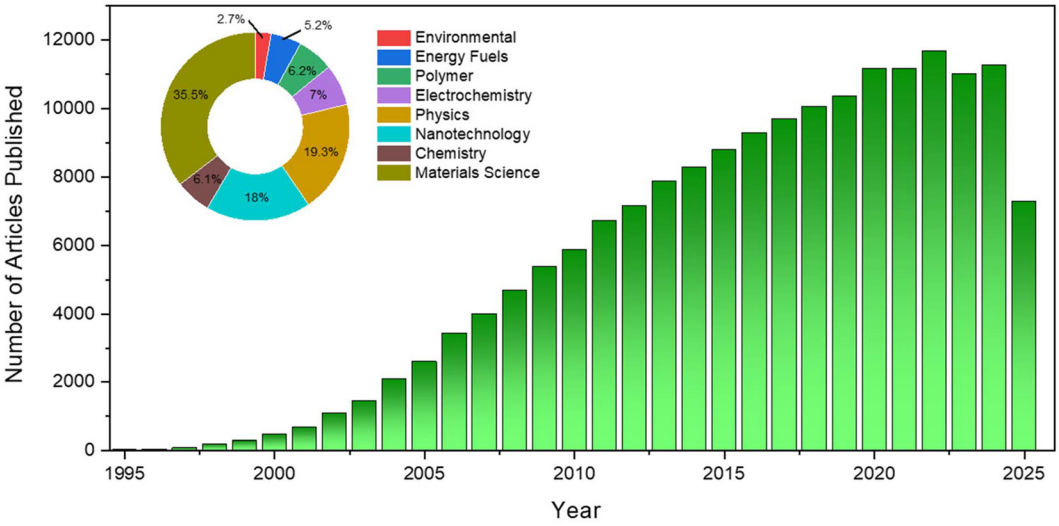

Fig. 1 Trends in research on catalytic applications of CNTs represented as the number of articles published from 1995 to 2025 (data from web of science). The inset shows the research fields that contribute to the catalytic applications of CNTs.

catalytic activity and superior stability than similar catalysts on traditional supports, while promoting the reduction of metal oxides to the active metallic phase. In photocatalysis, CNT-based materials have shown excellent activity in degrading environmental pollutants and inactivating pathogens. In air and water purification, CNTs play unique roles as adsorbents, electron reservoirs, co-catalysts, and reaction modulators. As effective electron mediators and reservoirs, CNTs promote interfacial charge separation, a prerequisite for the formation of reactive oxygen species (ROS)—the active species in photocatalytic pollutant degradation and pathogen inactivation.

Fig. 2 illustrates the evolution of CNTs from the 1990s to 2025, highlighting their catalytic applications in energy and environmental remediation. For the various applications in the roadmap, representative studies are presented below the figure. It emphasizes four major functional catalytic roles of CNTs: (i) support, (ii) promoter, (iii) confinement, and (iv) platform for key application areas such as electrocatalysis, Fischer–Tropsch synthesis, hydrocarbon reforming, wastewater treatment, air purification, and food safety. The early recognition of CNTs as excellent catalyst supports has inspired widespread research since the mid-2000s. Several studies (Fig. 2) have explored how promoter effects enhance activity, selectivity, and stability through methods such as alloying, heteroatom doping, and the development of bimetallic systems. The confinement effect of CNTs represents a significant breakthrough. Examples include encapsulation, tip-growth modes, single-atom catalysts, and CNT-based membranes, which have enabled precise control over reaction pathways, suppressed sintering, and enabled phenomena such as overcoming the Anderson-Schulz-Flory (ASF) limits, achieving room-temperature NO oxidation, and facilitating selective photocatalytic or electrochemical reactions. Recently, CNTs have evolved into a multifunctional platform capable of simultaneous adsorption and complex catalytic reactions.

Therefore, this review aims to critically examine advances in catalytic applications of CNTs in energy and environmental remediation, and clarify the structure–property–function relationships that define CNT catalytic behavior. The review also identifies key challenges and future directions necessary to translate CNT-based catalysts into sustainable energy and environmental remediation technologies (Fig. 3). Finally, we present our perspectives on critical future research directions needed to translate CNT-based catalysts into next-generation sustainable energy-conversion and environmental-remediation technologies.

CNTs are allotropes of carbon with a cylindrical nanostructure made of carbon atoms arranged in a sp^2-hybridized honeycomb lattice.[12–14] CNTs are composed of strong C–C covalent bonds, and pristine CNTs are hydrophobic, tend to form bundles and aggregates due to strong van der Waals forces.[15–18] They primarily exist in two forms: single-walled CNTs (SWCNTs, Fig. 4a) and multi-walled CNTs (MWCNTs). SWCNTs exhibit a hollow structure that provides an extraordinary surface-area-to-length ratio.[8] Based on their high aspect ratio[19–21] and the 1-D structure,[12] SWCNTs exhibit a wide range of properties that are highly dependent on their atomic arrangement, especially their chirality.[22,23] MWCNTs (Fig. 4b), on the other hand, are composed of at least two concentrically interlinked nanotubes,.[24] Moreover, MWCNTs exhibit superior mechanical strength due to their multilayered carbon structure.[25] Table 1 shows the major distinctions between MWCNTs and SWCNTs.

2. Key challenges in CNT application

Despite significant progress in the CNT field, several challenges remain in their catalytic applications for addressing energy and environmental issues. Although it is agreed that

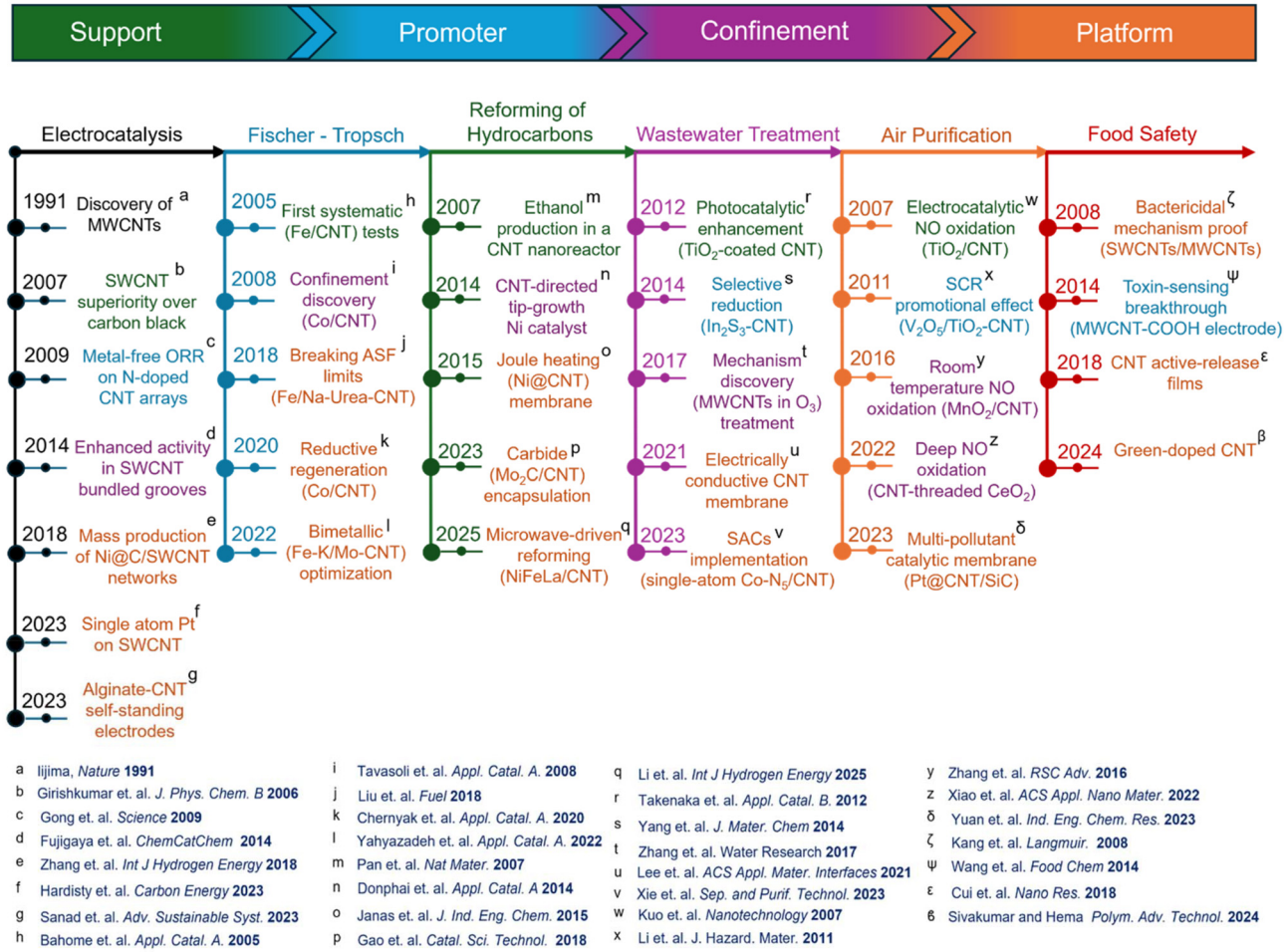

Fig. 2 Roadmap of catalytic applications of CNTs in energy and environmental remediation.

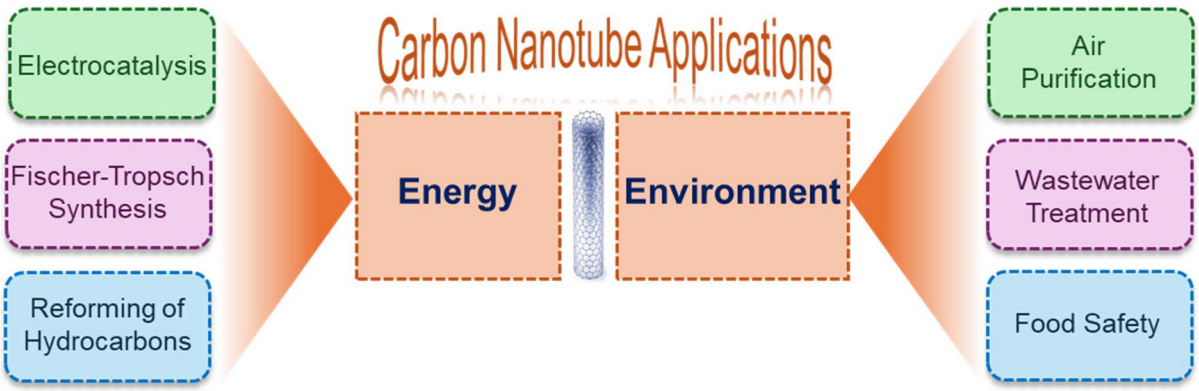

Fig. 3 Summary of the catalytic applications of CNTs.

the catalyst plays a critical role during nucleation and growth, the mechanisms underlying nucleation and chirality selectivity remain poorly understood. Thus, achieving precise control over the structure and electronic properties of the produced nanotubes remains a major hurdle.[15] While post-synthesis sorting has advanced significantly, yield, scalability, and cost remain problematic.[31] Developing catalysts that are active, stable, selective, and cost-effective is crucial for industrial processes.

As-synthesized CNTs, regardless of the method, inevitably contain impurities, such as amorphous carbon and metal catalyst particles, which can severely degrade their properties.[15]

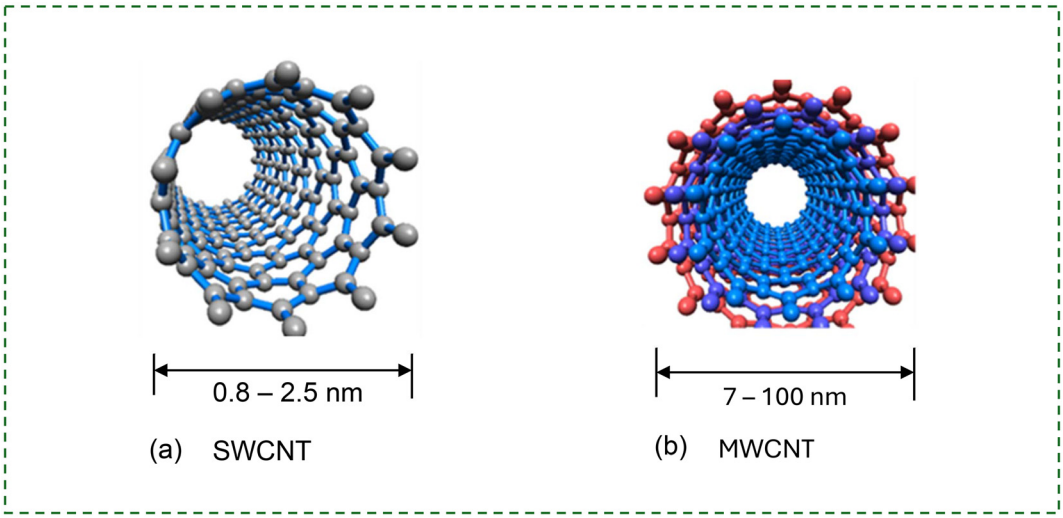

Fig. 4 Structure of (a) a SWCNT and (b) a MWCNT.

Table 1 Differences between MWCNT and SWCNT[26–30]

Properties	MWCNTs	SWCNTs
Diameter (nm)	5–20	0.8–2
Length (nm)	10–1000	0.14–55.5
Permittivity	1×10^4	30–1000
Specific gravity (bulk) (g cm^{-3})	1.8–2.6	1.8–2.3
Specific area (m^2 g^{-1})	200–400	400–900
Young's modulus (TPa)	0.3–1	1
Tensile strength (Pa)	1×10^{10}–15×10^{10}	3×10^{10}–5×10^{11}
Thermal conductivity (W m^{-1} K^{-1})	2000–3000	3000–6000
Electrical conductivity (S cm^{-1})	10^3–10^5	10^2–10^6
Thermal stability temperature in air (°C)	550–650	550–650
Cost	Cheaper	Expensive

Structural defects, such as dangling bonds, are also commonly found.[15] SWCNTs have a strong tendency to form bundles and aggregates due to strong van der Waals forces.[15–17] This agglomeration is detrimental to the properties of their composites and prevents their full utilization.[17] Pristine SWCNTs are highly hydrophobic and generally form insoluble aggregates, making it difficult to isolate individual nanotubes and integrate them effectively into various media.[15] It is also difficult to stabilize their properties during processing, especially in polymer–nanotube composites.[32] Historically, the high production cost of high-quality nanotubes has been a major barrier to commercial adoption, limiting their use to high-end products.[33,34] While significant progress has been made, cost remains a concern. There are also concerns regarding the long-term safety and toxicity of CNTs, particularly concerning human exposure through skin contact and inhalation.[17,35] Research data on toxicity can be ambiguous, with some studies showing cytotoxicity while others do not.[34] The biological effects of CNTs are known to depend on factors such as surface functionalization, solubility, and size.[18] Standardization of characterization methods for comprehensive safety assessment is crucial but still lacking. The long-term performance of SWCNTs, especially when integrated with metals, is a neglected aspect. Issues such as galvanic cell formation, leading to metal oxidation and corrosion, need to be addressed.[17]

To overcome the significant challenges posed by low growth efficiency and high costs that hinder SWCNT commercialization, concerted research has led to the development of various innovative growth processes. The most prominent is the water-assisted CVD method or "super-growth" process, developed at the National Institute of Advanced Industrial Science and Technology (AIST)[36] for synthesizing SWCNTs. This innovative CVD method, which involves the introduction of trace amounts of water, is characterized by a high yield of SWCNTs (SG-CNTs) per unit volume and time at atmospheric pressure, facilitating continuous synthesis in an open system.[36] The super-growth method significantly improves catalyst activity and lifespan, and SG-CNTs are characterized by larger diameters, typically 3 to 5 nm, and considerable lengths, from 100 to 600 μm.[36] In addition to the super-growth method, Almkhelfe *et al.*[37] introduced a novel approach that utilizes a mixture of gaseous products from Fischer–Tropsch synthesis (FTS–GP) as a feedstock to extend the lifetime of catalysts used in the CVD growth of CNTs. The FTS–GP mixture, which includes 40 vol% H_2 and 5 vol% CO, facilitates a reaction where CO and H_2 combine to produce water. The reaction is favored under low CO partial pressure and at temperatures above 400 °C (ref. 38 and 39)—conditions that are satisfied by the composition of FTS–GP and the growth temperatures of CNTs. As with supergrowth,[38] the *in situ* generated water acts as an oxidant. It actively removes excess amorphous carbon impurities from the catalyst surface, preventing early deactivation and thereby extending the active lifetime of catalysts,[37] even though FTS–GP delivers a high flux of carbon to the catalyst surface.[37,38] Similarly, the floating catalyst CVD

(FCCVD) introduced by Endo *et al.*[40] in 1993 and later adapted for SWCNT growth by Cheng *et al.*[41] and Nikolaev *et al.*[42] (HiPco process) has been reported to produce high yields of CNTs.[43] The efficiency of FCCVD is further enhanced by operating at high growth temperatures, typically above 1000 °C, which facilitates the synthesis of SWCNTs with long lengths, often exceeding 100 μm, and high crystallinity.[44] The fluidized-bed CVD introduced by Noda *et al.*[45] leverages the 3-D reaction space of the bed by using spherical ceramic beads as catalyst supports to enhance the efficiency of CNT growth. This method boasts a high productivity of over 0.2 kg-CNT per L-reactor per day and an estimated bead reusability of over 10 000 cycles.[45]

CNTs are among the most widely produced nanomaterials, holding over 26% of the market share in the overall nanomaterials industry.[46] The commercialization of SWCNTs has, however, been slower than that of MWCNTs, primarily due to low growth efficiency, high cost, and inconsistent quality.[34] The global volume of CNTs is expected to reach 7000 tons by 2025.[46] Fig. 5 shows the general trend of increasing global production of CNTs. Historically, MWCNTs have been the dominant form in the market, accounting for 80% of the total CNTs produced, while SWCNTs account for the remaining 20%.[46] Companies such as OCSiAI produce TUBALL™ SWCNTs,[34] which are commercially available with specific properties, including diameters of ≤2 nm, lengths >5 μm, and purity typically ≥94% (up to 100%).[47,48] MWCNTs are also produced by companies such as NanoLab, with reported characteristics including a diameter of 30 ± 15 nm, a length of 5–20 μm, and a purity of >95%.[48] CNano Technology not only holds several patents for CNT production, but is also a global supplier, investing USD 94.7 million in a manufacturing facility in the Kansas City area of the United States.[49] Other companies, such as NoPo Nanotechnologies and NanoIntegris, supply HiPCo SWCNTs,[50] while Meijo Nano Carbon provides SWCNTs.[51] The global CNT market reached USD 1.3 billion in 2024 and is projected to reach USD 2.6 billion by 2029.[35] The increasing availability of high-quality CNTs on the market, along with the emergence of new players, signifies that the time for their widespread industrial applications has arrived.[34]

3. Relevant properties of CNTs to catalysis

3.1 Textural properties

CNTs exhibit exceptional textural properties due to their tightly interwoven, porous tubular structure, which is fundamentally tied to their unique cylindrical structure and high aspect ratio.[12,14] They are characterized by a high surface area, which makes them suitable for applications requiring high adsorption capacity, especially in catalysis.[48,52] MWCNTs are characterized by a mesoporous structure (9.6–14.7 nm),[53] enabling macromolecules to readily penetrate and adsorb onto the catalyst surface, thereby enhancing catalytic activity.[6,7] Furthermore, MWCNTs possess high specific surface areas (>200 m^2 g^{-1}) and pore volumes (>0.5 cm^3 g^{-1}),[54] depending

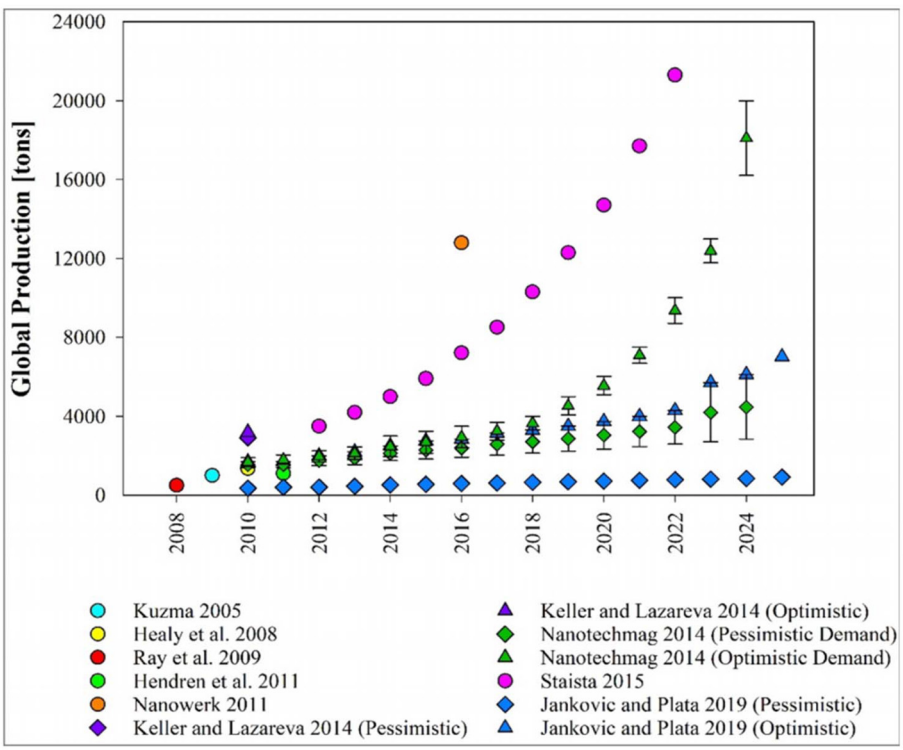

Fig. 5 Global market for CNTs.[46] Figure reprinted from ref. 46 *Int. J. Life Cycle Assess.*, 2021, **26**, 656–672, with permission from Springer Nature, copyright 2026.

on the methods used for synthesis, purification, and functionalization. In the case of SWCNTs, reported specific surface areas vary: 551 m^2 g^{-1} with a total pore volume of 0.993 cm^3 g^{-1}, or 45.67 m^2 g^{-1} with a pore volume of 0.065 cm^3 g^{-1} and an average pore size of 8.24 nm.[2,55] These properties can be modified by techniques such as lithium doping or hybridization with other materials (*e.g.*, MoS_2), which can increase the specific surface area and pore volume.[2,55] The morphology of CNTs can vary significantly depending on processing; for instance, SWCNT films with low dopant concentrations may exhibit rough bundle surfaces, whereas higher dopant concentrations can lead to smoother surfaces as the bundles become covered.[56]

3.2 Mechanical properties

CNTs possess exceptional mechanical strength, including high tensile strength and Young's modulus.[13,57] CNTs have tensile strengths of approximately 100 GPa and a Young's modulus of around 1 TPa, which are attributed to their strong C–C bonds.[14] This makes them superior additives to matrix composites.[13] For example, Ramirez B *et al.*[58] show that SWCNTs in an optimized buckypaper framework exhibited an excellent tensile strength of 236.9 ± 12.1 MPa. The SWCNTs used in such frameworks had an aspect ratio of 1500–3000, whereas the ultimate tensile strength of welded SWCNT free-standing films can reach approximately 22 MPa.[58] When coated onto aramid fibers, SWCNTs can help composites retain ≥84.9% of their original strength.[59] Additionally, SWCNTs exhibit excellent mechanical flexibility and ultrastretchability, making them highly suitable for bendability applications and flexible electronics, with some engineered composites demonstrating fracture strains exceeding 1700% and maintaining structural integrity under significant deformation.[60–62]

3.3 Electronic properties

SWCNTs are characterized by high carrier mobility, injection velocity, and current-carrying capability.[63] Their electronic nature is determined by the chiral indices (n,m). They are metallic (m-SWCNTs) when $n - m = 3j$ (j is an integer), and semiconducting (s-SWCNTs) with different band gaps when $n - m = 3j + 1$ or $3j + 2$.[17,20,31,32,64] m-SWCNTs are highly conductive and can carry current densities more than 1000 times higher than copper.[16,19,20,65,66] SWCNTs exhibit exceptionally high electronic mobilities, theoretically exceeding 100 000 cm^2 V^{-1} s^{-1},[33,34] and SWCNT films have high carrier concentrations ranging from 10^{21} to 10^{23} cm^{-3}.[20,66] Their electrical properties are very sensitive to chemical modification or atomic doping.[66,67] For instance, a low defect density results in high electrical conductivity.[21] SWCNT thin films can achieve very high conductivity, with sheet resistances as low as 51 Ohms per square meter at 90% transmission (550 nm wavelength) after HNO_3 doping.[68]

3.4 Thermal properties

CNTs exhibit high thermal stability and excellent thermal conductivity due to their highly ordered sp^2-carbon.[13,14,69] In practical applications, the inherent thermal stability of CNTs at temperatures as high as 250 °C benefits processes like flue gas purification.[6] Suspended m-SWCNTs with diameters around 1.7 nm can reach intrinsic thermal conductivity around 3500 W m^{-1} K^{-1} at room temperature.[16,19,20,31,33,34,65,66] Thermal conductivity reduces with increased defect density or surface roughness.[21] SWCNT rings have been shown to offer better thermal stability compared to linear SWCNTs.[67] Also, their thermal performance is significantly influenced by surface modifications and the operating atmosphere. For instance, doping the CNT matrix with heteroatoms, such as nitrogen, generally reduces the thermal stability of the material.[53,70]

3.5 Optical properties

CNTs, particularly SWCNTs, possess remarkable optical properties, including characteristic absorption and fluorescence that are intrinsically linked to their diameter and chirality.[13,71] SWCNTs exhibit photoluminescence (PL) in the near-infrared (NIR) fluorescence and shortwave infrared (SWIR) regions.[72,73] This emission originates from quantum-confined surface excitons (electron–hole pairs) and can be significantly modulated by changes in the local environment, such as surface characteristics, dielectric constant, charge, and solvent exposure,[72,74,75] which influence PL quantum yield by creating exciton trap states or affecting spin states.[13,76] Excitons in SWCNTs demonstrate large binding energies and high mobility.[72,76] The PL spectra of SWCNTs@ZSM-5, for instance, showed a peak attributed to the (4,2) nanotube, consistent with theoretical optical transition energies.[77]

3.6 Chemical properties

CNTs have high chemical stability.[16,35] Their reactivity is influenced by surface curvature, particularly at the nanotube caps, where dangling bonds increase reactivity.[15,32] m-SWCNTs are more reactive than s-SWCNTs, mainly due to their electronic structure. Also, Qin *et al.*[78] have shown that m-SWCNTs are readily oxidized due to their lower ionization energy. A key chemical feature of CNTs is their amenability to surface functionalization, which can be either covalent or non-covalent.[13,72,79] This functionalization is crucial for controlling their solubility and improving their dispersibility in various solvents.[15,18,32] Covalent functionalization introduces new Sigma bonds to the CNT, leading to changes in hybridization (sp^2 to sp^3) and novel photophysical properties, thus creating "quantum defects" or "color center nanotubes".[13,79,80] On the other hand, non-covalent functionalization involves interactions, such as van der Waals forces, π–π stacking, hydrophobic interactions, hydrogen bonding, and electrostatic interactions.[13,81]

4. CNT-based catalysts for energy applications

CNTs are at the forefront of advanced materials for next-generation energy technologies. The milestones reached in scalable

synthesis of CNTs are driving innovation across the energy sector, from improving energy generation through electrocatalysis to enhancing the production of clean fuels *via* Fischer–Tropsch synthesis and reforming of hydrocarbons.

4.1 Electrocatalysis

The electrocatalytic applications of CNTs have expanded significantly beyond their conventional role as conductive supports to rationally designed active catalysts, driven by improved control over nanotube structure, defect chemistry, and electronic properties.[82,83] The electrocatalytic performance of CNTs arises from the synergy of electronic modulation, dimensional confinement, and structural stability. The high electrical conductivity and large surface area of the CNT lattice serve as a fundamental scaffold for fast charge transfer and optimized catalyst dispersion, which directly enhances reaction kinetics and the electrochemically accessible surface area.[82,84,85] Heteroatom doping (*e.g.*, N, P) and surface defects systematically tune the electronic structure and charge distribution of the carbon matrix, thereby optimizing the adsorption energy of intermediates and creating active sites for reactions, such as the oxygen reduction reaction (ORR) and water splitting.[82,86,87] Dimensional confinement within the internal pores of CNTs or the grooves of bundled tubes steers reaction pathways through electronic state tailoring, enabling selective catalysis, such as favoring the four-electron ORR route or facilitating selective hydrogen oxidation while suppressing competitive reactions.[88,89] Furthermore, interfacial electronic interactions in CNT heterojunctions shift the Fermi level to create efficient electron tunneling pathways, while the degree of graphitic crystallinity and tube diameter governs electrochemical durability by dictating resistance to carbon corrosion (electrochemical oxidation of CNTs) under demanding potentials.[90–92] Recent studies highlight how CNTs function through complex synergistic effects involving defects, heteroatom doping, metal–CNT electronic interactions, and confinement, which lead to high efficiency in energy conversion.[82,84,88] Heteroatom doping remains a crucial strategy for maximizing the intrinsic electrocatalytic activity of CNTs, particularly for the ORR and oxygen evolution reaction (OER).[82] Li *et al.*[82] developed a SWCNT conductive network encapsulated in porous N, P co-doped carbon (SWCNT@NPC) (see Fig. 6a–g), which exhibited excellent bifunctional activity. They found that mutual promotion between N and P doping induced ultrahigh ORR activity, resulting in a half-wave potential of 0.85 V (Fig. 6h), comparable to that of commercial Pt/C and exhibiting enhanced durability (Fig. 6i–k). Mechanistically, this enhanced performance was attributed to N doping facilitating P doping, optimizing the O_2 adsorption energy, and promoting the formation of pyridinic N, which serves as a key active site for the ORR. Conversely, for the OER, N-doping sites were identified as the primary active components.

Beyond traditional chemical doping, controlling the inherent structural defects of CNTs also facilitates catalytic activity. Mohan *et al.*[87] demonstrated that simply exposing CNTs to oxygen plasma intentionally created surface defects and incorporated oxygenated functionalities (C–O, C═O, COO) as shown by the SEM images (Fig. 7a–d) and high-resolution deconvoluted spectra (Fig. 7e–l), which served as active sites for ORR in alkaline electrolytes. Their comparative study indicated that oxygen plasma-treated SWCNTs (O-SWCNTs) (Fig. 7m and n) exhibited superior ORR activity (onset potential of 0.78 V *vs.* RHE) compared to O-MWCNTs (Fig. 7n and p), suggesting that the intrinsic single-layer architecture of SWCNTs provided greater accessibility for functionalization. Also, the physical geometry of CNT structures provides additional avenues for tuning intrinsic activity Fujigaya *et al.*[89] compared N-doped graphitic structures coated onto bundled SWCNTs (SWCNT/N-GS) with MWCNTs (MWCNT/N-GS) for ORR in acidic media. They observed a dramatic enhancement in ORR activity for the SWCNT/N-GS (onset potential of 0.75 V *vs.* RHE) compared to the MWCNT/N-GS (0.61 V), attributing this enhancement to the formation of unique confined nanospaces, specifically grooves within the bundled SWCNT structure, which facilitate superior O_2 adsorption.

CNTs can serve as co-catalysts and supports for water splitting, offering the benefits of zero CO_2 release, recyclability, and high gravimetric energy densities.[93] In the electrochemical conversion of CO_2, catalysts supported on SWCNTs can enhance the selectivity of Cu-based electrocatalysts to valuable chemicals.

Li *et al.*[94] developed a facile and scalable synthesis method for ultrasmall (1 nm) gold nanocrystals (AuNCs) supported on s-SWCNTs. Under photon irradiation, electron–hole pairs are generated in the s-SWCNTs; electrons are injected into the AuNCs to reduce Au^{3+}, while holes remain in the s-SWCNTs, resulting in p-doping. The developed nanocomposites show a high faradaic CO selectivity of up to 86% at 25 mA cm^{-2}. Moreover, they achieved a mass activity of 5.61 A mg^{-1} (Au) at 100 mA cm^{-2}. CNTs consistently improved the overall conductivity of the composite materials, which is crucial for accelerating electrochemical reactions.[95,96] Wen *et al.*[95] observed that the CNT support in WO_{3-x}/CNT significantly enhances conductivity, facilitating electron transfer from tungsten atoms to carbon atoms *via* an oxygen bridge structure (W–O–C). This interfacial electron transfer channel is key to optimizing the electronic structure of the active metal sites. Xu *et al.*[97] highlighted that CNTs in covalent organic framework (COF@CNT) composites overcame the inherent low conductivity of COF materials, thereby maximizing electrocatalytic activity. Jia *et al.*[98] further reported that hybridization of the lone pair electrons from oxygen with Ni 3d orbitals in NiTPP@CNT-ox gives rise to new electronic states near the Fermi level, thereby enhancing surface electron-transfer efficiency.

The electronic properties of SWCNTs can be manipulated to selectively steer electrocatalytic reaction pathways, functioning as more than just a charge conduit. Hu *et al.*[88] demonstrated that the electrocatalytic ORR pathway of SWCNTs could be controllably tailored by modifying their electronic states *via* filling the inner space with electron donor substances. They observed that incorporating K or Fe resulted in n-type doping, preferentially favoring the four-electron ($4e^-$) pathway suitable

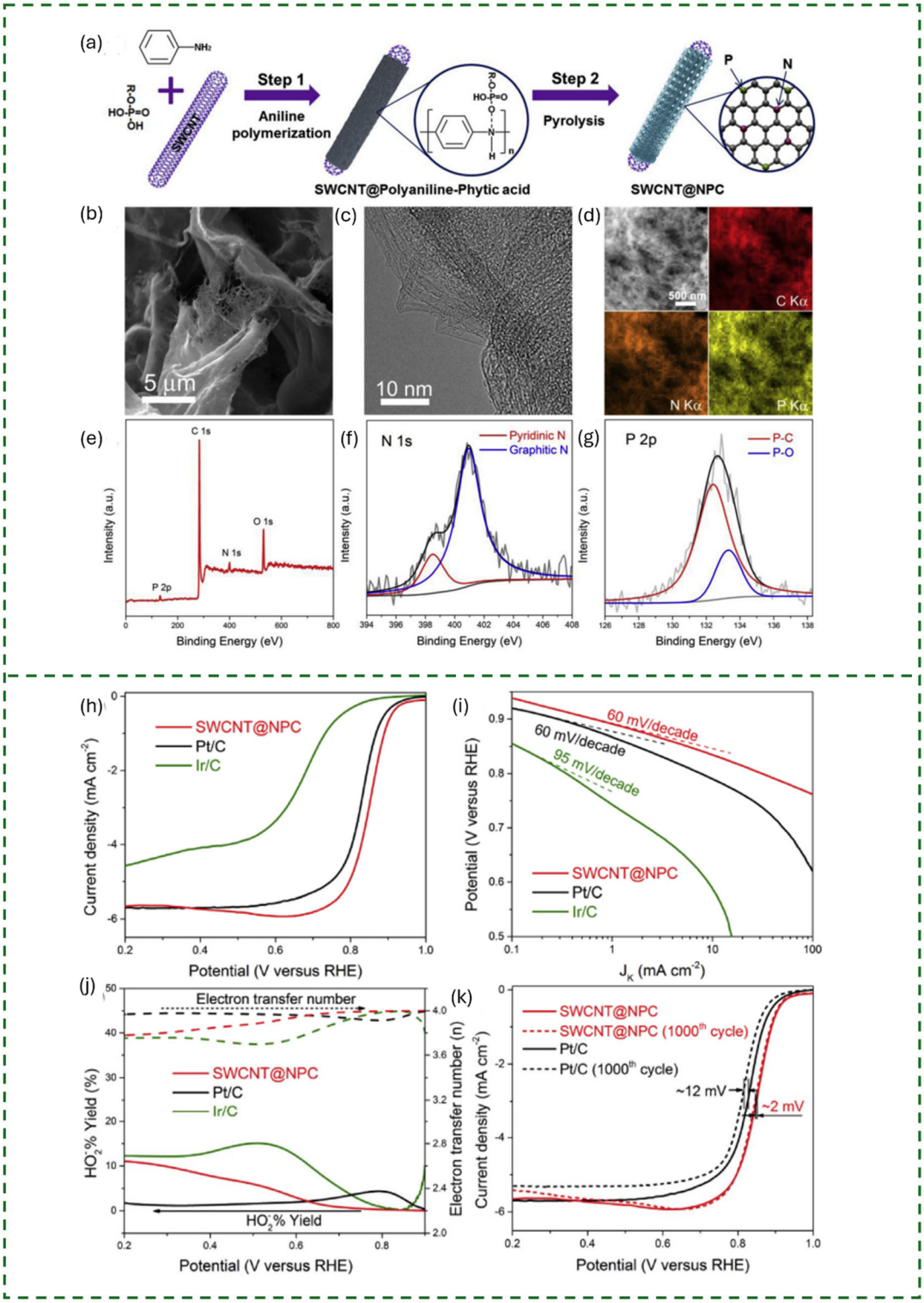

Fig. 6 (a) Schematic of the preparation procedure of SWCNT@NPC. (b) SEM and (c) TEM images of SWCNT@NPC. (d) A STEM image with corresponding element mapping images of SWCNT@NPC. XPS spectra of SWCNT@NPC: (e) survey, (f) N 1s, and (g) P 2p. (h) ORR polarization curves and (i) Tafel plots of SWCNT@NPC, Pt/C, and Ir/C in an O_2-saturated 0.1 M KOH. (j) HO_2^- yield and electron transfer number of the SWCNT@NPC, Pt/C, and Ir/C catalysts. (k) ORR polarization curves of the SWCNT@NPC and Pt/C catalysts before and after 1000 CV cycles.[82] Figures a–k reprinted from ref. 82 *Carbon*, 2018, **139**, 156–163, with permission from Elsevier, copyright 2026.

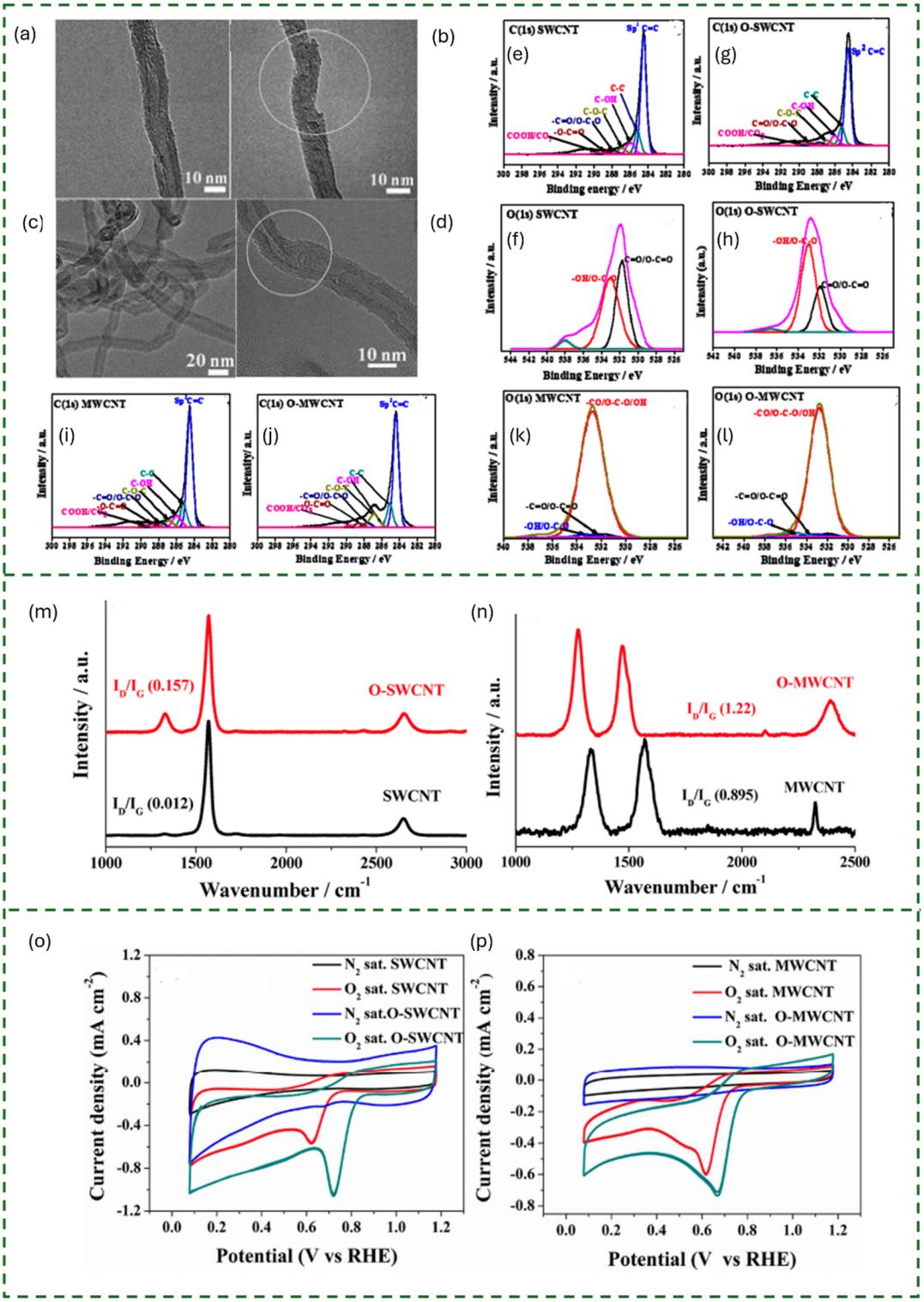

Fig. 7 HR-TEM images of (a) untreated SWCNT, (b) 20 min O_2 plasma-treated SWCNT, (c) untreated MWCNT, and (d) 20 min O_2 plasma-treated MWCNT (the white circle indicates the defect sites). High-resolution deconvoluted (C 1s and O 1s) spectra of (e, f) pristine SWCNT, (g, h) plasma-treated SWCNT, (i, j) pristine MWCNT, and (k, l) plasma-treated MWCNT. (m) Raman spectra of oxygen-plasma-treated and pristine SWCNT and (n) MWCNT. (o) CV of untreated and plasma-treated SWCNT and (p) MWCNT in N_2- and O_2-saturated 0.10 M KOH. Catalyst loading: 50 μg cm^{-2}, at a scan rate of 50 mV s^{-1}.[87] Figures a–p reprinted from ref. 87 *ACS Sustainable Chem. Eng.*, 2019, **7**, 11396–11406, with permission from the American Chemical Society, copyright 2026.

for fuel cells, while electron acceptors such as I_2 induced p-type doping, steering the reaction towards the two-electron ($2e^-$) pathway for H_2O_2 production.[88] The geometric and electronic constraints imposed by the CNT interior lead to unique activity patterns, particularly evident in single-atom catalysts (SACs). When compared to other supports such as graphene, carbon black, and oxide supports, CNTs offer more advantages as SAC supports. Their high longitudinal conductivity enables rapid charge transfer[84] along the tube axis, eliminating the need for extra conductive additives typically required for poorly conducting oxides.[99] Moreover, SWCNTs provide a high electrochemically accessible surface area, allowing a greater fraction of single atoms that are active to be exposed compared with porous carbons,[85] where deep pores and internal voids often create large amounts of "dead" mass that cannot participate in catalysis. Furthermore, CNTs exhibit superior durability as SAC hosts – the high graphitic crystallinity and multilayer stacking of MWCNTs stabilize metal–carbon bonds and resist electrochemical carbon corrosion at high potentials,[100] outperforming carbon black and single-layer nanostructures that are prone to oxidative degradation and atom detachment. Hardisty *et al.*[99] synthesized Pt SACs confined inside SWCNTs. They found that these Pt SAC samples showed high hydrogen oxidation reaction (HOR) activity, often surpassing that of commercial Pt/C across the high overpotential range. Specifically, the Pt SAC exhibited almost no ORR activity in the operating range of proton exchange membrane fuel cells (PEMFCs). This selective activity towards HOR was identified as the key fingerprint of catalyst confinement, offering a strategy to develop anode electrocatalysts insensitive to oxygen poisoning.[99] In metal-containing hybrid systems, the CNT structure promotes electronic interaction with the active component. Zhu *et al.*[90] studied iron phthalocyanine (FePc) coated on SWCNTs (FePc/SWCNT) as a heterojunction nanowire. Through density functional theory (DFT) calculations, they determined that the enhanced ORR activity stemmed from the metal–CNT electronic interaction; specifically, the metallic SWCNT up-shifted the Fermi level of the p-type semiconducting FePc, creating an efficient channel for transferring electrons to the FePc surface to interact with O_2, resulting in stronger O_2 binding and enhanced kinetics.

The large specific surface area of CNTs provides abundant active sites for electrochemical reactions.[96,101] Marbaniang *et al.*[101] showed that nitrogen doping at defect sites of MWCNTs provides effective exposure of active sites such as pyridinic-N and oxidic-N for oxygen electroreduction. Wen *et al.*[95] further noted that ultra-small WO_3 nanoparticles (~1 nm) uniformly dispersed on CNTs significantly enlarge the active surface area of WO_{3-x}/CNT. Han *et al.*[102] quantified this observation, reporting that PtFeCoNiMoY/CNT catalysts exhibited a larger electrochemically active surface area (ECSA) than commercial RuO_2, indicating more active sites for redox reactions. Beyond providing a high surface area, CNTs can be engineered to have specific anchoring sites for catalysts. Li *et al.*[96] demonstrated that CNT arrays with abundant oxygen-containing groups serve as an efficient matrix for anchoring metal atoms in CNT-O@M SACs. This is further supported by DFT calculations, which show that O-doped carbon substrates exhibit a higher adsorption capacity for metal atoms than undoped ones. The formation of a coaxial-cable structure in COF@CNT[97] and the uniform distribution of ultra-small nanoparticles in WO_{3-x}/CNT[95] illustrate how CNT morphology supports the effective dispersion of active sites.

CNTs function as robust scaffolds, effectively preventing the aggregation of active catalytic materials. This stability is crucial for maintaining catalytic efficiency over time. Li *et al.*[96] showcased that integrated CNT arrays facilitate the uniform dispersion of SACs and enhance metal–support interactions, minimizing agglomeration. Similarly, Yu *et al.*[103] demonstrated that functional groups on cobalt phthalocyanine (CoPc) molecules supported on CNTs prevent their stacking, ensuring a reliable dispersion of the active sites. Majeed *et al.*[86] developed a flexible, self-standing SWCNT film decorated with Ni-doped carbon-encapsulated Ni nanoparticles (NCNi/SWCNT). This bifunctional catalyst achieved overall water splitting with low overpotentials (HER: 190 mV, OER: 270 mV at 10 mA cm^{-2}). The high performance and robust stability were attributed to a synergistic effect, in which the Ni core tunes the electronic structure of the N-doped carbon shell, the monolayer carbon protects against oxidation or aggregation, and the SWCNT network provides high conductivity. Similarly, Zhang *et al.*[84] mass-produced Ni encapsulated in carbon particles anchored on SWCNT networks, reporting highly efficient overall water splitting (OER: 260 mV, HER: 198 mV). Also, Ding *et al.*[104] reported SWCNT-wrapped $CoFe_2O_4$ nanorods for water splitting. The synergy between $CoFe_2O_4$ and SWCNTs created enriched oxygen vacancies in the metal oxide and optimized the electronic structure, boosting both OER (310 mV) and HER (263 mV) activities, while the SWCNT wrap provided crucial stability against aggregation.

SWCNTs offer advantages over common metal supports due to their higher strength, larger surface area, and excellent chemical stability in acidic solutions, as observed by Yang *et al.*[44] The author developed an integrated membrane electrode composed of N-doped carbon-coated high-entropy nanowires (HEA NWs) anchored on a SWCNT network for efficient and stable hydrogen evolution reaction (HER) in an acid solution. The HEA NW@NC/SWCNT film demonstrated a low overpotential of 42 mV at 100 mA cm^{-2} for HER. It exhibited excellent durability up to 1000 h at 500 mA cm^{-2} in an acid solution. Bian *et al.*[93] synthesized nickel hydroxylphosphate (NiPO) SWCNTs and successfully incorporated FeOH onto their surface to enhance oxygen evolution reaction (OER) performance. The optimized NiPO/$Fe(OH)_x$-30 SWCNTs achieved a current density of 10 mA cm^{-2} at an overpotential of 248 mV and 100 mA cm^{-2} at 323 mV, along with a Tafel slope of 45.4 mV dec^{-1}. The high surface area and porous structure of these ultrathin nanotubes are critical for facilitating efficient electron and ion transport, which contributes to high electrochemical activity.

Table 2 summarizes recent advances in the application of CNT-based catalysts for electrocatalysis. The mechanistic

Table 2 Application of CNT-based materials in electrocatalysis

Nanomaterial	Application	Activity	Selectivity/efficiency	Stability	Ref.
N-doped MWCNTs (Mel-NCNT, Hex-NCNT)	ORR (fuel cells)	Mel-NCNT onset 1.1 V, JL = 5.7 mA cm^{-2}; Hex-NCNT onset ~0.92 V	9× higher activity than Pt/C	Mel-NCNT stable 15k cycles (12 mV shift), excellent methanol tolerance	101
WO_{3-x}/CNT (WO_{3-x}/CNT-2 h)	OER (photo-electrocatalysis)	η = 326 mV (dark), 276 mV (light) @ 10 mA cm^{-2}; Tafel slope 53.2 mV dec^{-1}	Maintained current 22 h; only 8 mV shift after 2000 CV cycles	—	95
CNT-O@Co, CNT-O@Pt (SACs)	ORR & HER	Co-SAC: half-wave 0.77 V, JD = −40.1 mA cm^{-2}; Pt-SAC: HER η = 26 mV @ −50 mA cm^{-2}	Pt-SAC 75.7% site utilization *vs.* 11% (Pt/C)	Co-SAC durable after bending/ultrasound; Pt-SAC stable 10k cycles	96
CNT/NCNT@MOFs (MIL-101, CAU-17)	eNRR (NH_3 synthesis)	NCNT@MIL-101 = 607 mg h^{-1} $mgNCNT^{-1}$; CNT@CAU-17 = 11.9 mg h^{-1} mg_{cat}^{-1}	CNT@MIL-101 FE = 37.3%; NCNT@CAU-17 FE = 19.9%; CNT@CAU-17 FE = 31.3%	CNT/NCNT@CAU-17 stable 12 h	105
NiTPP@CNT-ox (Ni-SAC)	2e$^-$ ORR → H_2O_2	Current density up to 1.6 A cm^{-2}; onset 0.58 V	H_2O_2 selectivity 97%; FE > 92% (0.2–1 A cm^{-2})	Maintains >93% FE for 80 h; 10 wt% H_2O_2 achieved	98
PtFeCoNiMoY HEA/CNT	ORR & OER (ZABs)	OER η = 238 mV; ORR half-wave 0.75 V; ΔE = 0.713 V	Specific capacity 797 mAh g^{-1}; power density 128.4 mA cm^{-2}	Stable >80 h @ 5 mA cm^{-2}	102
B_2O_3/F-CNT-h	2e$^-$ ORR → H_2O_2	$n \approx 2.2$; current stable 20 000 s	H_2O_2 selectivity 92%; FE = 87.7%	92% current retained after 20 000 s	106
CoPc-NO_2/CNT, CoPc-NH_2/CNT	CO_2RR → Methanol	~30% methanol selectivity @ −0.88 V	Stable 31% selectivity for 10 h with electrolyte replacement	NH_2 variant resists de-activation better; activity is recoverable *via* reactivation	103

insights provided by these studies reveal how CNT-based catalysts control electron and ion transfer, adsorption of intermediates, and reaction pathways. Marbaniang *et al.*,[101] observed that nitrogen doping at defect sites of MWCNTs is crucial for ORR, with pyridinic-N and oxidic-N serving as active sites for a four-electron transfer mechanism that converts oxygen to water. The study explains that carbon atoms bonded to nitrogen develop a positive charge density, whereas carbon opposite to pyridine-N has a high spin density, both of which act as active sites for O_2 adsorption and subsequent reduction steps. Jia *et al.*[98] discovered that in NiTPP@CNT-ox, hydroxyl groups on the CNT support directly interact with Ni sites, subtly regulating their electronic structure, and creating a Ni–N_4O configuration that acts as an excellent 2e$^-$ ORR site for H_2O_2 production. This interaction leads to the hybridization of lone pair electrons from oxygen with Ni 3d orbitals, forming new electronic states that enhance the adsorption of the crucial *OOH intermediate.

In WO_{3-x}/CNT (see the synthesis in Fig. 8a), Wen *et al.*[95] identified the formation of a W–O–C oxygen bridge structure due to strong interaction between WO_{3-x} and CNT (Fig. 8b–n). This structure regulates the electronic structure of W sites, promoting intrinsic activity and optimizing the adsorption of active *OH species, thereby enhancing OER performance (Fig. 8o–q). Photogenerated holes also contribute by creating additional active sites. The study by Han *et al.*[102] on PtFeCoNiMoY/CNT HEA catalysts revealed that the addition of Mo and Y elements synergistically modulates the electronic structure of alloys. DFT calculations indicated that Mo increases the continuity of upper-spin state electrons near the Fermi level, while Y shifts the d-band center downward, both of which regulate surface adsorption energy and significantly lower the OER energy barrier for the OH to O step.

The choice between SWCNTs and MWCNTs in electrocatalytic applications depends on the specific reaction and environment (Table 3), owing to the complex structure–property relationships. SWCNTs are generally preferred for reactions requiring high mass-specific activity and precise electronic tuning due to their unique quantum effects and high accessible surface area. However, MWCNTs are the preferred choice when electrochemical stability and resistance to carbon corrosion are significant under high-potential or high-temperature conditions.

Mehrpooya *et al.*[109] found that $PtRu_4Fe_5$/SWCNT exhibited the highest mass activity (827 A per g-Pt) and maximum current density (13.2 mA cm^{-2}) for MOR compared to other supports, including MWCNTs and graphene, demonstrating improved mass transfer and proper interaction with the SWCNT support. Similarly, Wu and Xu[85] showed that Pt on SWCNT/Nafion greatly outperformed MWCNT/Nafion for methanol oxidation, possessing lower CO poisoning, higher graphitization, and a much higher electrochemically accessible surface area 9105.1 m^2 g^{-1} for SWCNT/Nafion *versus* 52.5 m^2 g^{-1} for MWCNT/Nafion, facilitating easier charge and mass transfer. CNT structure heavily influences stability under extreme electrochemical potential cycling. Weerathunga and Fujigaya[92] conducted accelerated durability tests (ADT) on Pt catalysts and concluded that the stability of the CNT support dominated the overall durability. They found that MWCNTs with larger diameters and fewer sidewall defects exhibited superior durability compared to smaller MWCNTs and all tested SWCNTs. They established that the electrochemical durability was strongly correlated with the thermal oxidation onset temperature (from thermogravimetric analysis), suggesting that thermal stability serves as a useful predictive metric for electrochemical corrosion resistance. This insight is

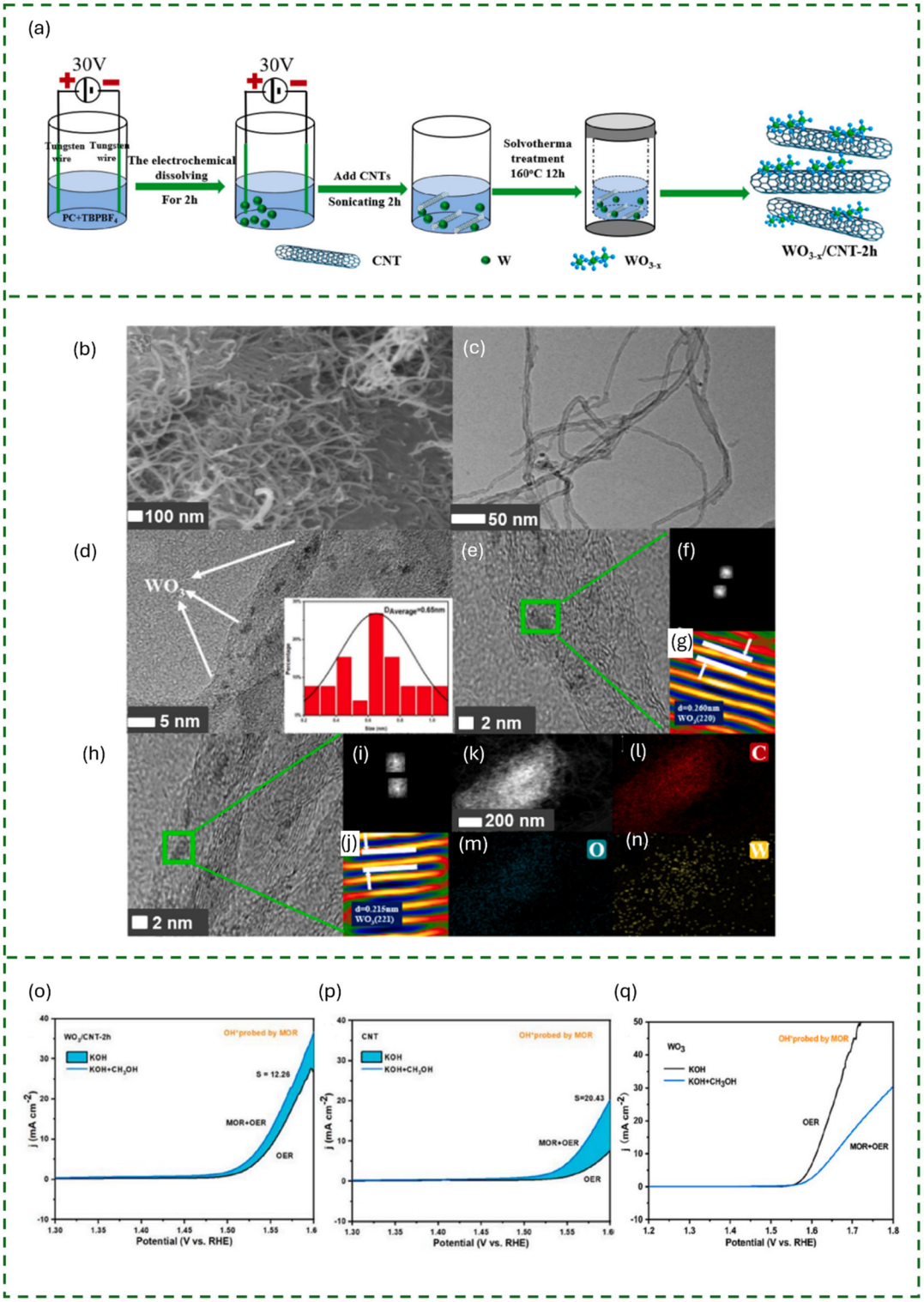

Fig. 8 (a) A schematic illustration of the synthesis process of WO_{3-x}/CNT. (b) SEM images of WO_{3-x}/CNT-2 h, (c–j) TEM images of WO_{3-x}/CNT-2 h, (k) HAADF-STEM images of WO_{3-x}/CNT-2 h, and elemental mappings of (l) carbon, (m) oxygen, and (n) tungsten. (o) LSV curves for MOR and OER on WO_{3-x}/CNT-2 h, (p) CNT, and (q) WO_3 in 1 M KOH and 1 M KOH + CH_3OH at a scan rate of 50 mV s^{-1}.[95] Figures a–q reprinted from ref. 95 *Int. J. Hydrogen Energy*, 2025, **127**, 903–911, with permission from Elsevier, copyright 2026.

Table 3 Structure–function relationships between CNT type and electrocatalytic performance

Reaction/condition	CNT type	Findings	Ref.
Oxygen reduction reaction (ORR)	SWCNTs	Formation of unique bundled "grooves" facilitates superior O_2 adsorption compared to stiff MWCNTs; higher accessibility for oxygen plasma doping	89
Alcohol oxidation reaction (MOR/EOR)	SWCNTs	Twice the electrochemically accessible surface area of MWCNTs; higher utilization and activation of Pt catalysts; lower charge-transfer resistance	85
Corrosion resistance	MWCNTs	Multilayer stacking and larger diameters provide superior resistance to carbon corrosion at high potentials (1.0–1.5 V) and elevated temperatures (~250 °C)	100
Selective hydrogen oxidation (HOR)	SWCNTs	Atomic confinement of Pt single atoms inside SWCNT pores enables HOR activity while remaining insensitive to oxygen poisoning	99
Hydrogen evolution reaction (HER)	SWCNTs	Presence of more nanographitic edges and higher intrinsic activity compared to generally inactive MWCNTs; easier to tune *via* electrolyte engineering (*e.g.*, Li^+ ions)	107
Reaction pathway tailoring ($2e^-$ *vs.* $4e^-$ ORR)	SWCNTs	Controllable tailoring of ORR pathways (H_2O_2 *vs.* H_2O production) *via* n-type or p-type electronic state modification of the inner space	88
Bifunctional water splitting (HER/OER)	SWCNTs	Flexible, self-standing networks provide a high-conductivity scaffold for core–shell metal@carbon nanoparticles, minimizing interfacial resistance	82
Electron tunneling	TWCNTs	Pd supported on triple-walled CNTs (TWCNTs) shows "volcano-type" peak activity due to electron tunneling between outer and inner walls	91
Electrochemical sensing	SWCNTs/ MWCNTs	A 1 : 1 ratio of SWCNT to MWCNT creates a compact synergistic structure with higher electroactive concentration on the electrode surface	108

also supported by a study carried out by Papandrew *et al.*[100] involving solid acid fuel cells, where SWCNTs (nanohorns) quickly degraded due to electrochemical carbon corrosion, whereas MWCNTs proved stable, attributing their corrosion resistance to larger tube size and low defect density. Furthermore, Table 4 compares the electrocatalytic performance of SWCNTs and MWCNTs, highlighting a fundamental trade-off between catalytic activity, structural stability, cost, and scalability.

4.2 Fischer–Tropsch synthesis

Fischer–Tropsch synthesis (FTS) is a process that catalytically converts syngas ($CO + H_2$) into liquid hydrocarbons, contributing to the reduction of reliance on fossil fuels.[110,111] CNTs are widely used as catalyst supports owing to their mesoporosity, chemical inertness, high thermal stability, electrical conductivity, and mechanical strength.[110,112] CNTs possess a relatively large, freely accessible surface area and an open, macro- and mesoporous structure.[113–115] This high surface area enhances CO adsorption, a critical step in FTS. For instance, Yahyazadeh *et al.*[116] demonstrated that the larger surface areas of synthesized CNTs (267 $m^2\ g^{-1}$) and commercial CNTs (380 $m^2\ g^{-1}$) contributed to higher CO conversion compared to Al_2O_3 (221 $m^2\ g^{-1}$). Surface functionalization of CNTs, particularly through nitrogen doping, introduces electron-donating sites that transfer charge to transition metals, thereby weakening the C≡O bond and accelerating CO dissociation to boost overall reaction activity.[53,70] These functional groups and structural defects (higher I_D/I_G ratios obtained from their Raman spectra) function as anchoring sites that enhance metal dispersion and prevent deactivation by suppressing nanoparticle sintering.[54] The unique electronic structure of CNTs due to their curvature induces a π-electron density shift from the inner to the outer walls, making the interior electron-deficient and resulting in weaker metal–oxygen bonds (*e.g.*, iron oxides) that facilitate facile autoreduction and the formation of an active iron carbide phase, leading to improved FTS performance.[53,117]

Unlike conventional oxide supports, which are poor heat conductors, CNTs exhibit excellent thermal conductivity.[113,118] This property is crucial in FTS, as the reaction is highly exothermic. The high thermal conductivity of CNTs minimizes temperature gradients across the reactor bed, preventing local overheating and hot spots that can lead to catalyst deactivation and undesirable product selectivity.[119] Almkhelfe *et al.*[119] hypothesized that CNT networks minimize temperature gradients, allowing for maximum catalytic activity at lower temperatures (<200 °C). CNTs are chemically inert and do not typically form inactive complex oxides with the active metal phase, a common drawback of oxide supports.[113,114,120] This inertness, coupled with their mechanical and thermal stability, contributes to enhanced catalyst reducibility and overall stability.[113,118]

The unique tubular structure of CNTs enables confinement effects, where active metal nanoparticles can be housed within the CNT channels.[121] This confinement can restrict particle growth and agglomeration, stabilizing the nanoparticles and influencing FTS activity and selectivity.[121,122] Additionally, the nano-confinement effect extends the residence time of reaction intermediates, thereby directly enhancing the probability of chain-growth toward long-chain C_5^+ hydrocarbons and waxes.[123] Akbarzadeh *et al.*[124] found that the confinement of active sites within CNT channels significantly enhances C_5^+ selectivity and reduces methane formation rates, largely due to the lower sintering potential of confined particles compared to those on the external surface. Acid treatment purifies CNTs, introduces oxygen-containing functional groups that serve as anchoring sites, and opens their closed ends, whereas thermal treatment improves metal dispersion and alters morphology. Karimi *et al.*[122] found that small cobalt crystallites (3–8 nm) were mostly confined inside functionalized CNTs, and this confinement was crucial for FTS activity. Similarly, Pendyala *et al.*[110] noted that confining Ru particles inside tubes enhanced dissociative CO adsorption and activity. Residual Fe nanoparticles from CNT synthesis can be activated *in situ* to

Table 4 Comparison between SWCNTs and MWCNTs in electrocatalysis

	SWCNTs		MWCNTs	
Aspect	Advantages	Disadvantages	Advantages	Disadvantages
Electrocatalytic activity	■ Higher electrochemically accessible surface area (ECSA), often twice that of MWCNTs ■ Unique bundled 'groove' structures enhance O_2 adsorption and accelerate ORR kinetics ■ Confinement effects enable reaction-pathway steering and selectivity control (*e.g.*, selective HOR over ORR)	■ Prone to bundling, which can reduce effective surface area if dispersion is poor	■ High electrical conductivity in isolated tubular morphologies ■ Triple-walled CNTs can show peak alcohol-oxidation activity due to inter-wall electron tunneling	■ Lower intrinsic activity and ECSA because inner walls are electrochemically inaccessible ■ Lack of surface grooves limits gas adsorption efficiency
Stability & durability	■ Good chemical stability under moderate electrochemical conditions	■ Susceptible to carbon corrosion at high potentials (1.0–1.5 V) and elevated temperatures (250 °C) ■ High curvature induces C–C bond strain, increasing vulnerability to thermal and electrochemical oxidation	■ Superior electrochemical durability due to multilayer graphitic stacking and larger diameters ■ Outer walls act as a 'sacrificial layer', preserving overall structural integrity	■ Defect-rich outer walls in some variants may trigger gradual degradation
Cost & scalability	■ High sensitivity enables efficient performance at ultra-low noble-metal or PGM-free catalyst loadings	■ Higher cost and greater difficulty in purification and large-scale production	■ Economically competitive and well-suited for mass production; mature large-scale CVD synthesis technologies	■ Often contain higher residual metal impurities, requiring aggressive acid purification
Structural & functional attributes	■ High structural flexibility enables formation of self-standing, binder-free electrodes	■ Highly prone to intermolecular aggregation and bundling due to strong π–π interactions	■ Greater structural rigidity preserves isolated tubular morphology	■ Inherently stiff and rigid structures that do not form the unique bundled "groove" nanospaces characteristic of SWCNTs
	■ Higher electroactive concentration makes them superior for electrochemical sensing ■ Inner-space tunability allows electronic-state engineering for selectivity control	■ Bundling can block internal cavities and hinder reactant (*e.g.*, H_2, O_2) transport to active sites ■ Reduced effective surface area if dispersion is not well controlled	■ Thermal oxidation onset temperature is a reliable predictor of long-term electrochemical lifespan ■ Mechanically robust scaffold for harsh electrochemical environments	■ Absence of groove-induced confinement leads to nonspecific and less efficient gas adsorption (*e.g.*, for ORR)

form Fe@CNT supports active for both the reverse water–gas shift (RWGS) reaction and FTS, utilizing CO_2 as a feedstock for hydrocarbon production. Differences in conversion and selectivity have been observed for Fe nanoparticles deposited on the outside surface *versus* within the hollow interior of CNTs (Fig. 9a).[125]

Akbarzadeh *et al.*[126] investigated the impact of thermal pretreatment (up to 900 °C) on MWCNTs after acid treatment, demonstrating that up to 70% of cobalt oxide nanoparticles could be deposited within the CNT channels. Xing *et al.*[127] also achieved controllable encapsulation of Co clusters within CNT channels (up to 80%) by tuning the thermal treatment temperature (optimal 650 °C) of the acid-treated CNTs. This pronounced confinement yielded the highest CO conversion (89.3%), C_{5+} selectivity (83.7%), and lowest CH_4 selectivity, confirming that sequestering the active phase enhances long-chain hydrocarbon growth. Furthermore, studies focusing on stability have shown that CNT-supported catalysts are more stable. Chernyak *et al.*[118] demonstrated that Co/CNT systems exhibited remarkable stability (>500 h) and showed that sintering during the initial reaction phase actually increased activity and C_{5+} selectivity by converting less active ultra-small particles into larger, more efficient ones. Pendyala *et al.*[110] studied the effect of nitric acid treatment on CNT supports for Ru catalysts in FTS. Acid treatment removes impurities, introduces oxygen-containing groups (which serve as anchoring sites), opens the ends of CNTs, and breaks tubes at defects, shortening the diffusion path for Ru nanoparticles and enabling stable and efficient deposition inside the channel (Fig. 9b). This treatment resulted in heightened catalytic activity and enhanced selectivity toward alcohols and liquid hydrocarbons (C_5^+), while reducing methane selectivity. The electron-deficient concave CNT surface is hypothesized to weaken the bonding strength of RuO_2, facilitating the activation of Ru species within CNT channels and lowering the reduction temperature. Pour *et al.*[120] showed that functionalization of CNTs (*e.g.*, with H_2O_2 and sonication) enhances the interaction between Co species and the inner CNT surface,

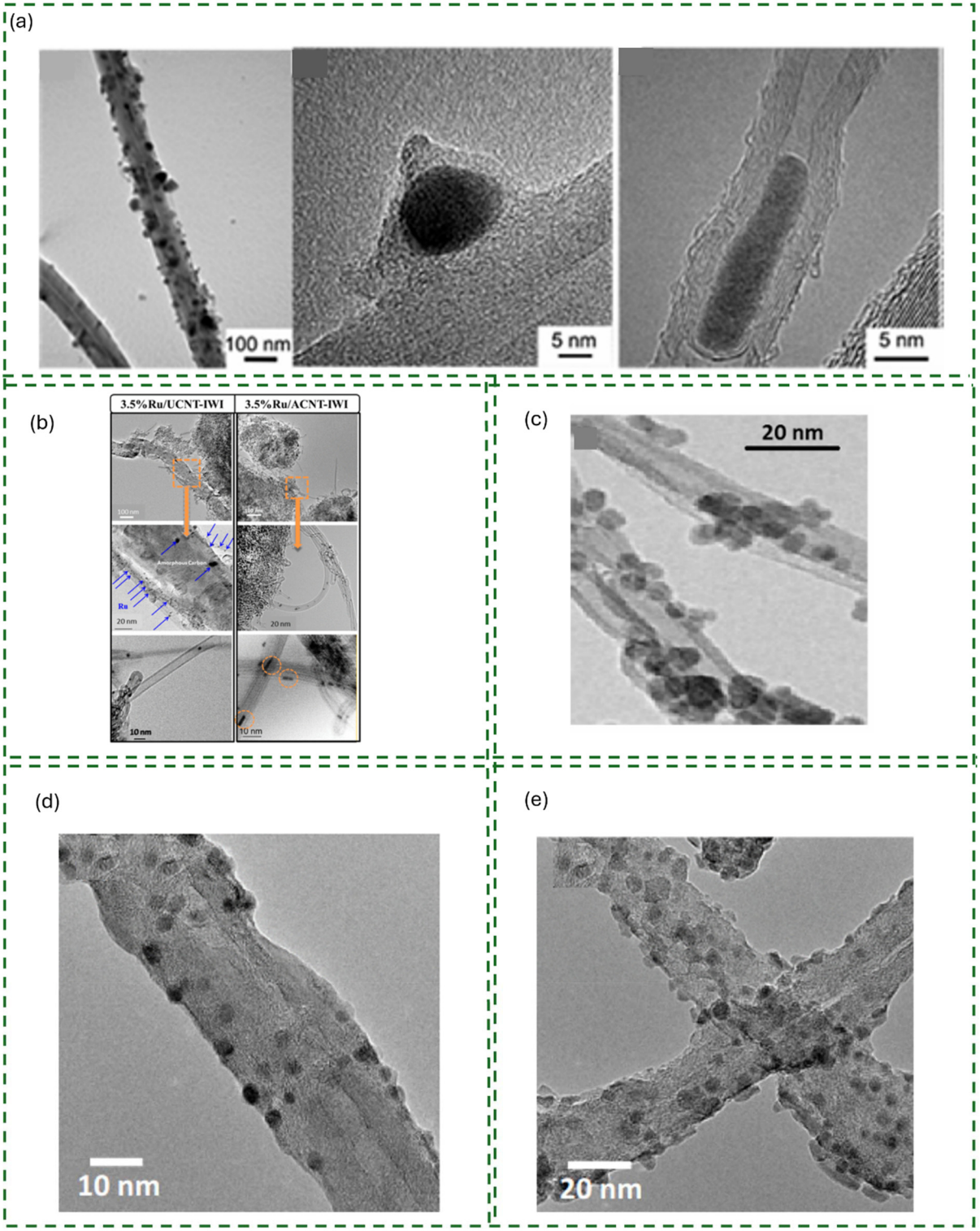

Fig. 9 (a) TEM micrographs of as-produced CNTs showing the presence of Fe nanoparticles.[125] (b) TEM and HR-TEM images of Ru/UCNT-IWI and Ru/ACNT-IWI catalysts with increasing magnification.[110] (c) A TEM image of calcined Co-FCNT-10 catalyst.[120] (d, e) Low- and high-magnification TEM images of fresh Fe/CNT-Fenton catalyst.[119] Figure a reprinted from ref. 125 *Catal. Sci. Technol.*, 2014, **4**, 3351–3358, with permission from Royal Society of Chemistry, copyright 2026. Figure b reprinted from ref. 110 *Ind. Eng. Chem. Res.*, 2017, **56**, 6408–6418, with permission from American Chemical Society, copyright 2026. Figure c reprinted from ref. 120 *Ind. Eng. Chem. Res.*, 2018, **57**, 13639–13649, with permission from American Chemical Society, copyright 2026. Figures d–e reprinted from ref. 119 *J. Catal.*, 2018, **361**, 278–289, with permission from Elsevier, copyright 2026.

thereby increasing the capillary force for injecting nanoparticles into the channels (Fig. 9c). For instance, a Co/FCNTs-10 catalyst (with 10 s sonication pulses) exhibited higher FTS activity and a lower activation energy (92.1 kJ mol^{-1}) compared to a non-sonicated Co/CNTs catalyst (102.7 kJ mol^{-1}). Liu *et al.*,[53] however, showed that alternative chemical modification routes are highly effective. They investigated Fe/CNT catalysts treated by urea/NaOH and attributed the catalyst performance (superior stability and remarkable diesel selectivity (52%)) to the synergistic effect of NaOH and urea, which resulted in pyrrolic N incorporation, high graphitization degree, facile reduction, structural integrity, and a strong metal–support interaction. The ability of this catalyst to achieve 90.8% C_{5+} selectivity and 52% diesel selectivity surpassed the maximum value (29%) predicted by Anderson-Schulz-Flory (ASF) distribution for diesel hydrocarbons.

Almkhelfe *et al.*[119] investigated the synthesis and performance of FTS catalysts supported on CNTs using a modified photo-Fenton process, highlighting the unique and superior role of CNTs compared to conventional oxide supports. Based on the TEM results from the study (Fig. 9d and e), the CNTs promote high catalyst dispersion and produce small, uniform catalyst particles (2–5 nm) when used with the photo-Fenton process, which results in a significant increase in the number of active sites available for the FTS reaction. The high thermal conductivity of CNTs is crucial for dissipating heat generated during the exothermic FTS reaction, thereby effectively minimizing the temperature gradient across the reactor bed and reducing the susceptibility of the catalyst to sintering and deactivation. Results from the study show that the physical stability, thermal management, and chemical inertness of CNT result in superior catalytic performance, with photo-Fenton prepared Co/CNT catalysts achieving high CO conversion (~80%) and good selectivity for liquid hydrocarbons (C_{5+}, ~70%) at low FTS reaction temperature (200 °C). In bimetallic and promoted systems, CNTs offer sophisticated control over electronic and structural promoters. Incorporating CNTs to conventional FTS catalysts often leads to improved performance, including higher activity per unit volume and enhanced selectivity to olefins[125] Yahyazadeh *et al.*[128] optimized a promoted system (0.5K-5Mo-10Fe/CNTs), which resulted in the highest overall olefin yield (35.5%). They found that Mo enhanced light olefin selectivity and Fe dispersion by creating structural defects on the CNTs, whereas K boosted CO conversion and favored the formation of active Iron carbides. Table 5 is a summary of the essential properties of CNTs and their influence on the catalyst function during FTS.

CNTs, as highly active and tunable supports, provide superior performance when compared to conventional oxidic supports. Table 6 presents a comprehensive comparison of catalysts supported on CNTs and on traditional metal oxides, highlighting the advantages of CNT-supported catalysts.

In general, metal particles encapsulated within CNT cavities are typically more stable, exhibit higher catalytic activity, and experience less carbon deposition.[120,124,129,130] The electron deficiency on the inner CNT surface weakens metal–oxide bonds, favoring reduction and the presence of highly active metallic sites.[110,130] Acid treatment introduces oxygen-containing groups (*e.g.*, hydroxyl, carboxyl) on CNT walls, improving hydrophilicity and providing anchoring sites for metal nanoparticles, which enhances dispersion.[112,124,131] Nitrogen-doping in CNTs introduces pyridinic nitrogen species that enhance the electronic properties of the support, facilitate metal reduction, and increase active site density.[132] Table 7 presents the activity, selectivity, and stability of CNT-based catalysts in FTS.

4.3 Reforming of hydrocarbons

The catalytic application of CNTs in hydrocarbon reforming reactions, such as dry reforming of methane (DRM), steam reforming (SR) of alcohols and glycerol, and variations including oxy-steam reforming, leverages the unique physicochemical properties of CNTs to enhance catalytic performance, stability, and product selectivity. The CNT surface serves as an active promoter for hydrogen spillover, facilitating the transfer of activated H-species from metal sites to the support, thereby

Table 5 Summary of CNT properties and their influence on catalyst performance during FTS

CNT property	Influence on catalyst performance
Confinement effect/curvature	Encapsulation of metal particles restricts sintering and aggregation, enhancing catalyst stability. Confinement significantly increases the residence time of intermediates within the channels, promoting successive chain-growth steps for heavy hydrocarbons (C_{5+} and wax)
Electronic structure/reducibility	The π-electron density shift from the inner concave surface to the outer convex surface of the CNT wall results in electron-deficient inner surfaces. This causes weaker metal–oxygen bonds in oxides situated internally, facilitating facile autoreduction to the active metallic or carbide phase. CNTs generally provide weak metal–support interactions that prevent the formation of inactive, hardly reducible metal aluminates or silicates common to oxide supports
Surface defects and functionalization	Chemical treatments (like acid, urea/NaOH) introduce surface functional groups (COOH, C═O) and defects (kinks, broken caps). These defects act as crucial anchoring sites for metal precursors, enhancing metal dispersion and reducing sintering, even when initial metal loadings are high
N-doping (pyrrolic/quaternary N)	Incorporating nitrogen atoms creates an electron donor effect. This transfers charge to the transition metal, weakening the C═O bond, which enhances CO adsorption, activation, and cleavage efficiency. N-doping significantly enhances FTS activity and favors higher C_{5+} selectivity due to increased surface basicity
Degree of graphitization	A high degree of graphitization facilitates electron transfer between the metal active species and CO molecules, contributing directly to the activation of CO and thus boosting FTS reaction activity

Table 6 Comparison between CNT-supported catalysts and conventional metal oxide-supported catalysts for FTS

Feature	CNT-supported catalysts	Oxide-supported catalysts
Activity	Generally, exhibit higher FTS activity and conversion rates due to high metal dispersion and enhanced reducibility	Formation of hard-to-reduce species lowers the active metal concentration, thereby reducing intrinsic activity
Selectivity	High tunability and excellent C_{5+} and diesel selectivity (up to 93.8% C_{5+}) are achieved through confinement and N-doping/promotion. CH_4 selectivity is typically low, although increasing Co dispersion (*i.e.*, smaller particles) can increase CH_4 selectivity	High methane selectivity is a common drawback for unpromoted Fe catalysts. Selectivity is often constrained by ASF limitations unless optimally promoted
Olefin/paraffin ratio	Can achieve superior olefin/paraffin ratios through surface defect engineering, which inhibits secondary hydrogenation. The C_2–C_4 olefin/paraffin ratio positively correlates with C_{5+} selectivity	Generally, results in lower olefin selectivity due to a lack of electronic and structural promoters
Reducibility/carburization	High reducibility due to weak interaction or electronic effects. CNT structures can promote rapid and selective formation of active carbide phases	Strong metal–support interactions lead to the formation of inactive mixed oxides, requiring higher reduction temperatures
Resistance to deactivation	High resistance to sintering due to confinement and anchoring sites. The primary deactivation mechanism is often wax accumulation, but activity can be restored *via* mild regeneration	Susceptible to sintering and permanent deactivation due to the formation of non-reducible spinel phases

Table 7 Application of various CNT-based materials for Fischer–Tropsch synthesis

Nanomaterial	Application	Activity	Selectivity	Stability	Ref.
CNT, functionalized CNT	FTS	Increased FTS rate from 0.64 to 0.78 g HC $g_{cat.}^{-1}$ h^{-1} (micro-emulsion *vs.* common CNT)	+7.4% C_{5+}; −44% CH_4; C_{5+} = 85% with 3–4 nm crystallites	Uniform Co inside CNT prevents sintering, stabilizes activity	122
N-doped CNT	CO hydrogenation to higher alcohols	Improved CO conversion; max alcohol selectivity 27.2% *vs.* 20.2% (CNT)	68.8% C_{2+} –OH *vs.* 30.2% (CNT); methanol selectivity reduced from 69.8% → 31.2%	Stable at 300 h; N-doping stabilizes Rh species	115
Carbon-encapsulated Co & Fe in CNT framework	FTS	TOFs: Co 0.10–0.14 s^{-1}, Fe ∼ 1.0 s^{-1} (highest among unpromoted)	High C_{5+}; Fe1200 lower CO_2 selectivity	Carbon shells prevent oxidation & sintering; no pre-reduction needed	113
MWCNTs, OCNTs, NCNTs	High-temp FTS	NCNT-supported Fe: high/constant CO conversion over 80 h	High olefin selectivity; C_2–C_4 & C_{5+} + increases with particle size	Strong Fe–N interaction prevents oxidation; less severe sintering *vs.* untreated OCNT	133
CNTs (synthesized *vs.* commercial)	FTS (light olefins)	20Fe/CNTs-synthesized: CO conversion 90.4%	Light olefins 23.6%; C_{5+}: 21.6% *vs.* 5.8% (commercial CNT)	Acid treatment increases hydrophilicity, prevents sintering, and increases stability	116
OMC, AC, CNT	FTS	CNT-supported catalyst showed the highest FTS activity; Ru–OMC (autoreduction) > Ru/OMC (IWI)	Ru–OMC high product selectivity	Ru nanoparticles embedded, stable; OMC structure retained	134
CNT, oxCNT	FTS	TOF: CNT 150 × 10^{-3} s^{-1} *vs.* oxCNT 63 × 10^{-3} s^{-1}	C_{5+}: CNT 82% *vs.* oxCNT 78%	oxCNT anchors Co, prevents sintering; CNT is more prone to growth	135
CNTs	FTS	Co/CNT ≫ oxide supports; high activity, high TOF	C_{5+} increases, CH_4 decreases with sintering	Deactivation mainly by wax accumulation; activity recoverable by regeneration	118
CNTs (Mn-promoted/unpromoted)	FTS	High activity due to open morphology, low diffusion limits	Mn promoter improved selectivity	Good sustained performance (deactivation not detailed)	136
CNTs (acid-treated *vs.* untreated)	FTS	ACNT-IWI catalyst: highest activity	Oxygenates ∼17% (ACNT-IWI) *vs.* 10–12% others; higher C_{5+}	Acid treatment anchors Ru, enhances confinement & stability; CVD catalyst deactivated faster	110
CNTs, functionalized CNTs (sonicated)	FTS	Co/FCNTs-10 > Co/CNTs, Co/FCNTs-20; E_a: 92.1–102.7 kJ mol^{-1}	FTS rate increases, C_1–C_4 increases, and C_{5+} decreases	Narrow particle distribution enhances stability	120
MWCNTs (pretreated, acid-treated)	FTS	Co/CNT pretreated @ 900 °C, CO conversion 58.7%	C_{5+} (83.2%); CH_4 decreases from 44.3% to 9.5%	Acid treatment uncaps CNTs, improves dispersion, and stabilizes Co	121

accelerating dehydrogenation and increasing H_2 selectivity.[137,138] The high electrical and thermal conductivity of the sp^2-hybridized framework enables CNTs to act as efficient energy transducers for microwave or Joule heating, ensuring uniform thermal distribution that enables stable low-temperature operation and rapid chemical bond breaking for higher hydrogen yields.[139,140] Also, the tunable surface chemistry provided by defects and functional groups allows for high metal dispersion and increased surface basicity through doping, which promotes the chemisorption and activation of reactants such as CO_2.[141–143] Moreover, the CNT curvature creates an electron-deficient interior that weakens metal–oxygen bonds to enhance reducibility and modify adsorption strengths for improved activity.[9,141] Recent studies have focused on leveraging the confinement effect and tunable surface chemistry of CNTs to mitigate common catalyst deactivation issues such as sintering and carbon deposition. As shown in Table 8, the main advantage of CNT-supported catalysts over conventional oxide supports (*e.g.*, CeO_2, Al_2O_3, SiO_2, and MgO) lies in their multifunctional nature. While oxides such as CeO_2 are valued for their oxygen storage capacity and Al_2O_3 for its surface area, they often fail to prevent the sintering and coking that occur at high reforming temperatures.

4.3.1 Dry reforming of methane (DRM). DRM is a crucial technology that converts two greenhouse gases, CH_4 and CO_2, into syngas (H_2 and CO), contributing to emission reduction and clean energy production.[132,144] However, the highly endothermic nature of the reaction necessitates high temperatures, which often lead to sintering and carbon deactivation of conventional Ni-based catalysts.[132] Several studies (Table 9) involving CNT-supported catalysts for DRM have demonstrated the profound impact of active-site localization and promoter incorporation. Ma *et al.*[9] reported that Ni nanoparticles loaded inside CNTs (I–Ni/CNTs) (Fig. 10a and b) exhibited higher catalytic activity and stability in DRM (Fig. 10e–g) than those loaded on the exterior surface (O–Ni/CNTs) (Fig. 10c and d). The I–Ni/CNTs were found to be easier to reduce by H_2 (T_{red} 293 °C) compared to O–Ni/CNTs (T_{red} 320 °C). This difference is attributed to the electron density of CNTs and confinement effects that promote the reduction of NiO species to metallic Ni by H_2. Specifically, I–Ni/CNTs suppressed carbon accumulation, with a total carbon deposition of 9.3% compared with 20.8% for O–Ni/CNTs, in which graphitic carbon formed. Jiang *et al.*[141] successfully synthesized cobalt nanoparticles anchored on nitrogen-doped CNTs (Co/N-CNTs) for DRM and proposed that pyridinic N and carbon defects synergistically promote DRM activity. The optimal Co/N-CNTs catalyst achieved peak conversions of 92.9% for CH_4 and 96.4% for CO_2 at 800 °C, significantly surpassing the undoped catalyst. N-doping amplified the strong interaction between Co species and CNT support, which benefited CH_4 and CO_2 conversions and strengthened coke resistance. Furthermore, pyridinic N species enhanced CO_2 chemisorption and stabilized the H_2/CO ratio close to 1.

Donphai *et al.*[145] found that Ni/CNT catalysts exhibited higher stability than Ni/SiO_2 over a 24 h test period. This stability was attributed to a mechanism in which carbon deposits selectively form as extensions of the existing CNT tube length, following a tip-growth mechanism, thereby preserving the active Ni sites on the catalyst surface. Wang *et al.*[146] demonstrated that the $Ni/80CNT/CeO_2$ catalyst showed excellent stability for 50 hours, with no carbon deposition encapsulating the Ni nanoparticles, because the localized "hot spots" facilitated CH_4 dissociation and reaction with CO_2 at lower bulk tempera-

Table 8 Comparison between CNT-supported catalysts and oxide-supported catalysts for the reforming of hydrocarbons

Feature	CNT-supported catalysts	Oxide-supported catalysts
Electronic properties	The unique π-electron density shift from concave inner to convex outer surfaces creates an electron-deficient interior that enhances metal reducibility and modifies adsorption	Rely on intrinsic redox cycles (*e.g.*, Ce^{4+}/Ce^{3+}) or lattice oxygen mobility to facilitate oxygen transfer and activation
Thermal & electrical conductivity	High thermal conductivity prevents 'hotspots'; high electrical conductivity enables novel energy transduction such as Joule (self-heating) or microwave-driven processes	Generally, function as thermal insulators or poor conductors, often leading to temperature gradients and lower energy efficiency in conventional furnaces
Pore structure & mass transfer	Mesoporous structure with regularized channels significantly reduces mass transfer resistance, allowing reactants and products to diffuse easily	Porous structure can vary; conventional oxides like Al_2O_3 or SiO_2 may have narrower pore distributions that increase diffusion limitations
Stability (sintering)	The nano-confinement effect within CNT channels physically restricts metal nanoparticle mobility, effectively suppressing sintering and maintaining dispersion	Prone to metal sintering at high reforming temperatures, leading to larger particle sizes and a loss of active surface area
Coke resistance	Favors the growth of filamentous carbon (MWCNTs) that extends outward from the catalyst tip rather than blocking the active site	Frequently suffer from amorphous coke encapsulation, where carbon deposits cover active metal sites and lead to rapid deactivation
Chemical stability	Highly stable in aqueous environments and resistant to acidic or basic conditions, making them ideal for steam-rich environments	Some oxides, particularly alumina (Al_2O_3), are known to deactivate or degrade after prolonged usage under harsh reforming conditions
Surface chemistry	Surfaces can be tailored *via* functionalization (*e.g.*, nitric acid) or heteroatom doping (N, S) to improve hydrophilicity and metal anchoring	Surface properties like acidity/basicity are generally fixed by the material type, though they can be modified with specific promoters
Operational impact	Often enable low-temperature operation for reactions like SRE or GSR while maintaining high activity and selectivity	Typically require higher temperatures (>550 °C) to achieve appreciable conversions, which increases energy consumption and deactivation risks

Table 9 Application of various CNT-based materials for dry reforming of methane (DRM)

Nanomaterial	Application	Activity	Selectivity	Stability	Ref.
I–Ni/CNTs *vs.* O–Ni/CNTs MWCNTs	DRM of CH_4	At 750 °C: I–Ni/CNTs: 70.2% CO_2 conversion, 83.4% CH_4 conversion; O–Ni/CNTs: 58.9% CO_2 conversion, 75.6% CH_4 conversion	H_2/CO higher for I–Ni/CNTs; H_2/CO decreases over time; RWGS at 700 °C	I–Ni/CNTs more stable (65.4% CH_4, 78.8% CO_2 after 8 h) *vs.* O–Ni/CNTs (50.1% CH_4, 66.1% CO_2 after 8 h); lower carbon deposition inside CNTs	9
Co/N-CNTs	DRM of CH_4	Optimal Co/N-CNTs: 92.9% CH_4 conversion, 96.4% CO_2 conversion at 800 °C; undoped Co/CNTs: 33% CH_4, 49% CO_2	H_2/CO < 1; pyridinic N promotes DRM, H_2/CO ≈ 1 at 750 °C	Co/N-CNTs maintained ~68% CH_4, and 77% CO_2 conversion after 15 h; undoped deactivated in 3 h	141
Ni-CNTs/MS	DRM of CH_4	Slightly lower initial activity *vs.* Ni/MS; CH_4 & CO_2 conversions ↑ 3% after 24 h; higher TOF for 10Ni-CNTs/MS	Higher H_2/CO ratio *vs.* Ni/MS (less RWGS)	Improved stability: Ni/MS ↓ 10% conversion after 24 h, Ni-CNTs/MS ↑ 3%	145
CeSr@MWCNT/Co	DRM of CH_4	At 700 °C: Ni@MWCNT/Ni: 80.45% CH_4, 87.65% CO_2; CeSr@MWCNT/Co: 70.77% CH_4, 79.13% CO_2	H_2/CO = 4.1–5 (high, CO disproportionation suppressed)	Stable after 12 h on stream	129
Ni/80CNT/CeO_2	MW-assisted DRM	96.4% CO_2 conversion, 90.1% CH_4 conversion at ~40 W, 280 °C; much higher *vs.* Ni/CNT or Ni/CeO_2	H_2/CO = 2.8 (Ni/CeO_2, 10–30 W)	Stable for 50 h (CH_4, 76.7%, CO_2 90.1%); no carbon encapsulation	146
Ru/CNT	DRM of CH_4	High activity at 773–973 K, 3 atm; better than Pt–Pd/CNT	H_2/CO < 1 at 773 K (RWGS); ≈1 at 973 K	High stability; little sintering; slight coke at high temperature	147
Mo_2C-in-CNTs *vs.* Mo_2C-out-CNTs	DRM of CH_4	Mo_2C-in-CNTs > Mo_2C-out-CNTs; Ni/Co-modified stable at high WHSV (18 000 $cm^3\ g^{-1}\ h^{-1}$)	Stability linked to Mo_2C oxidation *vs.* recarburization balance	Mo_2C-in-CNTs: stable 23 h; Mo_2C-out-CNTs: deactivated after 13 h; Ni/Co-modified: stable 50 h	10
Ni/CNT, $CeZrO_2$/CNT, Ni–$CeZrO_2$/CNT	DRM of CH_4	Ni/CNT: 28% CH_4, 10% CO_2 at 450 °C; Ni lowers temperature onset (400 °C *vs.* 630 °C for NiCZ/CNT, 750 °C for CZ/CNT)	CO_2 > stoichiometry (RWGS, CO_2 deoxidation); H_2/CO < 1	$CeZrO_2$-containing catalysts resist coke; NiCZ/CNT maintained nanosized phases	148
Pd–Pt/CNT	DRM of CH_4	High activity at 773–923 K, 3 atm; CH_4 conversion 0.075, CO_2 conversion 0.091 at 773 K	H_2/CO ≈ 0.798 at 773 K (model); Cs presence ↑ H_2/CO ≥ 1	Minimal coke; Pt–Pd more stable than Pt-only	11
Ni and Fe inside/outside CNTs	DRM of CH_4	At 800 °C: 10Ni@CNT: 63% CH_4, 72% CO_2; 10Ni@CNT/5Fe: 67% CH_4, 88% CO_2; Fe promoted H_2	H_2/CO = 1.17 for 10Ni@CNT/5Fe; Fe promoted coke resistance & H_2 selectivity	Stable for 11 h (70% CH_4, 80% CO_2); CNT structure preserved	130

tures. Also, Gao *et al.*[10] reported that encapsulating Mo_2C nanoparticles within CNTs significantly enhanced the catalytic stability for DRM by increasing the oxidation resistance of the carbide material. The MO_2C-in-CNTs catalyst remained stable for 23 h compared to only 13 h for Mo_2C-out-CNTs. This approach, combined with Ni or Co modification, resulted in highly stable catalysts over a 50 h period.

CNT-based catalysts offer several advantages over traditional oxide supports such as Al_2O_3, SiO_2, and MgO. The intrinsic electronic properties of CNTs, with an electron-deficient interior and an electron-rich exterior surface, can lead to distinct catalytic performance depending on the location of the catalytic sites.[9] This influences the reducibility of metal oxides, such as the easier reduction of NiO inside CNTs.[9] CNTs possess high permittivity, allowing them to efficiently convert microwave energy into heat, creating localized "hot spots".[146] This enables DRM to occur at significantly lower bulk temperatures with reduced energy input compared to conventional heating, and notably, can suppress carbon deposition. Conventional CeO_2 supports, for example, exhibit much lower permittivity and are less effective at responding to microwaves.[146]

Figueira *et al.*[129] explored nanocomposites with Ce, Sr, and Co nanoparticles distributed both inside and outside MWCNTs. The functionalization of CNTs with nitric acid introduced oxygen-containing groups, reducing hydrophobicity and enabling the use of both organic and aqueous solvents, thereby facilitating control of the size and position of inserted particles. These catalysts achieved high conversions in DRM, with the presence of oxygen on the CNT surface favoring the oxidation process (removal of deposited carbon) and enhancing H_2 production, thereby increasing the H_2/CO ratio.

A nitrogen-doped CNT-loaded Ni catalytic system (Ni/NCNT) was developed by Tao *et al.*[132] to enhance active sites while maintaining the structural stability of the Ni/CNT system. Nitrogen doping was found to strengthen the metal–support interactions (MSI). Specifically, pyridinic nitrogen species synergistically interact with Ni particles, modulating the electronic environment on the CNT surface and increasing the active site density.[132] Khavarian *et al.*[144] reported that Co/CNT catalysts achieved higher CH_4 conversions and lower carbon deposition rates than Co/MgO, suggesting better resistance to deactivation. TEM images confirmed that most cobalt oxide nanoparticles were confined inside the CNTs. Afandi

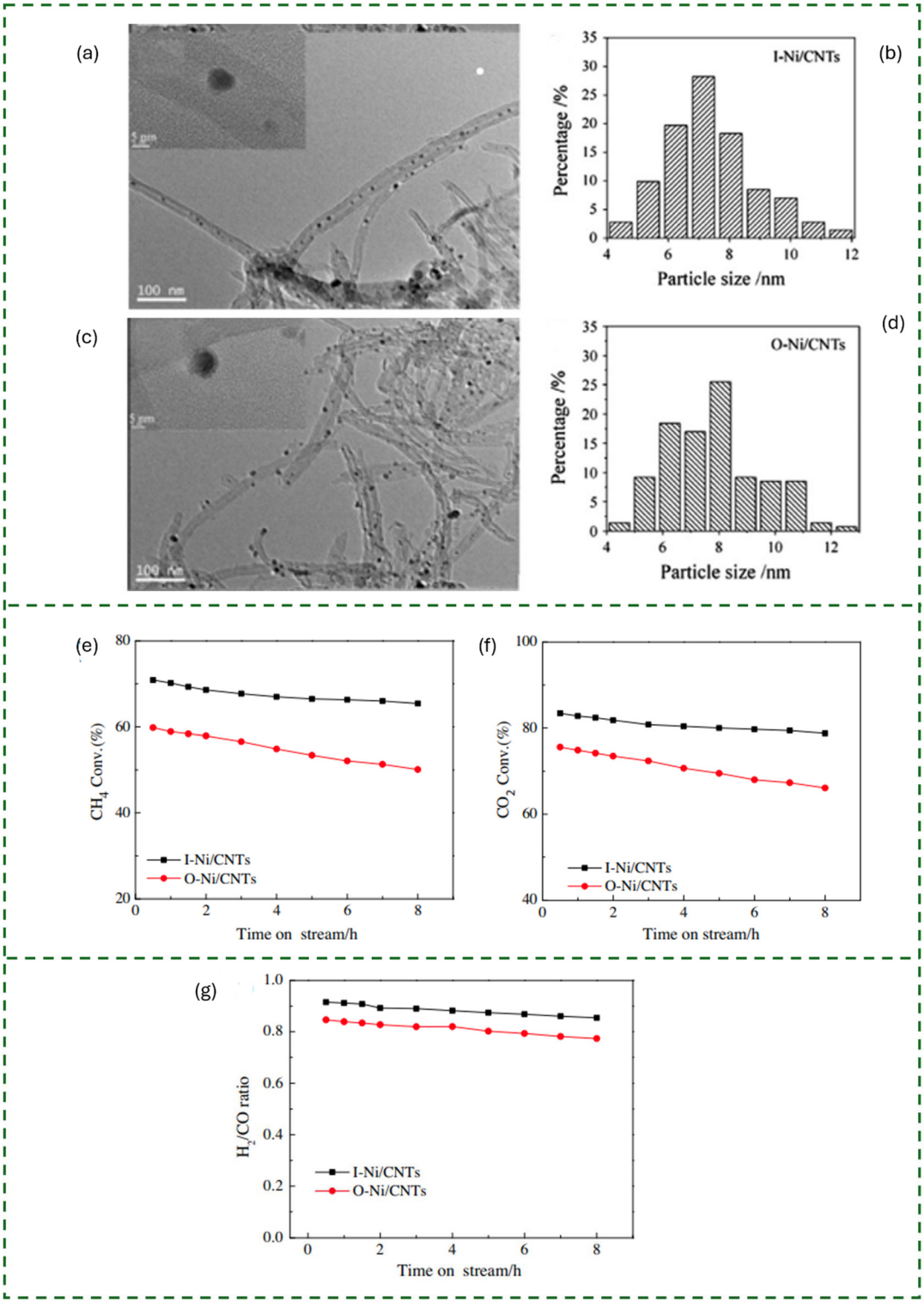

Fig. 10 TEM images and particle size distribution of (a, b) I–Ni/CNTs and (c, d) O–Ni/CNTs. Catalytic stability of I–Ni/CNTs and O–Ni/CNTs: (e) CH_4 conversion; (f) CO_2 conversion; (g) H_2/CO ratio. (Reaction conditions: 750 °C, W/F = 1 g h mol^{-1}.)[9] Figures a–g reprinted from ref. 9 *Fuel*, 2013, **108**, 430–438, with permission from Elsevier, copyright 2026.

et al.[131] evaluated four different synthesis methods for Ni–Ce nanoparticles supported on functionalized MWCNTs (fCNT) for CO_2 reforming of methane (CDRM). The hydrothermal method (NiCe/fCNT(H)) yielded the highest catalytic activity (92% CH_4 and 96% CO_2 conversions at 800 °C) and the lowest carbon growth (only 2%). This superior performance was

attributed to the well-dispersed nanoparticles and the abundance of oxygenated groups on the fCNT surface. The acid treatment introduced defects and oxygen functionalities, making the MWCNT surface hydrophilic and providing active sites for metal attachment. The different CNT-based catalysts used for DRM, with their activity, selectivity, and stability, are summarized in Table 9.

4.3.2 Steam reforming (SR) of hydrocarbons. CNT-supported catalysts show exceptional promise across various steam reforming (SR) reactions, often enabling lower operational temperatures and improved selectivity. Seelam *et al.*[149] compared Ni, Co, Pt, and Rh catalysts supported on CNTs for steam reforming of ethanol (SRE) at low temperatures (150 °C to 450 °C). The Ni/CNT and Co/CNT catalysts exhibited the highest activity and selectivity for H_2 production. Notably, the Ni/CNT achieved almost complete ethanol conversion at 400 °C. The Co/CNT catalyst was particularly effective, yielding low concentrations of Co and CH_4, favoring steam reforming pathways over decomposition reactions. Yang and Liao[150] successfully prepared Cu/ZnO-CNTs catalysts for methanol steam reforming (MSR) using chemical reduction and wet impregnation, noting that acid pretreatment of the CNT surface was vital to create functional groups and improve hydrophilicity. An optimized Cu/ZNO-CNTs catalyst yielded nearly 100% H_2 above 320 °C. Similarly, they synthesized Ni–Cu alloys[151] supported on CNTs for MSR, achieving a high H_2 yield of 98.7% at 360 °C.

Zhou *et al.*[152] systematically studied bimetallic NiCo/CNTs catalysts for glycerol steam reforming (GSR) by controlling the distribution of Ni and Co species. The Ni(i)Co(i)/CNTs catalysts, where both metals were confined inside the CNT channels, displayed the best catalytic activity and stability, attributed directly to the confinement effect. The sintering degree of the confined particles increases by only 41.1% after reaction, which is lower than the 238.5% increase observed for external loading (Ni(o)Co(o)/CNTs). Confinement also minimized coke accumulation, yielding only 0.28 mgC $g_{cat.}^{-1}$ for Ni(i)Co(i)/CNTs compared to 1.77 mgC $g_{cat.}^{-1}$ for external loading. Yadav and Vaidya[153] investigated Ni/CNT and Co/CNT catalysts for butanol steam reforming (BSR) at high temperatures (350 °C to 500 °C). They found that Ni/CNT was the superior catalyst, achieving 87.3% butanol conversion and H_2 yield of 0.75 mol mol^{-1} at 500 °C. The higher activity of Ni/CNT compared to Co/CNT in BSR was ascribed to the stronger efficiency of Ni in cleaving the longer C–C chain bonds present in butanol. Table 10 summarizes key advances in the catalytic application of CNTs to hydrocarbon reforming.

5. CNT-based catalysts for environmental remediation and food safety

CNTs have emerged as essential materials in heterogeneous catalysis for gas- and liquid-phase environmental remediation, functioning not only as supports but as multifunctional components that actively influence reaction mechanisms, thermal stability, and electronic properties.[6] The high specific surface area and mesoporous structure of CNTs facilitate the high dispersion of nanosized active sites and improve mass transfer efficiency by allowing reactant macromolecules to easily penetrate and adsorb onto the catalyst surface.[6,7] Also, the introduction of defects increases acidic or basic site strength to promote the adsorption and activation of gaseous pollutants such as NO_x or CO_2 and other hazardous pollutants, while inducing the formation of surface oxygen vacancies that accelerate reaction kinetics and lower activation energies.[155,156] The intrinsic chemical reactivity of the carbon lattice allows CNTs to function as stoichiometric reducing agents for NOx degradation in oxygen-lean environments, where the support itself participates in the reaction to prevent active site saturation.[157]

Photocatalysis, in particular, is an effective and eco-friendly method for air purification, wastewater treatment, and the inactivation of pathogens.[158,159] The photocatalytic process is initiated when a semiconductor is exposed to photons of appropriate wavelength ($\lambda \geq$ bandgap of semiconductor), resulting in the generation of reactive charge carriers (electrons and holes) that drive chemical reactions.[160] The holes (h^+) in the valence band have a sufficiently positive potential and thus generate OH* radicals from the adsorbed water molecules, while the electrons (e^-) in the conduction band, with a sufficiently negative potential, reduce the adsorbed oxygen to form superoxide radical ($O_2{}^{*-}$). The ROS (OH* and $O_2{}^{*-}$) are highly effective at degrading pollutants or inactivating microorganisms.[161–163] The mild reaction conditions, use of light for activation, low cost, and potential for large-scale application are among the benefits of photocatalysis. The photocatalytic efficiency depends on the competition between two main processes: electrons that react with adsorbed O_2 and the electron–hole recombination that releases phonons. It is estimated that most photogenerated electron–hole pairs recombine within 10 picoseconds (ps), which is extremely fast compared to the 100 ps usually required for redox reactions.[164] As a result, only a small fraction (~10 percent) of the photogenerated charges is available to participate in ROS generation.[164,165] Photocatalysis, therefore, suffers from rapid electron–hole recombination, which diminishes its efficiency, and form a wide band gap in some photocatalysts (especially the gold standard, TiO_2), which confines its photoactivity to the UV range.

To address the limitations of photocatalysts, studies have mainly focused on coupling with metal/semiconductor to form Schottky barriers or heterojunctions[167–169] and doping with cations/anions to impart visible light activity. For instance, coupling TiO_2 with a material that has a higher work function, such as graphene or CNTs, can suppress charge recombination. The high electron transport and storage properties of CNTs can serve as an electron reservoir, decreasing the recombination probability of the photogenerated charges in the hybrid material and enhancing activity. Work functions of CNTs are in the range of 4.45–5.27 eV, which are more positive than that of TiO_2 with a lower work function conduction band

Table 10 Recent advances in CNT-based catalysts for hydrocarbon reforming reactions

Reaction	Study	Key finding	Mechanism	Ref.
Dry reforming of methane (DRM)	Ni nanoparticles confined inside (I–Ni/CNTs) *versus* deposited outside (O–Ni/CNTs) CNTs	I–Ni/CNTs exhibited higher activity and superior stability. NiO confined inside CNTs was reduced at a lower temperature (293 °C) than external NiO (320 °C)	CNT confinement effects modify the electronic environment, enhancing metal reducibility and significantly suppressing carbon deposition (9.3% inside *vs.* 20.8% outside)	9
	Co nanoparticles supported on N-doped CNTs (Co/N-CNTs)	Optimized Co/N-CNTs achieved 92.9% CH_4 and 96.4% CO_2 conversion at 800 °C, with improved stability over undoped CNTs	Pyridinic-N and defect sites act synergistically: N sites enhance CO_2 adsorption (basicity), while defects facilitate CH_4 activation, directly linking I_D/I_G ratio to DRM performance	141
	Mo_2C encapsulated inside CNTs (Mo_2C-in-CNTs) *versus* external loading	Encapsulated Mo_2C maintained stability for 23 h *vs.* 13 h for external Mo_2C; Ni or Co modification extended stability to 50 h	CNT encapsulation slows carbide oxidation and stabilizes the oxidation–recarburization cycle, enabling sustained DRM activity under CO_2-rich conditions	10
	Zr- or La-promoted Ni/CeO_2 catalysts for DRM with simultaneous MWCNT formation	Zr and La reduced coke deposition (down to 5.1 wt% for Zr) and promoted highly graphitized MWCNTs (I_G/I_D up to 1.59 for La)	Zr enhances oxygen mobility, while La increases surface basicity; both facilitate carbon gasification, minimizing deactivation while enabling filamentous carbon growth	142
Methanol steam reforming (MSR)	Cu/ZnO-CNTs and Ni–Cu alloy catalysts on CNTs	Acid-treated CNTs improved metal dispersion. $Ni_{20}Cu_{80}$/CNTs achieved ~100% H_2 yield at 360 °C, outperforming physically mixed catalysts	Ni–Cu alloying tunes ensemble and ligand effects, reducing excessive H adsorption on Ni and improving methanol reforming kinetics	150
	Ce- or Zr-promoted CuZn/CNTs *via* microwave polyol, co-precipitation, and impregnation methods	Microwave-polyol CeCuZn/CNTs achieved 94.2% conversion, 98.2% H_2 selectivity, and only 2.6% CO selectivity with excellent stability	Microwave synthesis yields ultra-small crystallites and high dispersion; CeO_2 oxygen storage suppresses coke and CO formation, producing high-purity H_2	154
Ethanol steam reforming (ESR)	Ni/CNT and Co/CNT catalysts, ZnO-promoted systems	Ni/CNT reached near-complete conversion at 400 °C; ZnO-promoted Ni/CNT achieved full conversion at 350 °C with <1% CO selectivity	ZnO promotes the water–gas shift reaction, converting CO to CO_2 and enhancing H_2 selectivity while suppressing carbon deposition	149
	NiFe-based CNT catalysts under microwave/Joule heating ($NiFeLa_5$/CNTs-2)	>97% ethanol conversion at 470 °C with low CH_4 and CO (~5 vol%). High-surface-area CNTs heated faster than highly graphitized CNTs	CNTs act as microwave susceptors, enabling low-temperature reforming; La promotes Ni–Fe alloying, basicity, reducibility, and anti-coking behavior	139
Glycerol steam reforming (GSR)	NiCo/CNTs with metals confined inside *versus* outside CNT channels	Fully confined Ni(i)Co(i)/CNTs showed the highest activity and stability, with minimal sintering (41.1% *vs.* 238.5% particle growth externally)	CNT nano-confinement physically restricts particle migration, effectively suppressing sintering and coke formation, the dominant deactivation pathways	152
	Ni/CNT catalysts with varying Ni loadings	15 wt% Ni/CNT achieved 86.4% conversion and 72.9% H_2 selectivity at 375 °C	Performance correlates with Ni surface density, confirming that exposed metallic sites govern C–C cleavage and WGS activity at low temperature	143
Butanol steam reforming (BSR)	Ni/CNT *versus* Co/CNT catalysts	Ni/CNT achieved 87.3% conversion and 0.75 mol mol^{-1} H_2 yield at 773 K, outperforming Co/CNT	Ni is more effective for breaking longer C–C bonds in butanol, underscoring the importance of metal choice coupled with CNT support stability	153

of *ca.* 4.0 eV. As illustrated in Fig. 11 by Zhang *et al.*,[166] three primary mechanisms detail the role of CNTs in semiconductors such as TiO_2: (i) electron scavenging – CNTs act as a sink for photogenerated electrons due to their high conductivity and storage capacity, as mentioned earlier, which inhibits electron–hole recombination and leaves excessive reactive holes on the TiO_2 surface for redox reactions; (ii) photosensitization – the semiconducting CNTs absorb light themselves and inject charge carriers (electrons and holes) into the conduction and valence bands of the TiO_2 to drive chemical processes; and (iii) band-gap modification – the formation of C–O–Ti bonds at the interface introduces new energy states within the TiO_2 band gap, enabling the composite to absorb longer wavelength photons from the visible light spectrum.

A key focus in advancing photocatalysis is the development of high-performance, cost-effective catalysts, often by incorporating nanocarbon materials, particularly CNTs, owing to their exceptional conductivity, high surface area, and ability to enhance charge separation and light absorption.[158,162,170,171] Choosing between MWCNTs and SWCNTs for specific photocatalytic applications depends on the desired properties of the CNTs. Table 11 outlines the advantages and disadvantages of both MWCNTs and SWCNTs in terms of photocatalytic activity, stability, cost, and structural & functional attributes.

5.1 Air purification

CNT-based photocatalytic materials play a crucial role in degrading gaseous pollutants, such as volatile organic com-

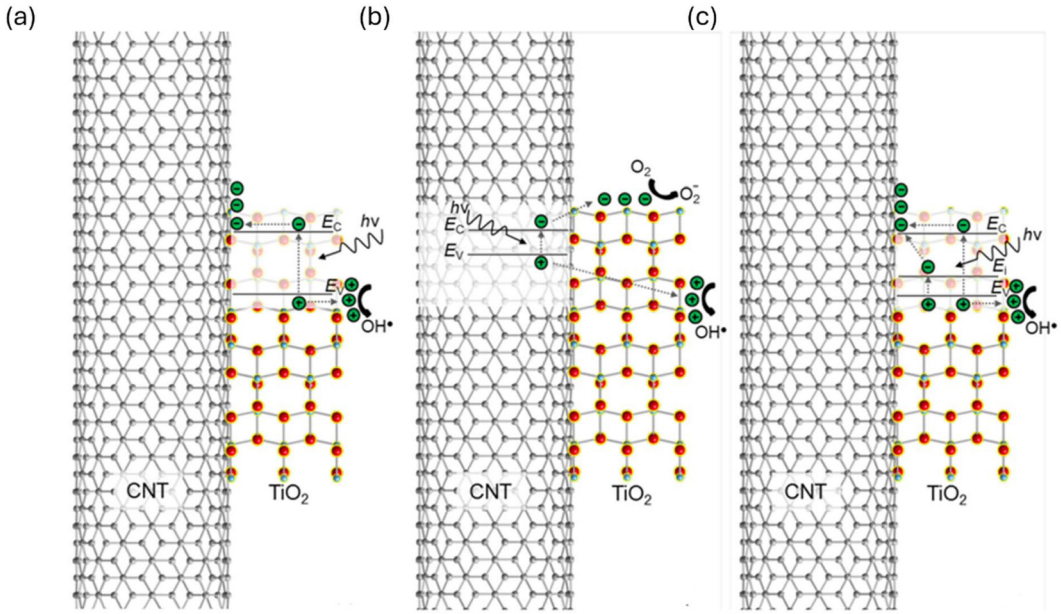

Fig. 11 Mechanism of TiO_2–CNT composite. (a) electron scavenging, (b) photosensitization, and (c) band-gap modification.[166] Figures a–c reprinted from ref. 166 *Beilstein J. Nanotechnol.*, 2014, **5**, 946–955.

Table 11 Comparison between SWCNTs and MWCNTs in photocatalysis

	SWCNTs		MWCNTs	
Aspect	Advantages	Disadvantages	Advantages	Disadvantages
Photocatalytic activity	■ High adsorption capacity and strong affinity for organic pollutants (*e.g.*, benzene, dyes) due to higher specific surface area	■ Lower light-to-heat conversion efficiency (~95%)	■ Superior solar harvesting and light-to-heat conversion (~99% absorbance) ■ Possesses self-cleaning and broadband absorption abilities	■ Generally lower specific adsorption capacity for organic contaminants compared to SWCNTs
Stability & durability	■ High tensile strength (~270 MPa) when organized into densely packed bundles	■ Vulnerable to structural changes if not properly supported	■ Robust stability against structural collapse and aggregation due to rolled graphene shells ■ High resistance to corrosive/oxidizing environments	■ Structural integrity can be impaired by the introduction of certain metallic species during modification
Structural & functional attributes	■ Provides excellent penetration channels for water ■ Easily functionalized to become hydrophilic *via* oxygen groups	■ Smaller interior size makes the tube centers less suitable for the adsorption of larger molecules	■ Forms nano–micro hierarchical structures that trap light	■ Pure forms are prone to aggregation and poor dispersion in solvents due to van der Waals forces

pounds (VOCs) and nitrogen oxides (NO_x), in air-purification applications. Pristine CNTs and functionalized CNTs have different catalytic abilities. CNTs that have undergone modification, whether through oxidative pretreatment[157,172] or heteroatom doping (N-doping, *via* melamine for high N content and defects[155]), consistently demonstrate superior catalytic activity compared to pristine CNTs.[157]

TiO_2 is a commonly used photocatalyst for indoor VOC decomposition due to its chemical stability and low cost. However, as previously discussed, its photocatalytic activity is relatively low under visible light irradiation, limiting its practical application for direct visible-light utilization. Another major limitation of TiO_2 is the swift recombination of photogenerated electron–hole pairs, with most recombining within 10 picoseconds, which significantly reduces efficiency.[162] To overcome this limitation, coupling TiO_2 with CNTs can significantly enhance photocatalytic efficiency by inhibiting charge recombination.[162] Al Mayyahi *et al.*[162] found that combining TiO_2 with 1% MWCNT improves photocatalytic degradation of acetaldehyde under UV light (Fig. 12a–c). The increase in activity is attributed to increased porosity, enrichment of hydroxyl groups on the surface, and high dispersion of TiO_2

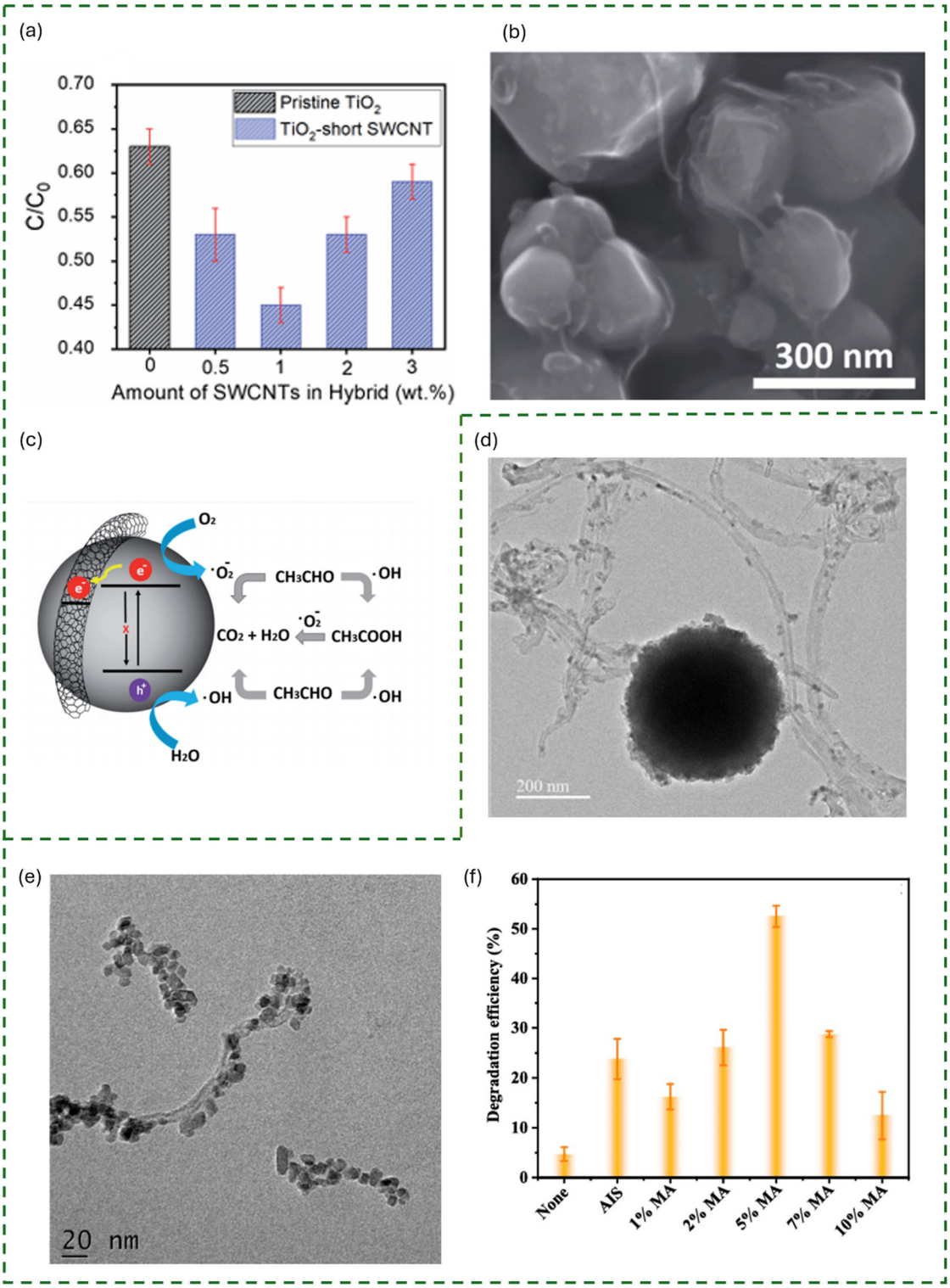

Fig. 12 (a) SEM image of TiO_2-short SWCNT, (b) photocatalytic degradation of gaseous acetaldehyde using TiO_2 and TiO_2-short SWCNT of different SWCNT loadings after 60 min, (c) schematic illustration of the possible mechanism of photocatalytic degradation of gaseous acetaldehyde.[162] (d) TEM images of 5% MA,[161] (e) photocatalytic degradation efficiencies with a 420 nm cut-off filter,[159] (f) HRTEM images of TCNT (0.5).[161] Figures a–c reprinted from ref. 162 *RSC Adv.*, 2021, **11**, 11702–11713. Figures (d) and (f) reprinted from ref. 161 *Diamond Relat. Mater.*, 2025, **157**, 112571, with permission from Elsevier, copyright 2026. Figure e reprinted from ref. 159 *Diamond Relat. Mater.*, 2025, **152**, 111904, with permission from Elsevier, copyright 2026.

particles. This is because MWCNTs act as electron sinks, facilitating the flow of photogenerated charge in TiO_2 and thereby increasing the lifetime of electron–hole pairs. Li *et al.*[161] synthesized MWCNTs-OH/$AgInS_2$ (MA) composite for visible-light photocatalytic degradation of high-concentration gaseous formaldehyde (1710 ppm). A 5% MA composite achieved a degradation efficiency of 67% after 2 hours of visible-light irradiation, enhancing the efficiency by 28% compared to unmodified $AgInS_2$ (Fig. 12d and e).

The enhancement is attributed to the enlarged specific surface area provided by MWCNTs-OH, which increases the number of active sites, and to their superior electrical conductivity, which facilitates efficient separation of photogenerated electron–hole pairs. MWCNTs-OH were found to accelerate electron-transfer kinetics and effectively suppress charge-carrier recombination. Joseph *et al.*[159] used hydrogen peroxide-functionalized MWCNTs (HP-CNTs) modified TiO_2 (TCNT(x)) nanohybrids for the visible-light reduction of nitrobenzene to aniline, and the redox synthesis of benzimidazoles (Fig. 12f). The TCNT (0.5) nanohybrid (0.5 wt% MWCNT) exhibited the highest photocatalytic activity, showing 100% conversion of substrates in a limited time with excellent selectivity. HP-CNTs contributed to visible-light sensitivity by shifting the absorption edge, serving as sensitizers, and enhancing substrate adsorption properties due to surface hydroxyl and carbonyl functionalities. They also possess excellent charge-transfer properties, thereby enhancing efficiency.

Beyond photocatalysis, electrocatalysis has also been explored for NO_x degradation. Kuo *et al.* synthesized a CNT-grafted TiO_2 nanocatalyst that exhibited NO oxidation activity triggered by either UV light (photocatalysis) or a DC voltage in dark conditions (electrocatalysis). The CNTs played a multifunctional role by improving electrical conductivity (13.65 S m^{-1}) and trapping photo-induced electrons, thereby reducing electron–hole recombination – a process that was dependent on the CNTs being grafted directly onto the TiO_2 surface rather than simply being mixed. Similarly, Xiao *et al.*[173] constructed CNT-threaded CeO_2 mesocrystals (Fig. 13a–d) for photocatalytic NO oxidation. The structure provided a three-dimensional conductive network that enhanced interfacial charge transport and stability, thereby increasing the concentration of surface Ce^{3+} species and oxygen vacancies. This electronic modification optimized the reaction towards the deep oxidation pathway, achieving high NO_3^- selectivity (93%) while severely limiting the toxic byproduct NO_2 (Fig. 13e–j).

Recent studies demonstrate the capability of CNT-supported catalysts in degrading VOCs and indoor pollutants under practical conditions. Lu *et al.*[6] investigated a cobalt-supported CNT (Co/CNT) catalyst for the catalytic oxidation of BTEX (including toluene) present in incineration flue gas at 250 °C, achieving stable and efficient removal (*e.g.*, 99% conversion for benzene when Pb was added to the feedstock). The sustained performance was attributed to the good dispersion of nanoscale cobalt particles (<10 nm) and the superior thermal stabilization and hydrophobic properties conferred by the CNT support, which prevented deactivation from water vapor and coke deposition. Similarly, Yuan *et al.*[174] developed a novel Pt@CNTS/SiC catalytic membrane for the simultaneous high-efficiency removal of formaldehyde (HCHO) and particulate matter (PM) at room temperature. They found that using a low reduction temperature (−80 °C) to deposit platinum resulted in extremely small Pt particles (0.5–3 nm), yielding superior HCHO degradation efficiency (up to 96% at 25 °C). The CNT membrane layer leveraged the large aspect ratio of CNTs to promote both HCHO degradation (adsorption and catalysis) and fine particle capture.

CNTs are instrumental in enhancing efficiency and modifying the mechanisms of NOx-degradation technologies, such as selective catalytic reduction (SCR) and catalytic decomposition. Li *et al.*[156] synthesized V_2O_5/TiO_2-CNT catalysts for NO_x SCR and observed a catalytic promotional effect exerted by CNTs. This effect was linked to increased catalyst acidity and reducibility, promoting efficient NH_3 adsorption and enhancing the oxidation of NO to NO_2, thereby facilitating fast SCR pathways. Also, Beyer and Köhler[157] critically investigated rhodium-supported CNT (Rh/CNT) catalysts and concluded that in the absence of excess oxygen, the CNT itself functions as the reducing agent for NO and NO_2 through stoichiometric oxidation. They further demonstrated that oxidative pretreatment of the CNT surface (Rh/CNT (ox)) increased the amount of labile oxygen compounds and defect sites, enhancing catalytic activity and lowering the quantitative NOx conversion temperature by 50 °C. Wu *et al.*[155] developed nitrogen-doped CNT (N-CNT) supported CuMgAl-LDO catalysts for low-temperature NH_3-SCR. The optimal catalyst (CuMgAl-LDO/N-CNT-M) achieved 93% NO_x conversion at 210 °C, owing its performance to N-derived defects, greater surface area, enhanced acidity, and an optimal valence distribution of Cu^+/Cu^{2+} species. Mechanistic studies confirmed that the N-doping accelerated NO activation, pushing the reaction toward the highly efficient Eley-Ridel pathway (fast NH_3-SCR). Gholami and Luo[8] examined Cu–Ce catalysts supported on MWCNTs for NO reduction by CO in the presence of O_2. They achieved 96% NO_x conversion at 220 °C, attributing this high activity to the CNT support facilitating the synergetic interaction between surface oxygen vacancies (SOV) and Cu^+ species. The CNT materials offered better dispersion and stability compared to activated carbon supports. Table 12 summarizes the multifunctional roles of CNTs in air purification catalysis, highlighting how their electronic conductivity, structural features, defect engineering, and surface chemistry synergistically enhance redox activity, pollutant adsorption, and low-temperature catalytic performance.

5.2 Treatment of emerging contaminants in wastewater

CNTs function as adsorption substrates, electron reservoirs, co-catalysts, and chemical reaction modulators.[175] Photocatalysis is an effective method for eliminating persistent and hazardous pollutants from industrial wastewater and domestic sewage, such as pharmaceuticals and various organic dyes.[158,163,170] CNTs are used extensively as effective co-catalysts in the photocatalytic degradation of emerging contami-

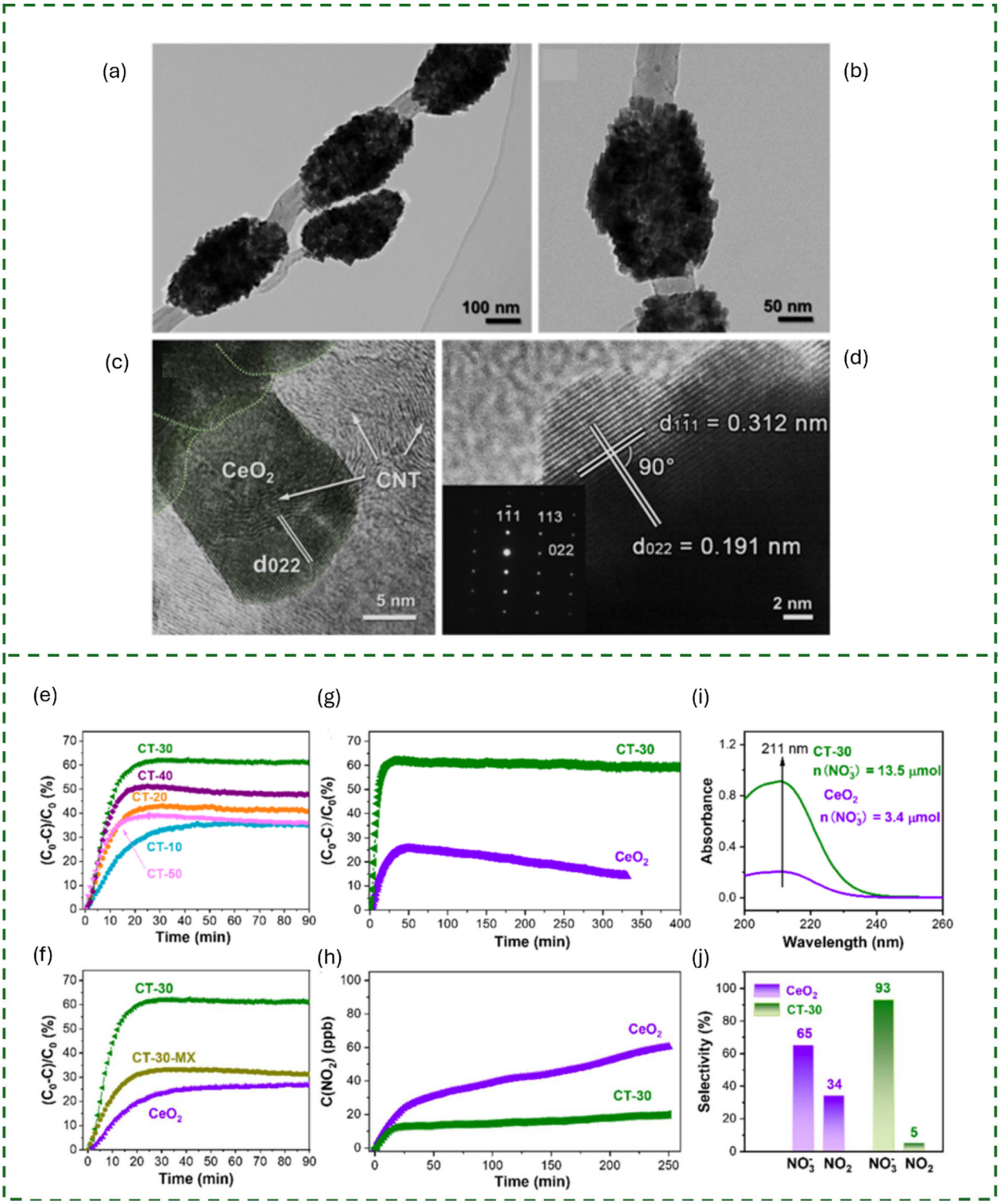

Fig. 13 (a, b) TEM images and (c, d) HRTEM images of CT-30 (the SAED pattern in the inset). Photocatalytic NO oxidation performance of (e) CT-series samples with different CNT contents and (f) CeO_2, CT-30, and CT-30-MX, (g) long-term stability test and (h) concentration profiles of NO_2 during the photocatalytic NO oxidation applying CeO_2 and CT-30 as catalysts, (i) liquid UV–vis spectra of the catalyst-washed solution after photocatalytic reaction for 250 min, and (j) selectivity of NO_3^- and NO_2 for NO oxidation reactions.[173] Figures a–j reprinted from ref. 173 *ACS Appl. Nano Mater.*, 2022, **5**, 3581–3590, with permission from the American Chemical Society, copyright 2026.

Table 12 Multifunctional role and mechanistic contributions of CNTs in photocatalytic air purification

CNT role and property	Mechanistic contribution in air purification catalysis
Electronic conductor and charge-transfer medium	CNTs act as efficient electron sinks and transport pathways, capturing photo- or reaction-induced electrons and suppressing electron–hole recombination in semiconductors (*e.g.*, TiO_2). CNT incorporation enhances electrical conductivity, enabling improved redox kinetics and even electrocatalytic activity under dark or low-energy conditions
Support for redox cycling and metal stabilization	Strong metal–CNT interactions promote dynamic redox cycling and stabilize catalytically active species. CNTs shift redox equilibria (*e.g.*, Cu^{2+}/Cu^{+}, Fe^{3+}/Fe^{2+}) and facilitate *in situ* reduction of metal oxides, increasing the population of low-valent, highly active sites while suppressing metal sintering
Nanostructured and porous framework	CNT networks provide high surface area, mechanical strength, thermal stability, and hydrophobicity. Their mesoporous architecture enhances gas diffusion, pollutant adsorption, and reactant accessibility, thereby improving reaction rates for VOC oxidation and NO_x abatement
Promoter of oxygen vacancy and Ce^{3+}specie formation	CNT integration induces lattice distortion and electronic coupling in metal oxides (notably CeO_2), increasing surface oxygen vacancies (OVs) and Ce^{3+} concentration. These defects enhance oxygen adsorption, activation, and mobility, while surface hydroxyl (OH) species act as reactive oxygen sources during low-temperature oxidation
Catalytic reducing agent	Under oxygen-deficient conditions, CNTs can function as stoichiometric reducing agents, supplying electrons for NO and NO_2 reduction. This role mitigates noble-metal poisoning by surface oxygen and prolongs catalytic activity in exhaust-like environments
Surface doping and functionalization (N-doping)	Nitrogen doping introduces defects and alters the electronic structure of CNTs, generating strong anchoring sites for metals and enhancing surface acidity and reducibility. N-CNTs promote NH_3 adsorption and accelerate the "fast-SCR" pathway, improving NO_x conversion efficiency at low temperatures

nants such as antibiotics (*e.g.*, ciprofloxacin, tetracycline, sulfamethoxazole, cefixime, penicillin, and amoxicillin) and PFAS, which includes perfluorooctanoic acid (PFOA), perfluorooctanesulfonic acid (PFOS), perfluorononanoic acid (PFNA), perfluorodecanoic acid (PFDA), *etc*. CNTs facilitate the initial concentration of pollutants, which enhances reaction kinetics. Naderi *et al.*[176] highlighted that the hybrid CNT@$CoFe_2O_4$/PDS system successfully integrates both the[177] adsorption and catalytic oxidation advantages for efficient tetracycline (TC) degradation. The nanoscale interface of CNTs also enhances mass transfer, providing easy access for oxidants such as ozone to the active sites on the material surface. CNTs function as effective electron mediators, vital for charge separation in photocatalysis and for promoting redox cycles in electrocatalytic systems.[175,178,179]

Recent studies have successfully integrated CNTs into a spectrum of advanced oxidation processes (AOPs), with catalytic enhancement observed across the photocatalytic domain. Takenaka *et al.*[180] successfully synthesized TiO_2 nanoparticles uniformly coating acid-treated CNTs, demonstrating that the resultant photocatalyst showed higher catalytic activity for the photodegradation of organic molecules than pure TiO_2. This enhancement was achieved because the addition of CNTs retarded the recombination of the photogenerated e^-/h^+ pairs in the TiO_2. In a further refinement, the author found that inserting Pt metal particles into the cavities of TiO_2-coated CNTs further improved the photocatalytic activity. This system leverages CNTs to transfer photogenerated electrons from TiO_2 to Pt, thereby maximizing charge separation and efficiency. Zuo *et al.*[178] constructed a ternary Ag–AgBr/$Bi_2O_2CO_3$/CNT Z-scheme heterojunction using CNTs as efficient electronic mediators, achieving 100% degradation of tetracycline (TC) in 40 minutes under visible-light irradiation. The CNTs enhanced light absorption, reduced recombination, and facilitated electron transfer through the constructed Z-scheme pathway. Jia *et al.*[181] synthesized magnetic γ-Fe_2O_3/ZnO@CNT heterojunction catalysts, achieving a 93.5% aniline removal rate *via* photocatalytic coupling with catalytic ozonation (PCO). CNTs boosted electron-migration efficiency, thereby accelerating both the catalytic O_3 and Fenton reactions within the system.

In semiconductor heterojunctions, CNTs utilize their high electrical conductivity to transfer photogenerated electrons, thus acting as an electron reservoir or bridge that suppresses recombination of electron–hole (e^-/h^+) pairs.[178,180] A study by Zhang *et al.*[175] demonstrated that CNTs act as metal-free catalysts in accelerating the transformation of ozone (O_3) into highly potent hydroxyl radicals (HO*) in catalytic ozonation. CNTs alone are also capable of directly activating peroxydisulfate (PDS) or peroxymonosulfate (PMS).[176,182] Zhang *et al.*[175] probed the catalytic ozonation efficiency of MWCNTs and found that OH* accumulated within a tight solid–liquid interphase defined as the HO* zone. The radical abundance in this zone was at least 1000 times higher than in the aqueous bulk phase. Shu *et al.*[183] demonstrated that Co_3O_4 nanoparticles confined in CNT nanochannels (Co_3O_4@CNT) performed exceptionally well as a cathode material for EF degradation of BPA, achieving complete removal in 60 minutes. The catalyst benefited from low electron transfer resistivity and a highly efficient Co^{2+}/Co^{3+} redox cycle that promoted the continuous generation of HO* radicals.

A novel magnetic nanocatalyst, $ZnCoFe_3O_4$@Methylcellulose (MC)/MWCNT/WO_3 was synthesized by Rahimi *et al.*[170] and demonstrated a cefixime removal efficiency of 87% for synthetic samples and 55% for real wastewater samples under optimal conditions. The process followed pseudo-first-order kinetics, with superoxide radicals playing a significant role. The inclusion of MWCNTs increased adsorption capacity, electron transfer, and suppression of charge recombination. Walczak *et al.*[171] proposed a SWCNT–TiO_2/SiO_2 (Fig. 14a) nanocomposite for the photocatalytic oxidation of a mixture of common pharmaceuticals, including ibuprofen, metoprolol, carbamazepine, and oseltamivir under visible light. SWCNT doping, particularly between 1.7 and 3.5 wt%, significantly reduced the band gap to 2.84 eV for S20 (20%mol. SWCNTs), thereby enhancing visible-light

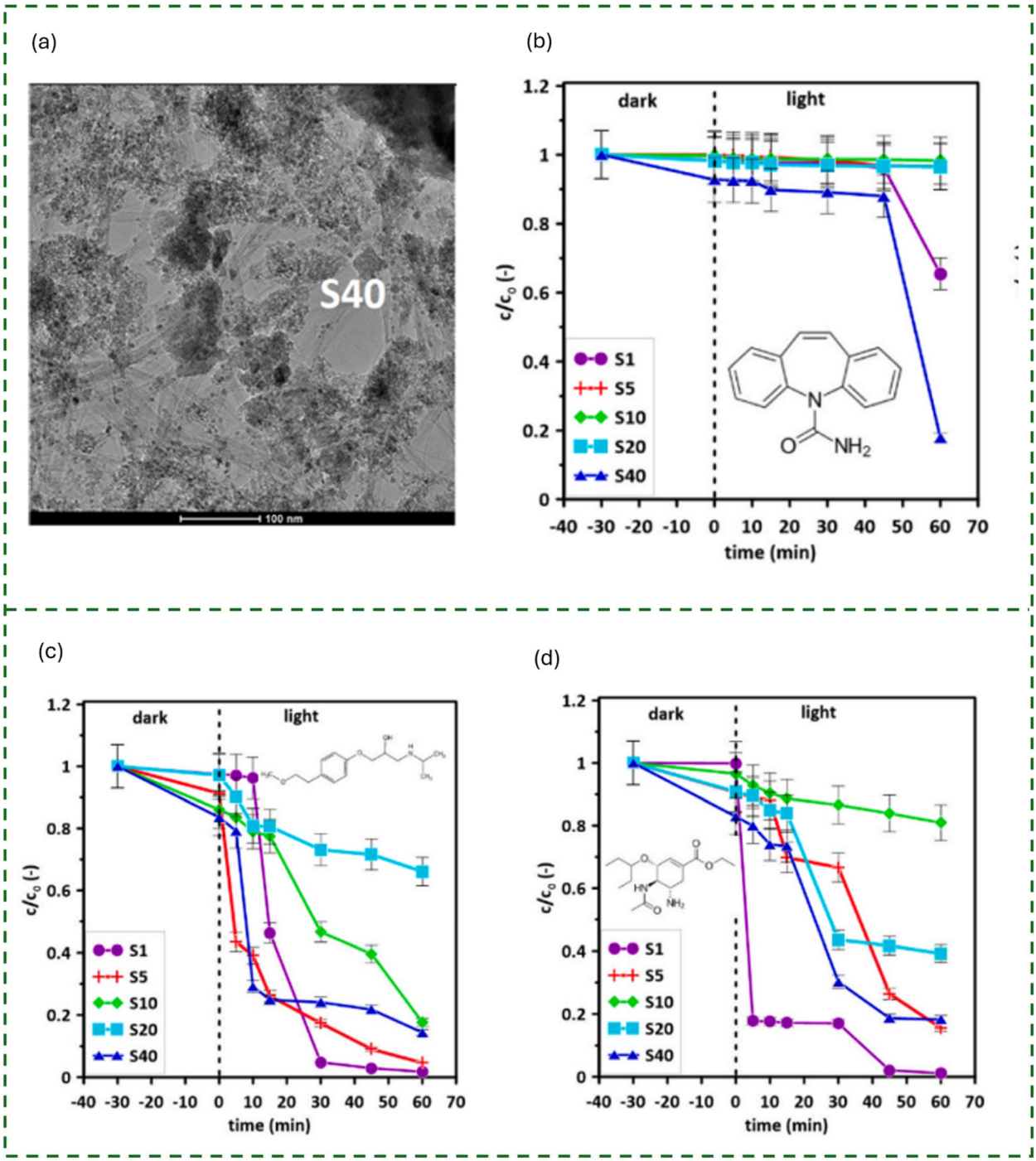

Fig. 14 (a) Surface characteristics of SWCNT–TiO_2/SiO_2 nanocomposites. Kinetics of PPCPs (pharmaceutical and personal care products) photocatalytic removal: (b) IBU (ibuprofen), (c) MET (metoprolol), and (d) OSA (oseltamivir).[171] Figures a–d reprinted from ref. 171 *J. Photochem. Photobiol., A*, 2025, **467**, 116437, with permission from Elsevier, copyright 2026.

activity. The enhanced surface area, porosity, and functional groups of the material also promote the adsorption of these pollutants. According to the study, oseltamivir and metoprolol showed high removal rate constants (0.0626 min^{-1} and 0.0783 min^{-1}, respectively) (Fig. 14b–d).

PTCDA-modified CNTs showed 93% removal of bisphenol A (BPA) within 20 min in a PMS/Vis system, outperforming several other catalysts.[184] This metal-free catalyst activates PMS to generate multiple ROS, including sulfate radicals (SO_4^{*-}), hydroxyl radicals (*OH), singlet oxygen ($^1O_2$), electron holes (h^+), and superoxide ion radicals (O_2^{*-}).[184] Gao *et al.*[185] explored the use of a Mn/Ce-CNT composite for the activation and degradation of sulfamethoxazole in PMS, achieving over 90% degradation within 30 min with excellent stability and

recyclability. Similarly, Nejadramezan *et al.*[158] demonstrated that the CN/Zn/CNT nanocomposite exhibits high photodegradation activity, achieving 93% degradation of methylene blue and 25% degradation of methyl orange under visible light, due to efficient charge transfer and the presence of CNTs as electron-transfer accelerators.

A novel STO/MWCNT composite achieved 84.61% degradation of methylene blue within 120 min under visible light, with hydroxyl radical ions playing a dominant role.[186] A study by Aygun *et al.*[187] showed that TiO_2@f-MWCNTs (functionalized MWCNTs as support for TiO_2 nanoparticles) exhibited photodegradation efficiencies of 76.19% for MB, 78.17% for methylene red, and 57.93% for methyl orange under sunlight. The presence of f-MWCNTs facilitated charge-carrier separation and improved dye removal. In a separate study, Hatel *et al.*[163] observed that the graphene oxide, MWCNT, and tungsten trioxide GO/MWCNT/WO_3 nanocomposite exhibits an 85% degradation rate of Rhodamine B in 240 min under visible light, significantly outperforming GO alone (10%). This improvement is attributed to the light absorption of WO_3 and MWCNTs, which provide more active sites, surface area, improved charge transport, and promote charge-carrier separation. Similarly, the NiO/MWCNT/GO composite synthesized by Subramanyam *et al.*[188] exhibited excellent photocatalytic performance, achieving 92.7% degradation of Reactive Red 35 under UV irradiation in 80 min. The authors observed that the high efficiency is due to interfacial charge transfer between MWCNT and GO, which effectively decreases electron–hole recombination. Table 13 summarizes studies detailing the CNT-based catalysts and their primary mechanistic roles in degrading specific emerging contaminants *via* photocatalytic and electrocatalytic pathways.

5.3 Food safety

CNTs are widely used as a multifunctional platform to enhance food safety and quality assurance, primarily through their strong antimicrobial properties and their capability to improve the performance of polymer matrices. These functionalities directly contribute to pathogen control, prolonged shelf life, and robustness in complex food systems. Particularly, the unique cylindrical, needle-like structure of CNTs allows them to physically pierce and disrupt microbial cell membranes upon direct contact.[198,199] This physical damage often leads to the leakage of intracellular components such as plasmid DNA and RNA and eventual cell death.[198,200] Beyond physical disruption, CNTs induce oxidative stress in pathogens through the generation of reactive oxygen species (ROS), which inactivates a wide spectrum of foodborne bacteria, including *E. coli*, *S. aureaus*, and *Salmonella.*[198,201,202] Also, CNTs create a tortuous path for gas molecules, which significantly reduces the permeability of water vapor, O_2, and CO_2.[201,203] This limitation of gas exchange is vital for delaying the ripening of climacteric fruits and preventing the oxidative rancidity of meat products.[204] CNTs can act as carriers for volatile antimicrobial agents (*e.g.*, allyl isothiocyanate) due to their mesoporous structure, and facilitate a sustained and controlled release that extends the shelf life of perishable items such as chicken and beef for 40 days or longer.[204,205]

Tsou *et al.*[206] investigated hybrid nanocomposite films based on modified poly(butylene succinate) (MPBS) reinforced with ZnO nanoplate-decorated CNTs (MPBS/CNT-ZNP). This low-content hybrid system (0.1 g hg^{-1}) demonstrated superior preservation efficacy for perishable foods. Specifically, MPBS/CNT-ZNP films preserved bananas for more than 14 days, minimizing weight loss and delaying ripening indicators, including accumulation of total soluble solids (TSS) and changes in pH. Furthermore, when packaging raw chicken, the film significantly curtailed bacterial proliferation, extending the microbiological shelf life to at least 108 hours under refrigeration by keeping bacterial counts below the common spoilage threshold. The CNT-ZNP composite showed a highly significant reduction in *E. coli* counts ($P \leq 0.001$). Similarly, Ge *et al.*[205] studied poly(butylene succinate) (PBS) nanocomposites featuring ZnO-coated MWCNTs (PBS/MWCNT-ZnO), noting that the combination enhanced tensile properties and conductivity, as well as imparted antibacterial properties. Optimal loading (0.1 parts per hundred (pph)) boosted tensile strength by 22% and elongation at break by 95.7% compared to pure PBS. The composite exhibited excellent antibacterial activity against *E. coli*, with sterilization efficacy surpassing 98% at 0.4 pph. When used for beef packaging, the film effectively extended meat freshness and slowed bacterial growth over 72 hours.

Yakdoumi *et al.*[203] produced polylactic acid (PLA) nanocomposite films reinforced by MWCNTs modified with polydopamine (PDA) or TiO_2-modified (PLA/MWCNTs/TiO_2-PDA). The PLA/TiO_2-PDA-MWCNTs nanocomposite exhibited strong antimicrobial and antifungal activity compared to pure PLA, while also achieving substantial mechanical enhancements (161% increase in Young's modulus and 815% increase in hardness). This functionalized hybrid system suggests utility for energy storage and food packaging applications. Also, Ibrahim *et al.*[207] prepared films for food packaging applications utilizing chitosan-polyethylene oxide (Ch.-PEO) blends doped with (GO) and MWCNTs (Chitosan-PEO/MWCNTs/GO). The resulting MWCNTs/GO/Ch.-PEO nanocomposites showed a broad antimicrobial activity against tested microbes, including Gram-positive bacteria (*Staphylococcus aureus* was the most sensitive) and fungi (*Penicillium roqueforti* was the least sensitive). Furthermore, Dias *et al.*[204] fabricated cellulose-based films incorporated with the volatile antimicrobial agent allyl isothiocyanate (AIT) and CNTs (Cellulose/CNT/AIT). This system showcased the role of CNTs as a nano-reactor or encapsulating agent to retain the highly volatile AIT, which then diffused from the film into shredded cooked chicken meat inoculated with *Salmonella Choleraesuis*. The migration of AIT-controlled oxidation and reduced microbial contamination was effective for 40 days of storage. Sivakumar and Hema[201] developed functionalized CNTs by coating MWCNTs with phytocompounds from *Centella asiatica via* physical absorption. This resulting composite significantly enhanced the antimicrobial activity of MWCNTs against food-spoiling pathogens

Table 13 Multifunctional roles of CNT-based catalysts for the degradation of emerging contaminants

Contaminant(s)	Process	Nanomaterial	Mechanistic role of CNTs	Key finding	Ref.
Tetracycline (TC)	Z-scheme photocatalysis	CNT embedded in Ag–AgBr/$Bi_2O_2CO_3$ heterojunction	Acts as an electronic mediator and electron reservoir; promotes interfacial charge separation and suppresses e^-/h^+ recombination	Enhanced visible-light photocatalytic degradation	178
Tetracycline (TC)	Visible-light photocatalysis	MWCNT coupled with plasmonic Bi–BiOBr	Provides conductive channels for rapid electron transport and functions as adsorption sites *via* π–π stacking	Accelerated charge transfer and improved TC adsorption	189
Ibuprofen (IBP)	PMS (peroxymonosulfate) activation (catalytic membrane)	N-doped CNT encapsulating magnetic Ni–Co alloy (NiCo@NCNT)	Acts as an electron-transfer mediator, stabilizes active alloy NPs, and enables radical and nonradical pathways	High catalytic stability and efficient IBP degradation	190
Sulfamethoxazole (SMX)	PMS activation	CNT-encapsulated $CoFe_2O_4$ spinel (closed structure)	Provides nanoconfinement-enhanced electron transfer and favors the singlet oxygen ($^1O_2$) non-radical pathway	Selective and efficient SMX removal	191
Sulfamerazine (SMZ)	PMS activation (single-atom catalysis)	CNT-supported atomically dispersed Co–N_5 sites	Drives degradation primarily through a non-radical electron-transfer pathway by Co–N_5 coordination	Superior activity with maximized metal utilization	192
Bisphenol A (BPA)	Electro-Fenton	Co_3O_4 nanoparticles confined in CNT nanochannels	Facilitates Co^{2+}/Co^{3+} redox cycling, lowers electron-transfer resistance, and enhances H_2O_2 activation	Intensified $^{\bullet}OH$ generation and BPA degradation	183
Phenanthrene (PHE)	Ferrate (Fe(VI)) activation	Fe_2O_3-loaded CNT with surface C–OH defects	Acts as an electron-transfer mediator between PHE and Fe(VI); promotes high-valent Fe(IV/V) reactivity and $^1O_2$ formation	Boosted oxidative capacity toward PHE	193
Perfluorooctane sulfonate (PFOS)	Catalytic ozonation	Highly graphitic MWCNT (metal-free)	Intrinsic catalytic sites accelerate O_3 decomposition; formation of interfacial $^{\bullet}OH^-$ rich zone	Efficient PFOS degradation without metal catalysts	175
Phenol/phenolic compounds	PDS activation	CNTs with tunable oxygen content and graphitization (QSAR-based study)	Nonradical direct electron transfer *via* CNT-PDS* complex, governed by conductivity and hydrophobicity	Predictive structure–activity relationships	194
4-Chlorophenol (4-CP)	PMS activation	Defective, oxygen-functionalized MWCNTs (optimized C═O groups)	Acts as a metal-free catalyst, with carbonyl groups as active sites for generating surface-bound radicals; enhanced surface conductivity	High PMS activation efficiency	177
Phenol/4-bromophenol (4-BP)	Periodate (PI) activation	Calcined CNTs with residual metal species	Residual Fe/Co/Ni act as catalytic sites; electron donation enables IO_3* generation	Dominant single-electron transfer pathway	195
Metronidazole (MNZ)	Thermal/PMS-M (membrane reactor)	CNT-based filter membrane	Enhances mass transfer and radical exposure; promotes SO_4^{*-} and *OH pathways	Substantially increased degradation rate	196
Congo Red (CR)/Cr (VI)	Photocatalysis	Carboxylated CNTs bridged with CdSe and CeO_2	Accelerates charge transfer (CdSe → CNT → CeO_2) and suppresses charge recombination; boosts adsorption	Simultaneous dye degradation and Cr (VI) reduction	197

such as *Salmonella typhi*, *Escherichia coli*, and *Pseudomonas aeruginosa*.

Structurally, SWCNTs are often considered more cytotoxic against bacteria than MWCNTs due to their smaller diameter, which allows them to penetrate the bacterial cell wall and membrane more effectively.[198,208] The sharp edges of CNTs can physically disrupt the bacterial cell membrane upon contact, causing severe cell damage and nucleic acid leakage.[198,199] CNTs are often more effective in hybrid systems, where they serve as platforms for metal oxides. These composites rely on a synergistic antimicrobial mechanism.[205,206] ZnO nanoparticles are key, primarily functioning by generating ROS that cause oxidative stress and disrupt cell structures.[205] Additionally, the release of zinc ions (Zn^{2+}) penetrates and inactivates bacteria.[206] The combination with CNTs enhances this catalytic pathway, leading to improved antibacterial performance compared to components alone.[203,205] CNTs exploit their hollow structure and large specific surface area to act as carriers or nano-reactors.[200] This enables the controlled release of encapsulated antimicrobial compounds (*e.g.*, AIT or cinnamaldehyde) over extended periods, thereby improving detection speed (by preventing microbial growth in the first place) and lowering the effective concentration (LOD) needed compared to administering the agents directly.[204] The mechanical and barrier-enhancing properties of CNTs directly contribute to robustness against matrix interference in complex food systems. For instance, the uniform dispersion of CNT-ZNP at optimal concentrations (*e.g.*, 0.1 g hg^{-1}) within the

polymer matrix created a tightly structured film.[206] This dense structure notably reduced water vapor permeability by forcing water molecules to follow a tortuous, zigzag diffusion path around the filler, thereby effectively maintaining the freshness and integrity of high-moisture foods such as chicken and bananas.[206]

5.3.1 CNT-based sensors for food safety. The excellent electrical conductivity and high surface area of CNTs make them ideal components for developing highly sensitive and reliable biosensors.[209,210] These properties further enable CNTs to serve as active elements, amplifying detection signals and providing numerous binding sites for bioreceptors.[209] For instance, the CNT surface acts as a scaffold for the high dispersion of sensing components, such as metal nanoparticles (*e.g.*, Pt, Ag, Pd) or biomolecules (enzymes, aptamers, DNA), ensuring efficient detection even at low contaminant concentrations.[54,174] Their electrical conductivity arising from a highly ordered sp^2-carbon network is critical for signal transduction in sensors.[207,211] Also, CNTs facilitate rapid charge-transfer reactions between target species and the electrode surface in electrocatalytic-based sensors.[97,200] Consequently, CNT-based nanocomposites and devices have shown promise in addressing critical public health concerns, particularly for the rapid and accurate detection of a wide array of food contaminants, including chemical adulterants, pesticides, pathogenic bacteria, and allergens.[212,213] For instance, CuO–CNT nanocomposites have been developed for the non-enzymatic electrochemical detection of melamine in dairy products, exhibiting a very low limit of detection and a rapid response time of 10 seconds due to the conductivity of CNTs and their large surface area, which facilitates electrochemical oxidation of melamine.[212]

The widespread adoption of CNT-based sensors in food safety is driven by their inherent advantages over conventional analytical methods. They offer remarkably high sensitivity, rapid response times, and excellent specificity, crucial for detecting trace levels of contaminants and pathogens in complex food matrices.[210,213] These sensors are often label-free, portable, and cost-effective, making them suitable for on-site, real-time monitoring, addressing limitations such as complicated procedures, high costs, and lengthy analysis times associated with traditional techniques like HPLC or ELISA.[214–216] Furthermore, advancements in CNT fabrication and passivation techniques, coupled with sophisticated bioreceptor immobilization strategies (*e.g.*, aptamer groups), enhance the reproducibility, stability, and anti-interference capabilities of these biosensors, as demonstrated by 100% accuracy in single-blind tests and long-term stability.[214,217]

In food pathogen inactivation, photocatalysis is an effective approach for disinfection and microbial control by generating reactive species that damage microbial cells, thus enhancing food safety. The $ZnCoFe_2O_4$@MC/MWCNT/WO_3 nanocomposite demonstrated strong antibacterial properties against both Gram-positive bacterium *Bacillus cereus* and Gram-negative bacterium Acinetobacter baumannii. The smaller particle size (15 nm) of the nanocomposite facilitates passage through cell membranes, and the production of ROS contributes to cell destruction.[170] An innovative composite material comprising hydroxyapatite (Hap) reinforced with MWCNTs and doped with silver nanoparticles (AgNPs) and silver core Ag@SeNPs was synthesized by Unal[218] and evaluated for its antimicrobial activities against various microorganisms, including *P. aeruginosa*, *E. coli*, *S. aureusi E. faecalis*, and *C. albicans*. Ag@Se-MWCNTs/Hap exhibited superior efficacy

Table 14 Application of various CNT-based sensors for food safety

Nanomaterial	Application	Activity	Stability	Ref.
CuO–CNT nanocomposite	Non-enzymatic electrochemical detection of melamine in dairy products	LOD = 0.27 nM; linear range 0.05–0.5 nM; sensitivity = 93.924 μA μM^{-1} m^{-2}; response time = 10 s	Reliable in real milk analysis without interference	212
Co,N-HPNC@CNT	Electrochemical sensing of organophosphorus pesticide (chlorpyrifos) in fruit samples	LOD = 0.03 pmol L^{-1}; linear range 0.1 pmol L^{-1}–10 μmol L^{-1}; high sensitivity at +0.2 V	Retained >95% current after 14 days	213
Zein–CNT (Z-CNT) nanocomposite	Electrochemical detection of gliadin in wheat-based foods (celiac disease relevance)	LOD = 0.5 ppm; linear range 0.5–100 ppm; R^2 = 0.996	Stable for 30 days; reproducible over 4 weeks	216
CNT network + Y_2O_3 + AuNP + aptamers	FET biosensor for dual detection of *E. coli* O157 and Listeria monocytogenes	LOD = 1 CFU for both pathogens; rapid (<200 s); linear range 80–5 × 10^5 CFU mL^{-1}	Stable, repeatable; 100% accuracy in blind food sample tests	217
ZnS@CNT hybrid	Electrochemical detection of *E. coli* O157:H7	LOD ≈ 10^3 CFU mL^{-1}; linear range 10^3–10^8 CFU mL^{-1}; 30 min incubation	Robust biosensor performance; good stability	209
CNT/AuNP on PVDF membrane	SERS sensing of contaminants (melamine, paraquat, malachite green)	EF = 2.4 × 10^6; LOD = 1 nM melamine, pM-level MG detection	High stability in water, acid, alkali, oxidant, UV; reproducible (RSD 9.4–15.8%)	215
Lipase–CNT on optical fiber SPR sensor	Detection of tributyrin in food	Sensitivity = 4.45 nm mM^{-1}; LOD = 0.34 mM; RI sensitivity = 2077 nm RIU^{-1} response time = 9 min	Stable (SD = 0.51 nm over 45 min); repeatable (Cv = 7.5%)	210
CNT FET biosensor with Y_2O_3 + AuNP + aptamers	On-site detection of aflatoxin B1 (AFB1) in corn & peanuts	LOD = 0.55 fg mL^{-1} (standard), 0.25 pg kg^{-1} (corn); response <60 s	Stable, reproducible; SD = 0.02 for standard/corn; 85% response retained after 5 days	214

with inhibition zones of 18 mm, 12 mm, and 20 mm for *S. aureus*, *E. faecalis*, and *Candida albicans*, respectively. The incorporation of Ag@SeNPs enhanced Hap's antibacterial and antifungal properties through a synergistic mechanism. The activity and stability of CNT-based sensors for food safety are presented in Table 14.

6. Conclusions

CNTs play a transformative role, acting as highly effective multifunctional catalytic platforms rather than mere passive supports. Their exceptional performance stems from a cohesive set of nanoscale principles: carefully managed defect chemistry, tunable electronic structure modulation (often *via* heteroatom doping), strong geometric constraints imposed by nanoconfinement, and robust interfacial interactions with catalytic phases. These characteristics significantly enhance the reaction kinetics, selectivity, and durability of CNTs for energy and environmental remediation applications.

6.1 Observations

1. The catalytic role of CNTs in energy production has evolved from that of a passive conductive support to that of an active catalytic center, driven primarily by dimensional confinement and deliberate modulation of electronic transfer. Distinct CNT architectures impact intrinsic catalytic functionality. For instance, SWCNT bundles form confined groove sites that markedly enhance O_2 adsorption and activation for the ORR, while triple-walled CNTs promote electron-tunneling pathways that accelerate charge-transfer kinetics and maximize alcohol oxidation activity. These structure–property relationships further govern catalytic selectivity and durability. Confinement within SWCNTs can also direct single-atom Pt activity preferentially toward the HOR while suppressing ORR, whereas highly graphitic, defect-lean MWCNTs exhibit superior resistance to carbon corrosion, a critical requirement for long-term operation in fuel cell and water-splitting systems.

2. In FTS, CNTs function as versatile nano-confinement supports whose tunable surface chemistry is leveraged to regulate key FTS catalytic phenomena. Chemical modifications such as acid treatment, defect creation, or N-doping create specific anchoring sites that stabilize metal nanoparticles against sintering, thereby regulating metal dispersion. For iron catalysts, the intrinsic electronic effects of the support (*e.g.*, the electron-donating effect of nitrogen) directly modulate the metal–support interaction, promoting both the reduction of iron oxides and subsequent desirable carburization behavior toward active iron carbides such as e-Fe_2C. Specifically, the nanoscale confinement effect provided by the CNT inner channels physically restricts particle mobility and enhances the residence time of CH_x intermediates, thereby promoting successive coupling steps and increasing the probability of chain growth toward long-chain hydrocarbons (C_{5+} and wax), while concurrently suppressing undesired methane formation.

3. In alcohol and glycerol steam reforming reactions, CNTs serve as multifunctional structural scaffolds and energy transducers. Their high electrical conductivity enables rapid, efficient self-heating (Joule heating) processes that minimize thermal side reactions and optimize product distribution at lower temperatures. The CNT surface also promotes the adsorption and spillover of activated H-adspecies (especially on high-crystallinity h-type CNTs), ensuring high H_2 selectivity by favoring the steam reforming pathway over decomposition reactions. CNTs also act as powerful synergistic co-catalysts by enhancing metal dispersion and facilitating electron transfer characteristic of hydrogen spillover from the metallic phase (Cu, Pd) to the support surface, which is crucial for accelerating dehydrogenation steps and improving catalyst stability. Furthermore, the nanochannels in CNTs minimize the accumulation of graphitic coke and simultaneously tune the resulting active sites to exhibit weaker hydrogen adsorption strength, a property that correlates with superior intrinsic catalytic activity and higher glycerol conversion rates at low operating temperatures.

4. CNTs act as powerful, chemically tunable co-catalysts that actively modulate the redox chemistry, electron density, and acid sites concentration of coupled metal or metal oxide systems in VOC and NOx degradation. The integration enhances reducibility and stabilizes important intermediate valence states, shifting the redox equilibrium and significantly accelerating both the Eley–Rideal mechanism and the "fast SCR" pathway needed for highly efficient, low-temperature NOx conversion. In photoremediation, CNTs serve as a three-dimensional conductive network and efficient electron acceptor, forming synergistic heterojunctions with semiconductors (TiO_2). This electronic hybridization suppresses photo-induced electron hole species (h^+), enabling the deep oxidation pathway of pollutants and minimizing the formation of undesirable toxic byproducts.

5. In antimicrobial contaminant degradation, pristine or functionalized CNTs serve as enzyme-free active materials primarily through physical and mechanical membrane piercing, leveraging their high aspect ratio and sharp edges to mechanically disrupt and destroy bacterial cells directly. Furthermore, when employed as synergistic co-catalyst systems, CNTs enhance degradation efficiency by serving as nanoscale platforms that enhance the localized generation of reactive oxygen species and the controlled release of antimicrobial metal ions, enabling robust, broad-spectrum microbial control in food matrices. Alternatively, CNTs utilize their hollow interiors as nanoreactors, encapsulating highly volatile agents (*e.g.*, allyl isothiocyanate) and regulating their slow, sustained diffusion to inhibit contamination and reduce chemical degradation during prolonged storage.

6. For sensing applications, functionalized CNTs serve as catalytic signal amplifiers and enzyme-free active electrode materials by increasing the dielectric constant and electrical conductivity of the material, thereby facilitating enhanced electron transfer kinetics across the complex matrix/analyte interface. The purposeful incorporation of CNT functional groups

creates strong surface charges and double-bonding properties that significantly enhance the oxidation of organic contaminants, thereby boosting the anodic peak current of compounds such as bisphenol F and enabling ultra-sensitive and rapid electroanalytical methods.

6.2 Perspectives

The field is undergoing a crucial transition from reliance on empirical CNT utilization to more rational catalyst design, leveraging quantitative structure–function relationships and advanced mechanistic insights to guide the strategic synthesis of materials. The performance of CNT-based catalysts consistently arises from intentional structural and interfacial control, rather than empirical material selection. Key design principles include:

1. Defect and heteroatom engineering, which activates the CNT surface, creates anchoring sites for metal species, and modulates local electronic structure to steer reaction selectivity.

2. Controlled metal–CNT interfacial chemistry, where charge transfer and bonding strength dictate reducibility, durability, and adsorption energetics of key intermediates.

3. Nano-confinement and hierarchical architectures, which suppress nanoparticle sintering, regulate reaction probability, and enable coupled ion–electron transport in both thermochemical and electrochemical systems.

Together, these strategies establish CNTs as customizable catalytic platforms capable of achieving high atom efficiency and reaction specificity.

Despite rapid progress, several fundamental challenges remain. The precise nature of active sites, particularly in heteroatom-doped and single-atom CNT systems, remains difficult to resolve due to overlapping chemical functionalities and dynamic structural evolution under operating conditions. Long-term durability under realistic industrial environments, including resistance to coking, gasification, poisoning, and metal sintering, remains insufficiently validated. Additionally, the absence of quantitative structure–activity relationships limits predictive catalyst design, as key parameters such as defect density, heteroatom distribution, and confinement degree remain tightly coupled and difficult to control independently.

Advancing CNT-based catalysis will require integrated, interdisciplinary strategies. *In situ* and operando characterization techniques are essential for capturing real-time active-site evolution and reaction mechanisms. Computational–experimental coupling must be leveraged to guide rational catalyst design by linking electronic structure to reaction energetics. From a translational perspective, the development of scalable, sustainable synthesis routes, including modified CVD and biomass-derived CNT architectures, will be critical. Finally, standardized benchmarking protocols, particularly for long-term stability and safety, are necessary to enable meaningful comparison across studies and accelerate technological adoption. While CNT-based catalysts are not yet widely commercialized, multiple developments indicate meaningful progress toward technology translation. For Fischer–Tropsch synthesis, CNT-supported Co catalysts have been evaluated in long-duration fixed-bed reactor studies (500 hours), demonstrating stability and regenerability under conditions relevant to industrial operation.[118] Also, CNT-supported electrocatalysts (*e.g.*, Pt/CNT, N-doped CNTs) are being integrated into membrane electrode assemblies (MEAs) and have achieved stable performance over extended operation at industrially relevant current densities, suggesting readiness for scaled prototype devices.[219] At the same time, industrial CVD processes now produce CNTs at hundreds of tons per year with high purity, satisfying a key scale-up requirement for catalyst design and supporting broader adoption across various catalytic applications.[220]

The application of CNTs in food safety involves a complex trade-off between their exceptional antimicrobial and structural benefits and their potential human and environmental toxicity, which can trigger oxidative stress and inflammatory responses. To mitigate these risks, surface functionalization with polar groups such as carboxyl and hydroxyl species is essential, as it transforms hydrophobic, inert tubes into hydrophilic structures with improved biocompatibility and reduced cytotoxic potential. Immobilizing CNTs within biodegradable polymer matrices like polyactic acid (PLA) or polybutylene succinate (PBS) further limits their migration into the food chain while leveraging their ability to create a tortuous path that enhances moisture and gas barrier properties. Furthermore, the development of synergistic hybrid systems, such as decorating CNTs with ZnO nanoparticles or natural phytocompounds such as *Cantella asiatica*, allows for significant performance gains in pathogen inhibition at minimal loading levels, thereby reducing overall nanomaterial exposure. Ultimately, achieving safe translation requires rigorous risk assessments and precise nanoscale engineering to stabilize these materials against leaching or structural degradation during their operational lifecycle in the food industry.

Photocatalysis is a promising and effective method for degrading a wide range of pollutants at relatively low concentrations in the gas phase or liquid phase into innocuous compounds. The process is characterized by simple operation, mild reaction conditions, light activation (including sunlight), low cost, and potential for large-scale use. A growing family of emerging contaminants with documented adverse health effects, including per- and polyfluoroalkyl substances (PFAS), pharmaceuticals, herbicides, pesticides, and hormones, is poorly degraded by conventional advanced oxidation processes (AOPs) or standalone treatment technologies. Research efforts should also be directed toward integrating breakthrough photocatalytic technologies, employing novel photocatalysts, with conventional AOP processes to generate higher concentrations of ROS for degrading a broad spectrum of contaminants. This approach has the potential to outperform what current treatment systems alone can reliably remove.

Most studies employing CNT/TiO_2 hybrids for photocatalysis use MWCNTs or mixtures of SWCNT types for coupling, which form Schottky barriers that enhance electron–hole sep-

aration and thus photocatalytic activity. Less common are semiconducting SWCNTs coupled to TiO_2 to form heterojunctions. Improved control over SWCNT structure (chirality and diameter) is required to further investigate the design of this interfacial contact, which shows promise for visible-light activation. In addition, the controlled SWCNT synthesis process should be easily scalable to facilitate the practical application of the technology.

Conflicts of interest

There are no conflicts to declare.

Data availability

No primary research results, software or code have been included and no new data were generated or analysed as part of this review.

References

1 Y.-J. Kim and W.-S. Choi, *Nanomaterials*, 2024, **15**, 22.
2 K. Zhang, X. Liu, L. Tan, K. Xu, W. Pei, F. Tang, T. Wei, J. Jia, B. Xu, J. Li, X. Zhu and F. Ge, *Desalination*, 2025, **600**, 118518.
3 A. Andezai and J. O. Iroh, *Energies*, 2025, **18**, 1304.
4 J.-W. Lee, J. Kim, M. S. Kim, K.-S. Hong, I. H. S. Yang and H. J. Jeong, *J. Mater. Chem. C*, 2025, **13**, 4576–4582.
5 Y. Ren, Q. Liu and X. Wang, *Adv. Funct. Mater.*, 2025, 2505903, DOI: 10.1002/adfm.202505903.
6 C. Y. Lu, H. H. Tseng, M. Y. Wey, K. H. Chuang and J. H. Kuo, *J. Environ. Manage.*, 2009, **90**, 1884–1892.
7 C.-Y. Lu, M.-Y. Wey and K.-H. Chuang, *Appl. Catal., B*, 2009, **90**, 652–661.
8 Z. Gholami and G. Luo, *Ind. Eng. Chem. Res.*, 2018, **57**, 8871–8883.
9 Q. Ma, D. Wang, M. Wu, T. Zhao, Y. Yoneyama and N. Tsubaki, *Fuel*, 2013, **108**, 430–438.
10 H. Gao, Z. Yao, Y. Shi and S. Wang, *Catal. Sci. Technol.*, 2018, **8**, 697–701.
11 Y. Zhu, K. Chen, C. Yi, S. Mitra and R. Barat, *Chem. Eng. Commun.*, 2018, **205**, 888–896.
12 H. M. Sung, E. J. Kwon, D. Lee, Y. Jung, Y. H. Kim, C.-K. Oh and S. Jeong, *Carbon*, 2025, **237**, 120127.
13 J. Gretz and S. Kruss, *Carbon Trends*, 2025, **19**, 100498.
14 D. Chou, A. Rehman, M. Inc and S. Rezapour, *Multiscale Multidiscip. Model. Exp. Des.*, 2025, **8**, 237.
15 N. Saifuddin, A. Z. Raziah and A. R. Junizah, *J. Chem.*, 2013, **2013**, 676815.
16 N. Saba, M. Jawaid, H. Fouad and O. Y. Alothman, in *Nanocarbon and its Composites*, Elsevier, 2019, pp. 327–354.
17 F. Daneshvar, H. Chen, K. Noh and H.-J. Sue, *Nanoscale Adv.*, 2021, **3**, 942–962.
18 H. M. Dewey, A. Lamb and J. Budhathoki-Uprety, *Nanoscale*, 2024, **16**, 16344–16375.
19 R. Alrammouz, J. Podlecki, P. Abboud, B. Sorli and R. Habchi, *Sens. Actuators, A*, 2018, **284**, 209–231.
20 J. Zou and Q. Zhang, *Adv. Sci.*, 2021, **8**, 2102860.
21 Y. Okano, H. Yamamoto, K. Hoshino, S. Miyake and M. Takashiri, *Materials*, 2025, **18**, 188.
22 S. Ahmad, Y. Liao, A. Hussain, Q. Zhang, E.-X. Ding, H. Jiang and E. I. Kauppinen, *Carbon*, 2019, **149**, 318–327.
23 Q. Wu, X. Chi, X. Yao, G. Xu, X. Zhang, K. Chen, G. Lin and M. He, *Carbon*, 2025, **238**, 120279.
24 A. Przewłoka, A. Rehman, S. Smirnov, E. Karpierz-Marczewska, A. Krajewska, M. Liszewska, P. Dróżdż, K. Pavłov, M. Dub, S. Novytskyi, B. Jankiewicz, Z. Mierczyk, S. Rumyantsev and D. V. Lioubtchenko, *Carbon*, 2023, **202**, 214–220.
25 J. Lee, M. Bak, P. J. Yoo and W.-J. Kim, *Appl. Surf. Sci.*, 2025, **688**, 162440.
26 J. O. Márquez, Master's thesis, Universidad de Cantabria, 2015, DOI: 10.13140/RG.2.1.2187.5680.
27 T. V. Patil, D. K. Patel, S. D. Dutta, K. Ganguly, A. Randhawa and K.-T. Lim, *Appl. Sci.*, 2021, **11**, 9550.
28 A. Abdulhameed, M. M. Halim and I. A. Halin, *Nanotechnology*, 2023, **34**, 242001.
29 F. Alhashmi Alamer and G. A. Almalki, *Polymers*, 2022, **14**, 5376.
30 S. S. Siwal, Q. Zhang, N. Devi and V. K. Thakur, *Polymers*, 2020, **12**, 505.
31 H. Wang, Y. Yuan, L. Wei, K. Goh, D. Yu and Y. Chen, *Carbon*, 2015, **81**, 1–19.
32 L. Yang, W. Ji, M. Mao and J.-n. Huang, *J. Cleaner Prod.*, 2020, **257**, 120408.
33 J. P. Raval, P. Joshi and D. R. Chejara, in *Applications of Nanocomposite Materials in Drug Delivery*, Elsevier, 2018, pp. 203–216.
34 M. R. Predtechenskiy, A. A. Khasin, A. E. Bezrodny, O. F. Bobrenok, D. Y. Dubov, V. E. Muradyan, V. O. Saik and S. N. Smirnov, *Carbon Trends*, 2022, **8**, 100175.
35 R.-I. Vasluianu, A. M. Dima, L. Bobu, A. Murariu, O. Stamatin, E.-R. Baciu and E.-O. Luca, *J. Food Biochem.*, 2025, **16**, 110.
36 K. Hata, *Synthesiology*, 2016, **9**, 167–179.
37 H. Almkhelfe, X. Li, R. Rao and P. B. Amama, *Carbon*, 2017, **116**, 181–190.
38 B. M. Everhart, H. Almkhelfe, X. Li, M. Wales, P. Nikolaev, R. Rao, B. Maruyama and P. B. Amama, *Ind. Eng. Chem. Res.*, 2020, **59**, 9095–9104.
39 H. Almkhelfe, J. Carpena-Núñez, T. C. Back and P. B. Amama, *Nanoscale*, 2016, **8**, 13476–13487.
40 M. Endo, K. Takeuchi, S. Igarashi, K. Kobori, M. Shiraishi and H. W. Kroto, *J. Phys. Chem. Solids*, 1993, **54**, 1841–1848.
41 H. Cheng, F. Li, G. Su, H. Pan, L. He, X. Sun and M. Dresselhaus, *Appl. Phys. Lett.*, 1998, **72**, 3282–3284.
42 P. Nikolaev, M. J. Bronikowski, R. K. Bradley, F. Rohmund, D. T. Colbert, K. A. Smith and R. E. Smalley, *Chem. Phys. Lett.*, 1999, **313**, 91–97.

43 A. Karakassides, H. Inoue, P. Liu, Z. Xu, G. Yasin, H. Jiang and E. I. Kauppinen, *Nanoscale*, 2025, **17**, 12797–12809.
44 H. Yang, Z. Zhang, Z. Wang, F. Zhang, S. Liu, L. Zhang, C. Shi, P. X. Hou, H. M. Cheng, X. Wang and C. Liu, *Adv. Funct. Mater.*, 2025, **35**, 2425156.
45 D. Y. Kim, H. Sugime, K. Hasegawa, T. Osawa and S. Noda, *Carbon*, 2011, **49**, 1972–1979.
46 S. Temizel-Sekeryan, F. Wu and A. L. Hicks, *Int. J. Life Cycle Assess.*, 2021, **26**, 656–672.
47 D. Gardenö, L. Bábanová, V. Mazánek, Z. Sofer, P. Kríž, L. Mrazík, J. Mareš, J. Floreková, J. Schneider, S. Ashtiani, C. Vorndran, M. Thommes and K. Friess, *J. Membr. Sci.*, 2025, **729**, 124156.
48 J. Suni, S. Valkama and E. Peltola, *ACS Omega*, 2025, **10**, 5554–5562.
49 N. Shakir, Expansion Solutions Magazine, 2023, https://www.expansionsolutionsmagazine.com/cnano-technology-usa-selects-kansas-city-region/.
50 J. Ouyang, H. Shin, P. Finnie, J. Ding, Z. Li, B. Mirka and P. R. L. Malenfant, *ACS Appl. Nano Mater.*, 2025, **8**, 8260–8273.
51 Q. Chen, C. Y. Yu, Y. C. Zhai, T. Watanabe, M. Kawasumi, M. Huda and Y. Matsuo, *Small Methods*, 2025, 2500074, DOI: 10.1002/smtd.202500074.
52 P. Wang, C. Wang, Y. Hu, J. Zhu, H. Yang, F. Li, Y. Ye and R. Shen.
53 R. Liu, R. Liu, X. Ma, B. H. Davis and Z. Li, *Fuel*, 2018, **211**, 827–836.
54 Z. Zhang, J. Zhang, X. Wang, R. Si, J. Xu and Y.-F. Han, *J. Catal.*, 2018, **365**, 71–85.
55 Z. S. Doğan, E. E. Doğan, Z. Bicil and B. K. Kizilduman, *Fuel*, 2025, **396**, 135280.
56 H. Yamamoto, T. Amezawa, Y. Okano, K. Hoshino, S. Ochiai, K. Sunaga, S. Miyake and M. Takashiri, *Appl. Phys. Lett.*, 2025, **126**, 063902.
57 M. Shen, T. Inoue, M. Wang, Y. Liu and Y. Kobayashi, *ACS Appl. Mater. Interfaces*, 2025, **17**, 20105–20115.
58 J. A. Ramirez B, D. V. Krasnikov, H. A. Butt, V. A. Dmitrieva, S. I. Serebrennikova, O. R. Trepalin, A. R. Vildanova, V. A. Kondrashov, A. E. Goldt, D. V. Dzhurinskiy, J. A. Baimova, R. Alexander, A. Kaushal, K. Dasgupta, O. Akhavan and A. G. Nasibulin, *Carbon*, 2025, **238**, 120230.
59 H. Tian, Q. Guo, S. Liu, K. Jiao, X. Ren, J. Liu, H. Hao, J. Yin, J. Long, Y. Wang, J. Hu, J. Yang, Y. Cheng, X. Gao and J. Zhang, *ACS Nano*, 2025, **19**, 21729–21738.
60 H. Zhang, X. Chen, S. Xu, Y. Luo, X. Dai, Q. Liu and X. Zhou, *Appl. Mater. Today*, 2025, **44**, 102761.
61 X. Ma, Y. Li, C. Jiang, S. Chen, H. Liu, Y. Zhang, Q. Zhang and F. Du, *ACS Appl. Mater. Interfaces*, 2025, **17**, 14510–14519.
62 M. Ye, Q. Yin, Q. Ji, J. Deng and H. Jia, *Small*, 2025, 2504209, DOI: 10.1002/smll.202504209.
63 X. Guan, B. Zhang, Y. Xie and C. Jin, *Adv. Electrode Mater.*, 2025, 2500048, DOI: 10.1002/aelm.202500048.
64 M. V. Kharlamova and C. Kramberger, *Nanomaterials*, 2021, **11**, 2863.
65 C. Li, E. T. Thostenson and T.-W. Chou, *Compos. Sci. Technol.*, 2008, **68**, 1227–1249.
66 M. Dolafi Rezaee, B. Dahal, J. Watt, M. Abrar, D. R. Hodges and W. Li, *Nanomaterials*, 2024, **14**, 965.
67 W. Zhou, X. Bai, E. Wang and S. Xie, *Adv. Mater.*, 2009, **21**, 4565–4583.
68 S. Abdullahi, A. F. Ismail, A. Alshahrie, M. M. Damoom, E. Banoqitah and N. Salah, *Radiat. Phys. Chem.*, 2025, **236**, 112907.
69 A. C. R. Bittencourt, A. Ghosh and H. O. Frota, *J. Magn. Magn. Mater.*, 2025, **614**, 172763.
70 H. Xiong, M. A. Motchelaho, M. Moyo, L. L. Jewell and N. J. Coville, *Appl. Catal., A*, 2014, **482**, 377–386.
71 A. Hawkey, X. Rodríguez-Martínez, S. Lindenthal, M. C. F. Jansen, R. Crispin and J. Zaumseil, *Adv. Electrode Mater.*, 2025, 2400817, DOI: 10.1002/aelm.202400817.
72 H. M. Dewey, F. Rahmani, N. Sultana, M. A. Pasquinelli and J. Budhathoki-Uprety, *ACS Omega*, 2025, **10**, 11474–11482.
73 S. Nishitani, K. Ao, A. Jalil, O. I. Arias-Soto, A. Moudi, F. Chen, A. Biyani, P. N. Muppirala and M. P. Landry, *Proc. Natl. Acad. Sci. U. S. A.*, 2025, **122**, e2419666122.
74 A. T. Krasley, S. Chakraborty, L. Vuković and A. G. Beyene, *ACS Nano*, 2025, **19**, 7804–7820.
75 Y. Huang, Y. Zhou, S. Wieland, Y. Li, N. Zhao and J. Zaumseil, *Adv. Funct. Mater.*, 2025, 2423030, DOI: 10.1002/adfm.202423030.
76 T. Biktagirov, U. Gerstmann and W. G. Schmidt, *Nanoscale*, 2025, **17**, 6884–6891.
77 B. Zhang, T. Zhang, Y. Zhang, Y. Lou, W. He and Y. Wang, *AIP Adv.*, 2025, **15**, 045106.
78 X. Qin, F. Peng, F. Yang, X. He, H. Huang, D. Luo, J. Yang, S. Wang, H. Liu, L. Peng and Y. Li, *Nano Lett.*, 2014, **14**, 512–517.
79 B. Aydın, S. Bozoğlu, N. Karatepe and F. S. Güner, *ACS Omega*, 2025, **10**, 102–113.
80 Y. Wang, N. Ju, S. Niu, W. Zhang, X. Liu, Y. Wang, X. Chen, X. Zhang, Y. Ai, H.-b. Sun and G. Xu, *Adv. Funct. Mater.*, 2025, 2422711.
81 J. H. Kim, K. S. Song, Y. Kim, J. Y. Cho, K. Lee, D. G. Lee, J. H. Jin, J. Kim, J. H. Park, W. H. Lee, T. Kim and J. T. Han, *ACS Nano*, 2025, **19**, 4601–4610.
82 J.-C. Li, P.-X. Hou, M. Cheng, C. Liu, H.-M. Cheng and M. Shao, *Carbon*, 2018, **139**, 156–163.
83 G. Dong, M. Huang and L. Guan, *Phys. Chem. Chem. Phys.*, 2012, **14**, 2557–2559.
84 J. Zhang, C. Wu, K. Hou, M. Huang and L. Guan, *Int. J. Hydrogen Energy*, 2018, **43**, 15687–15692.
85 G. Wu and B.-Q. Xu, *J. Power Sources*, 2007, **174**, 148–158.
86 A. Majeed, P. X. Hou, F. Zhang, H. Tabassum, X. Li, G. X. Li, C. Liu and H. M. Cheng, *Adv. Sci.*, 2019, **6**, 1802177.
87 R. Mohan, A. Modak and A. Schechter, *ACS Sustainable Chem. Eng.*, 2019, **7**, 11396–11406.
88 R. Hu, C. Wu, K. Hou, C. Xia, J. Yang, L. Guan and Y. Li, *Carbon*, 2019, **147**, 35–42.

89 T. Fujigaya, J. Morita and N. Nakashima, *ChemCatChem*, 2014, **6**, 3169–3173.
90 J. Zhu, N. Jia, L. Yang, D. Su, J. Park, Y. Choi and K. Gong, *J. Colloid Interface Sci.*, 2014, **419**, 61–67.
91 J. Zhang, S. Lu, Y. Xiang, P. K. Shen, J. Liu and S. P. Jiang, *ChemSusChem*, 2015, **8**, 2956–2966.
92 D. T. D. Weerathunga and T. Fujigaya, *Diamond Relat. Mater.*, 2019, **97**, 107459.
93 W. Bian, Y. Huang, X. Xu, M. A. Ud Din, G. Xie and X. Wang, *ACS Appl. Mater. Interfaces*, 2018, **10**, 9407–9414.
94 Y. Li, N. K. Dang, G. Gao, H. Shin, S. Sharma, X. Wu, O. Kodra, A. Zborowski, P. R. L. Malenfant, J. Ding, C.-T. Dinh and J. Ouyang, *ACS Appl. Nano Mater.*, 2025, **8**, 9077–9089.
95 W. Wen, J. Gao, M. Zhao, Q. Yan, L. Qiang, S. He, P. Zhao, C. Liu, J. Ma, L. Zhang, J. Zhang, H. Xiao and J. Jia, *Int. J. Hydrogen Energy*, 2025, **127**, 903–911.
96 J. Li, H. Li, W. Xie, S. Li, Y. Song, K. Fan, J. Y. Lee and M. Shao, *Small Methods*, 2022, **6**, e2101324.
97 J. Xu, W. Tang, C. Yang, I. Manke, N. Chen, F. Lai, T. Xu, S. An, H. Liu, Z. Zhang, Y. Cao, N. Wang, S. Zhao, D. Niu and R. Chen, *ACS Energy Lett.*, 2021, **6**, 3053–3062.
98 S. Jia, J. Na, X. Liu, J. Li, S. Sun, H. Yu and Z. Shao, *ACS Nano*, 2025, **19**, 22402–22413.
99 S. S. Hardisty, X. Lin, A. R. J. Kucernak and D. Zitoun, *Carbon Energy*, 2023, **6**, e409.
100 A. B. Papandrew, R. A. Elgammal, M. Tian, W. D. Tennyson, C. M. Rouleau, A. A. Puretzky, G. M. Veith, D. B. Geohegan and T. A. Zawodzinski, *J. Power Sources*, 2017, **337**, 145–151.
101 P. Marbaniang, S. Ingavale, P. Karuppanan, A. Swami and B. Kakade, *Int. J. Hydrogen Energy*, 2021, **46**, 10268–10280.
102 J. Han, W. Zhang, K. Liu, H. Zheng, Y. Li, L. Luo, S. Gong, Y. Jia and X. Liang, *Appl. Surf. Sci.*, 2025, **687**, 162238.
103 S. Yu, H. Yamauchi, D. Menga, S. Wang, A. Herzog, H. Xu, D. J. Zheng, X. Wang, H. Iriawan, B. Huang, A. Nitsche and Y. Shao-Horn, *J. Am. Chem. Soc.*, 2025, **147**, 12298–12307.
104 Y. Ding, J. Zhao, W. Zhang, J. Zhang, X. Chen, F. Yang and X. Zhang, *ACS Appl. Energy Mater.*, 2018, **2**, 1026–1032.
105 Y. Lv, Y. Wang, M. Yang, Z. Mu, S. Liu, W. Ding and M. Ding, *J. Mater. Chem. A*, 2021, **9**, 1480–1486.
106 Y. Yang, H.-J. Zhang, Y. Tao, H. Luo and Y. Xue, *ACS Appl. Nano Mater.*, 2025, **8**, 10603–10610.
107 A. Guha and T. N. Narayanan, *J. Phys.: Energy*, 2020, **2**, 034001.
108 K.-C. Lin, C.-P. Hong and S.-M. Chen, *Sens. Actuators, B*, 2013, **177**, 428–436.
109 M. Mehrpooya, F. Valizadeh, R. Askarimoghadam, S. Sadeghi, F. Pourfayaz and S. A. Mousavi, *Eur. Phys. J. Plus*, 2020, **135**, 589.
110 V. R. R. Pendyala, G. Jacobs, U. M. Graham, W. D. Shafer, M. Martinelli, L. Kong and B. H. Davis, *Ind. Eng. Chem. Res.*, 2017, **56**, 6408–6418.
111 Z. Tao, Y. Zhao, Y. Wang and G. Zhang, *C*, 2024, **10**, 69.
112 V. Vosoughi, S. Badoga, A. K. Dalai and N. Abatzoglou, *Ind. Eng. Chem. Res.*, 2016, **55**, 6049–6059.
113 S. A. Chernyak, A. S. Ivanov, S. V. Maksimov, K. I. Maslakov, O. Y. Isaikina, P. A. Chernavskii, R. V. Kazantsev, O. L. Eliseev and S. S. Savilov, *J. Catal.*, 2020, **389**, 270–284.
114 T. O. Eschemann, W. S. Lamme, R. L. Manchester, T. E. Parmentier, A. Cognigni, M. Rønning and K. P. de Jong, *J. Catal.*, 2015, **328**, 130–138.
115 X. Shi, H. Yu, S. Gao, X. Li, H. Fang, R. Li, Y. Li, L. Zhang, X. Liang and Y. Yuan, *Fuel*, 2017, **210**, 241–248.
116 A. Yahyazadeh, V. B. Borugadda, A. K. Dalai and L. Zhang, *Catal. Today*, 2022, **404**, 117–131.
117 Z. Li, R. Liu, Y. Xu and X. Ma, *Appl. Surf. Sci.*, 2015, **347**, 643–650.
118 S. Chernyak, A. Burtsev, S. Maksimov, S. Kupreenko, K. Maslakov and S. Savilov, *Appl. Catal., A*, 2020, **603**, 117741.
119 H. Almkhelfe, X. Li, P. Thapa, K. L. Hohn and P. B. Amama, *J. Catal.*, 2018, **361**, 278–289.
120 A. N. Pour, M. R. Housaindokht and S. M. Kamali Shahri, *Ind. Eng. Chem. Res.*, 2018, **57**, 13639–13649.
121 O. Akbarzadeh, N. A. Mohd Zabidi, N. A. Hamizi, Y. Abdul Wahab, Z. M. Aljunid Merican, W. A. Yehya, S. Akhter, M. Shalauddin, E. Rasouli and M. R. Johan, *Symmetry*, 2019, **11**, 50.
122 A. Karimi, B. Nasernejad, A. M. Rashidi, A. Tavasoli and M. Pourkhalil, *Fuel*, 2014, **117**, 1045–1051.
123 A. Tavasoli, R. M. M. Abbaslou, M. Trepanier and A. K. Dalai, *Appl. Catal., A*, 2008, **345**, 134–142.
124 O. Akbarzadeh, S. F. Alshahateet, N. A. Mohd Zabidi, S. Moosavi, A. Kordijazi, A. A. Babadi, N. A. Hamizi, Y. A. Wahab, Z. Z. Chowdhury and S. Sagadevan, *Catalysts*, 2021, **11**, 846.
125 D. R. Minett, J. P. O'Byrne, S. I. Pascu, P. K. Plucinski, R. E. Owen, M. D. Jones and D. Mattia, *Catal. Sci. Technol.*, 2014, **4**, 3351–3358.
126 O. Akbarzadeh, N. A. Mohd Zabidi, Y. Abdul Wahab, N. A. Hamizi, Z. Z. Chowdhury, Z. Merican Aljunid Merican, M. Ab Rahman, S. Akhter, E. Rasouli and M. R. Johan, *Symmetry*, 2018, **10**, 572.
127 C. Xing, G. Yang, D. Wang, C. Zeng, Y. Jin, R. Yang, Y. Suehiro and N. Tsubaki, *Catal. Today*, 2013, **215**, 24–28.
128 A. Yahyazadeh, V. B. Borugadda, A. K. Dalai and L. Zhang, *Appl. Catal., A*, 2022, **643**, 118759.
129 C. E. Figueira, P. F. Moreira, R. Giudici, R. M. B. Alves and M. Schmal, *Appl. Catal., A*, 2018, **550**, 297–307.
130 C. E. Kozonoe, V. M. Santos and M. Schmal, *Environ. Sci. Pollut. Res.*, 2023, **30**, 111382–111396.
131 N. S. Afandi, M. Mohammadi, S. Ichikawa and A. R. Mohamed, *Environ. Sci. Pollut. Res.*, 2020, **27**, 43011–43027.
132 Z. Tao, D. Shen, Y. Liu, X. Zhang and G. Zhang, *Catalysts*, 2025, **15**, 559.
133 L. M. Chew, W. Xia, H. Düdder, P. Weide, H. Ruland and M. Muhler, *Catal. Today*, 2016, **270**, 85–92.
134 K. Xiong, J. Li, K. Liew and X. Zhan, *Appl. Catal., A*, 2010, **389**, 173–178.

135 T. W. van Deelen, H. Yoshida, R. Oord, J. Zečević, B. M. Weckhuysen and K. P. de Jong, *Appl. Catal., A*, 2020, **593**, 117441.
136 A. Rose, J. Thiessen, A. Jess and D. Curulla-Ferré, *Chem. Eng. Technol.*, 2014, **37**, 683–691.
137 P. Mierczynski, K. Vasilev, A. Mierczynska, W. Maniukiewicz, M. I. Szynkowska and T. P. Maniecki, *Appl. Catal., B*, 2016, **185**, 281–294.
138 G. Lin, X. Liang, Z. Liu, J. Xie, B. Chen and H. Zhang, *Sci. China: Chem.*, 2014, **58**, 47–59.
139 W. Li, R. Nie, Y. Song, L. Ni, D. Wu, G. Wu, R. Chu and X. Meng, *Int. J. Hydrogen Energy*, 2025, **101**, 490–503.
140 D. Janas, S. K. Kreft and K. K. K. Koziol, *J. Ind. Eng. Chem.*, 2015, **25**, 222–228.
141 Z. Jiang, Y. Shi, Y. Bai, X. Song, J. Wang, P. Lv, S. Wu and W. Su, *Fuel*, 2023, **337**, 127136.
142 W. N. Manan, W. N. R. Wan Isahak, Z. Yaakob and S. Samidin, *Bull. Chem. React. Eng. Catal.*, 2025, **20**, 381–391.
143 S. Liu, Z. Yan, Y. Zhang, R. Wang, S.-Z. Luo, F. Jing and W. Chu, *ACS Sustainable Chem. Eng.*, 2018, **6**, 14403–14413.
144 M. Khavarian, S.-P. Chai and A. R. Mohamed, *Fuel*, 2015, **158**, 129–138.
145 W. Donphai, K. Faungnawakij, M. Chareonpanich and J. Limtrakul, *Appl. Catal., A*, 2014, **475**, 16–26.
146 T. Wang, X. Li, F. Liu, B. Liu, X. Peng, Z. Wang, N. Qu, J. Kong, Z. Tang, F. Zeng, H. Lin, X. Lu, T. Ji and J. Zhu, *Chem. Eng. J.*, 2025, **520**, 166244.
147 Y. Zhu, K. Chen, R. Barat and S. Mitra, *ChemEngineering*, 2020, **4**, 16.
148 A. Łamacz, P. Jagódka, M. Stawowy and K. Matus, *Catalysts*, 2020, **10**, 741.
149 P. K. Seelam, M. Huuhtanen, A. Sápi, M. Szabó, K. Kordás, E. Turpeinen, G. Tóth and R. L. Keiski, *Int. J. Hydrogen Energy*, 2010, **35**, 12588–12595.
150 H.-M. Yang and P.-H. Liao, *Appl. Catal., A*, 2007, **317**, 226–233.
151 P.-H. Liao and H.-M. Yang, *Catal. Lett.*, 2007, **121**, 274–282.
152 H. Zhou, S. Liu, F. Jing, S.-Z. Luo, J. Shen, Y. Pang and W. Chu, *Ind. Eng. Chem. Res.*, 2020, **59**, 17259–17268.
153 A. K. Yadav and P. D. Vaidya, *Int. J. Hydrogen Energy*, 2019, **44**, 30014–30023.
154 H. Shahsavar, M. Taghizadeh and A. D. Kiadehi, *Int. J. Hydrogen Energy*, 2021, **46**, 8906–8921.
155 X. Wu, J. Liu, X. Liu, X. An and X. Wu, *Sep. Purif. Technol.*, 2025, **361**, 131493.
156 Q. Li, H. Yang, F. Qiu and X. Zhang, *J. Hazard. Mater.*, 2011, **192**, 915–921.
157 H. Beyer and K. Köhler, *Appl. Catal., B*, 2010, **96**, 110–116.
158 M. Nejadramezan, A. Ajami and S. Sheibani, *Environ. Res.*, 2025, **284**, 122176.
159 H. M. Joseph, H. Narayanan and S. Sugunan, *Diamond Relat. Mater.*, 2025, **152**, 111904.
160 S. Musazad, S. Allahyari, M. Zarei and M. Sillanpää, *Sol. Energy*, 2025, **296**, 113589.
161 M. Li, G. Chen, Y. Chen, Q. Zhu, Y. Yan and L. Liu, *Diamond Relat. Mater.*, 2025, **157**, 112571.
162 A. Al Mayyahi, B. M. Everhart, T. B. Shrestha, T. C. Back and P. B. Amama, *RSC Adv.*, 2021, **11**, 11702–11713.
163 R. Hatel, I. Boukhoubza, I. Derkaoui, M. A. B.-M. Kabatas, E. Matei, M. Enculescu and M. Baitoul, *Colloids Surf., A*, 2025, **711**, 136395.
164 J. Schneider, M. Matsuoka, M. Takeuchi, J. Zhang, Y. Horiuchi, M. Anpo and D. W. Bahnemann, *Chem. Rev.*, 2014, **114**, 9919–9986.
165 K. Lee, H. Yoon, C. Ahn, J. Park and S. Jeon, *Nanoscale*, 2019, **11**, 7025–7040.
166 Y. Zhang, I. Utke, J. Michler, G. Ilari, M. D. Rossell and R. Erni, *Beilstein J. Nanotechnol.*, 2014, **5**, 946–955.
167 K. Woan, G. Pyrgiotakis and W. Sigmund, *Adv. Mater.*, 2009, **21**, 2233–2239.
168 A. L. Linsebigler, G. Lu and J. T. Yates, *Chem. Rev.*, 1995, **95**, 735–758.
169 H. Chen, R. Yang, K. Zhu, W. Zhou and M. Jiang, *J. Hazard. Mater.*, 2002, **94**, 191–201.
170 M. Rahimi, M. Hashemi and A. Nasiri, *J. Environ. Chem. Eng.*, 2025, **13**, 117424.
171 N. Walczak, A. Krzyszczak-Turczyn and B. Czech, *J. Photochem. Photobiol., A*, 2025, **467**, 116437.
172 H. Beyer, K. Chatziapostolou and K. Köhler, *Top. Catal.*, 2009, **52**, 1752–1756.
173 S. Xiao, N. Zhang, Y. Tao, X. Song, G. Li, H. Li and D. Zhang, *ACS Appl. Nano Mater.*, 2022, **5**, 3581–3590.
174 K. Yuan, Y. Zeng, J. Gan, Z. Zhong and W. Xing, *Ind. Eng. Chem. Res.*, 2022, **62**, 247–256.
175 S. Zhang, X. Quan, J. F. Zheng and D. Wang, *Water Res.*, 2017, **122**, 86–95.
176 A. Naderi, S. Sagadevan, R. Rezaei Kalantary, B. Kakavandi, R. Pelalak and H. Yang, *J. Colloid Interface Sci.*, 2026, **703**, 139106.
177 S. Adil, W. S. Kim, T. H. Kim, S. Lee, S. W. Hong and E. J. Kim, *J. Hazard. Mater.*, 2020, **396**, 122757.
178 H. Zuo, C. Wu, H. Du, H. Shi, Y. Fu, T. Zhang and Q. Yan, *Chemosphere*, 2022, **302**, 134927.
179 M. Moradi, M. Haghighi and S. Allahyari, *Process Saf. Environ. Prot.*, 2017, **107**, 414–427.
180 S. Takenaka, T. Arike, H. Matsune and M. Kishida, *Appl. Catal., B*, 2012, **125**, 358–366.
181 Z. Jia, Y. Yang, C. Yang and D. Wang, *Appl. Surf. Sci.*, 2024, **659**, 159866.
182 M. Wei, X. Shi, L. Xiao and H. Zhang, *J. Hazard. Mater.*, 2020, **382**, 120993.
183 L. Shu, X.-X. Lv, Y. Liu, D.-J. Wang, D.-F. Kong and X. Chen, *J. Environ. Chem. Eng.*, 2025, **13**, 117020.
184 L. Cheng, L. Zhu and M. Wei, *Colloids Surf., A*, 2025, **710**, 136261.
185 S. Gao, X. Han, Y. Zhang, L. Zhang, Z. Tian, Y. Xiong, H. Zeng and X. Fan, *Appl. Surf. Sci.*, 2025, **706**, 163549.

186 M. Ganesan, I. P. Chinnuraj, R. Rajendran, T. Rojviroon, O. Rojviroon, P. Thangavelu and S. Sirivithayapakorn, *Diamond Relat. Mater.*, 2025, **155**, 112254.
187 A. Aygun, D. G. Aydogmus, M. Akın, E. Halvaci, M. Bekmezci, I. Kaynak, A. Seyrankaya and F. Sen, *Inorg. Chem. Commun.*, 2025, **175**, 114153.
188 S. Subramanyam, L. Phor, Suman, A. Singh, S. Dahiya, G. S. Selopal, A. Kumar, P. Kumar and S. Chahal, *J. Water Process Eng.*, 2025, **71**, 107149.
189 M. Abdolnabizadeh, S. Allahyari, N. Rahemi, S. Musazad and M. Tasbihi, *J. Photochem. Photobiol., A*, 2026, **471**, 116734.
190 J. Kang, H. Zhang, X. Duan, H. Sun, X. Tan, S. Liu and S. Wang, *Chem. Eng. J.*, 2019, **362**, 251–261.
191 S. Gu, M. Wang, L. Li, H. Yu, Y. Zhao, C. Shen and H. Tao, *Sep. Purif. Technol.*, 2024, **337**, 126318.
192 M. Xie, M. Yao, S. Zhang, L. Kong, L. Zhao, J. Zhan and R.-S. Zhao, *Sep. Purif. Technol.*, 2023, **304**, 122398.
193 Z. Zhao, L. Xiang, Y. Liu, J. Qian, Y. Fu, J. D. Harindintwali, Y. Bian, C. Fang, X. Jiang, F. Wang and R. Naidu, *J. Hazard. Mater.*, 2025, **498**, 139919.
194 J. Peng, L. Li, S. Deng, H. Zhou, Y. Li, C. Fu, L. Lin, Y. Yuan, W. Wei, G. Lv, G. Yang, X. Lu and B. Lai, *J. Hazard. Mater.*, 2025, **485**, 136911.
195 D. Li, Y. Dong, F. Yang, Y. Ding, K. Lv, C. Wang and J. Huang, *Sep. Purif. Technol.*, 2025, **357**, 130037.
196 K. Du, W. Wu, Y. Wang, R. Jia, Y. Liu, X. Yu, W. Wang, G. Yin and J. Guo, *J. Water Process Eng.*, 2025, **73**, 107689.
197 L. Li, S.-z. Hu, T. Huang, N. Zhang and Y. Wang, *Chem. Eng. J.*, 2023, **476**, 146574.
198 I. H. Ifijen and S. I. Omonmhenle, *Biomed. Mater. Devices*, 2023, **2**, 113–120.
199 V. Prabakaran Elanjeitsenni and S. Vadivu Kulandhaivelu, *Bull. Chem. Soc. Ethiop.*, 2024, **38**, 1897–1914.
200 S. P. Bangar, W. S. Whiteside, P. Kajla and M. Tavassoli, *J. Food Meas. Charact.*, 2025, **19**, 2172–2194.
201 S. Sivakumar and T. A. Hema, *Polym. Adv. Technol.*, 2024, **35**, e6518.
202 E. M. Jonathan and O. A. Agbini, *J. Appl. Sci. Environ. Manage.*, 2024, **28**, 2601–2613.
203 F. Z. Yakdoumi, A. S. Hadj-Hamou, N. Rahoui, M. M. Rahman and V. Abetz, *Int. J. Biol. Macromol.*, 2022, **213**, 55–69.
204 M. V. Dias, F. N. Soares, S. V. Borges, M. M. de Sousa, C. A. Nunes, I. R. de Oliveira and E. A. Medeiros, *Food Chem.*, 2013, **141**, 3160–3166.
205 F.-F. Ge, W.-H. Yao, P. Potiyaraj, J.-H. Lin, C.-S. Wu, L. Meng, X. Zhang, C. Preuksarattanawut, Z.-L. Ma and C.-H. Tsou, *J. Polym. Res.*, 2024, **31**, 278.
206 C. H. Tsou, X. Huang, F. F. Ge, J. H. Lin, P. Potiyaraj, C. Preuksarattanawut, T. Yang and X. F. Hu, *Food Chem.: X*, 2025, **31**, 102989.
207 A. M. M. Ibrahim, A. Abou Elfadl, A. M. El Sayed and I. M. Ibrahim, *Polymer*, 2023, **267**, 125650.
208 M. Asaftei, M. Lucidi, C. Cirtoaje, A. M. Holban, C. A. Charitidis, F. Yang, A. Wu, G. A. Stanciu, O. Saglam, V. Lazar, P. Visca and S. G. Stanciu, *RSC Adv.*, 2023, **13**, 19682–19694.
209 F. F. Tong and J. L. Han, *Chalcogenide Lett.*, 2025, **22**, 719–733.
210 H. Zhang, X. Li, X. Zhou, Y. Zhang and Y. Zhao, *Nanoscale*, 2024, **16**, 3113–3120.
211 H. Zhang, M. Zhang, T. Xu, X. Wang, J. Qi, Y. Wang, W. Liu, L. Zhu, Z. Yuan and C. Si, *Chem. Eng. J.*, 2025, **505**, 159476.
212 F. K. Algethami, H. M. Marwani, N. Raza, A. M. Asiri and M. M. Rahman, *Food Chem.*, 2024, **445**, 138792.
213 J. Liu, X. Zhong, X. Gong, L. Deng, G. Tan, Q. E. Zhang, Z. Xiao, Q. Yao, S. Liu, Y. Gao, L. Wang and L. Lu, *Food Chem.*, 2024, **458**, 140275.
214 T. Li, Z. Li, L. Wang, B. Yu, M. Xiao and Z. Zhang, *ACS Nano*, 2024, **18**, 26891–26901.
215 K. Zhang, J. Ji, X. Fang, L. Yan and B. Liu, *Analyst*, 2015, **140**, 134–139.
216 T. B. Rouf, S. Díaz-Amaya, L. Stanciu and J. Kokini, *Food Control*, 2020, **117**, 107350.
217 X. Cao, D. Liu, R. Shi, T. Li, X. Fang, X. Feng, P. Li, Y. Zhang, M. Xiao and L. Wang, *Chem. Eng. J.*, 2025, **509**, 161218.
218 İ. Unal, *Nanomaterials*, 2025, **15**, 179.
219 B.-C. Cha, S. Jun, B. Jeong, M. Ezazi, G. Kwon, D. Kim and D. H. Lee, *J. Power Sources*, 2018, **401**, 296–302.
220 R. Rao, C. L. Pint, A. E. Islam, R. S. Weatherup, S. Hofmann, E. R. Meshot, F. Wu, C. Zhou, N. Dee, P. B. Amama, J. Carpena-Nuñez, W. Shi, D. L. Plata, E. S. Penev, B. I. Yakobson, P. B. Balbuena, C. Bichara, D. N. Futaba, S. Noda, H. Shin, K. S. Kim, B. Simard, F. Mirri, M. Pasquali, F. Fornasiero, E. I. Kauppinen, M. Arnold, B. A. Cola, P. Nikolaev, S. Arepalli, H.-M. Cheng, D. N. Zakharov, E. A. Stach, J. Zhang, F. Wei, M. Terrones, D. B. Geohegan, B. Maruyama, S. Maruyama, Y. Li, W. W. Adams and A. J. Hart, *ACS Nano*, 2018, **12**, 11756–11784.